The Wilson-Dirac Operator Eigenspectrum for the Theories of QCD and Super Yang-Mills with One Flavour

Jaïr Wuilloud

2010

Institut für theoretische Physik

The Wilson-Dirac Operator Eigenspectrum for the Theories of QCD and Super Yang-Mills with One Flavour

Inaugural-Dissertation
zur Erlangung des Doktorgrades
der Naturwissenschaften im Fachbereich Physik
der Mathematisch-Naturwissenschaftlichen Fakultät
der Westfälischen Wilhelms-Universität

vorgelegt von
Jaïr Wuilloud

2010

Dekan: Prof. Dr. Johannes Wessels
Erster Gutachter: Prof. Dr. Gernot Münster
Zweiter Gutachter: Prof. Dr. Uwe Philipsen
Tag der mündlichen Prüfungen: .....31.3.2010.....
Tag der Promotion: .....

Zusammenfassung

Für Simulationen der QCD und der minimalen, supersymmetrischen super Yang-Mills Feldtheorien mit einem Flavour (von Quark bez. Gluino) werden fermionische Felder und Eichfelder durch den Wilson-Formalismus auf einem diskretisierten, periodischen Version der Raum-Zeit versetzt.

In diesem Zusammenhang spielen die niedrigsten Eigenmoden des Dirac Operators eine grundsätzliche Rolle, als die fermionischen Felder und Eichfelder mit statistischen Methoden und numerischen Mitteln dynamisch erzeugt werden. Darüber hinaus lassen sich fundamentale Grössen einer Theorie von den niedrigsten Eigenmoden bestimmen: Das Vorzeichen Problem wird durch die kleinsten Eigenwerte des Dirac Operators bestimmt. Bedeutende Erwartungswerte lassen sich durch spektrale Zerlegung aus den kleinsten Eigenmoden partiell rekonstruieren. Dazu veranschaulichen die niedrigsten Eigenmoden des Dirac Operators physikalische Eigenschaften der realisierten Theorien.

In dieser Arbeit werden diese Aspekte in beider Theorien untersucht. Im Besonderen werden das Vorzeichen Problem, die Fragen einer Verletzung der CP-Symmetrie sowie die Definition der Quarkmasse in Abwesenheit der chiralen Symmetrie in einer QCD ähnlichen Theorie unter die Lupe genommen. Durch diese Fragestellung entsteht mit Hilfe der Dirac Operator Eigenwertverteilungen und spektrale Zerlegungen eine neue Aspekte betrachtende Diskussion, welche Artefakte, Beschränkungen und Eigenschaften des Wilson-Formalismus zu identifizieren versucht. Es zeigt sich, dass ein Studium der CP-Verletzung im Wilson-Formalismus nur in einem beschränkten Bereich stattfinden kann. Während die Verteilung der Eigenwerte des Wilson-Dirac Operators besser verstanden wird bieten sich unerwartete und unpräzise Definitionen der Quarkmasse aus Beobachtungen der niedrigsten Eigenmoden und derer Chiralität an.

Dennoch setzen solche Analysen effiziente Werkzeuge zur Berechnung der Eigenwerte voraus. Zu diesem Zweck wurden im Laufe dieser Arbeit besondere Strategien entwickelt, welche zu deutlichen Verbesserungen führten. Sie werden hier diskutiert und getestet.

Contents

Chapter 1

Introduction

The path integral formulation of Quantum field theory offers an elegant and intuitive approach. Nonetheless, analytical computations of path integrals are very difficult to achieve while the perturbation theory is only valid within a finite range of parameters.

As an alternative, the path integral in Euclidean space-time provides with a formulation, which by analogy with statistic quantum mechanics can be used to perform numerical simulations. In order to achieve this, the quantum field theoretical models are put on a discretised Euclidean version of space-time with periodic boundaries (the so-called *lattice*).

Such a lattice formulation imposes a natural energy cut-off, as well as offers the possibility to realise computations from first principles. Quantities believed to have a fundamental role in Nature are considered (quark, gluon fields, ...). In this framework on the lattice, the DESY-Münster collaboration is investigating the following theories:

- **One flavour ($N_f = 1$) QCD** is a version of QCD without symmetry. The absence of chiral symmetry allows for an investigation of original questions, as described in this work.

  In QCD, chiral symmetry is expected to play a fundamental role and connects the bare parameters of the theory to the low energy physics. Situations where the bare quark masses are positive or zero are distinguishable, in the sense that a non-vanishing quark mass explicit breaks chiral symmetry. In one flavour QCD, this does not hold anymore and the situation becomes ambiguous as the unique bare quark parameter can be widely tuned along the renormalisation group flow.

  Although the strong interaction appears in nature to be CP-invariant, a CP-symmetry breaking phase is thought to exist for a particular setting of the bare quark masses, with the lowest one set to be negative. One flavour QCD offers the opportunity to pull the only quark mass into the negative regime and test a CP-symmetry breaking scenario.

  The one flavour QCD study is completed by a partially quenched analysis. This replaces the one flavour theory within the well-known framework of multiflavour QCD, where comparisons and consistency checks can be performed.

- **Minimal supersymmetric ($\mathcal{N} = 1$) super Yang-Mills (Sym)** is a supersymmetric model restricted to the gauge fields content (the interaction between the gluinos and gluons). The low lying bound states or *supermultiplets* of $\mathcal{N} = 1$ ($SU(2)$) are under study while it is attempted to detect a supersymmetric phase.

  Several difficulties appear, as a supersymmetric model is defined on the lattice (absence of infinitesimal translations, SUSY breaking through doublers, breaking of the Leibniz rule). The approach chosen here (Curci-Veneziano formulation) rephrases the one flavour theory of QCD in its Wilson formulation and is expected to solve those problems in the continuum.

  From the supermultiplets mass spectrum, predictions from low-energy effective theories are tested (Yankielowicz, Veneziano, Farrar, Gabadadze, Schwetz, ...).

- Both one flavour models become planar equivalent in an expansion at large-N_c and analytical predictions concerning planar equivalence can be tested from lattice simulations.

Any attempt to formulate consistently fundamental quantum field theories on a discretised space-time is theoretically difficult while practical lattice computations face discretisation artefacts and statistical limitations.

Among different possible lattice formulations, the Wilson discretisation was chosen. This scheme explicitly breaks chiral symmetry, which is expected to be restored as the continuum limit is approached with appropriated parameter tunings. Although the production of configurations is relatively cheap, in comparison to other formulations (since they are controversial, staggered fermions were avoided while the twisted mass formulation is not possible for one flavour models), several drawbacks show up as the quark or gluino masses become small or negative. Small mass parameters imply small eigenvalues of the Wilson-Dirac operator, which mean tiny statistical weights. As a result, practical difficulties appear in the dynamic generation of the configurations through Two-Step Polynomial Hybrid Monte-Carlo algorithm (TS-PHMC), while the fermionic measure exhibits sign fluctuations.

A non-positive fermionic measure can wash away the statistical information (this is the sign problem). On the other hand, a non-positivity is a necessary condition for the breaking of CP-symmetry in QCD.

For practical simulations and statistical quantities, the presence of a fluctuating measure can be dealt with simple reweighting of the configuration contributions. For doing this, the sign fluctuations have to be carefully evaluated.

For both one flavour theories, the fermionic measure is given by $\det(D_W)$, or alternatively by $\det(Q)$, whereas $Q = \gamma_5 D_W$ is the hermitian version of the Wilson-Dirac operator D_W. As both operators D_W and Q can be diagonalised through similarity transformations into their eigenvalue systems, the determinant sign can be computed from the Wilson-Dirac operator eigenvalues. However, as the eigensystem of the Wilson-Dirac operator is partially accessible in practice, only the following two approaches are considered:

- The eigenflow strategy with the hermitian Wilson-Dirac operator $Q = \gamma_5 D_W$.
- A direct computation of the negative real eigenvalues of the non-hermitian operator D_W.

The second approach allows for an exact computation of the determinant sign and was chosen in this work. Nevertheless, D_W is non-normal and shows a very dense eigenspectrum. This makes evaluations of the lowest eigenvalues difficult (computations were performed with the Arnoldi algorithm (in its ARPACK version)). For that reason, it was necessary to improve the algorithm extraction performances.

In addition to internal operations organised inside of the algorithm itself, the eigenspectrum can be *preconditioned* through polynomial transformations. Such transformations are discussed, improved and tested in this work, where they are specialised to the problem of computing the lowest real eigenvalues of D_W. Those methods extend the algorithm performance as well as the computational possibilities (more real eigenvalues can be computed).

As a result, an efficient extraction of the non-hermitian Wilson-Dirac operator D_W low eigenspectrum makes possible the following studies:

- As the main point, the determinant sign can be computed from the lowest real eigenvalues of D_W for larger lattice volumes and smaller bare gluino or quark masses. Thanks to that, particle spectrum or phase space studies in the Wilson formalism are "backed up" and are therefore feasible within a broader range of parameters.

  For the performed simulations, effects from the determinant sign fluctuations on the particle spectrum as well as on the vacuum expectation values are reviewed.

- A better understanding of the lowest real eigenvalues of D_W fluctuations can be collected, also in relation with other quantities. In proceeding so, an alternative, indirect approximation of the determinant sign becomes available. Since no analytical relation is known between the lattice Wilson-Dirac operators D_W and the lowest eigenvalues of Q, a better understanding may emerge as comparisons are done with important statistical samples.

- The eigenspectrum and its corresponding eigenvectors are connected to vacuum expectation values through the spectral decomposition. Because D_W is a non-normal operator, it is in principle not appropriate for the implementation of precise spectral decompositions.

  However, the spectral decomposition coupled with basic tests give a pictorial understanding of how the eigenspectrum domains contribute to the vacuum expectation values. This offers an alternative approach for understanding the underlying physics, discussing lattice artefacts and eventually anticipating other parameter regimes (where the eigenspectrum is extended or shifted).

Chapter 2

Theory

This part introduces the theories studied by the DESY-MUENSTER collaboration (see among others [59], [62], [61], [62], [63], [64]).

After a short introduction to the theories of one flavour Quantum chromodynamics ($N_f = 1$ QCD) and minimal (one supersymmetric partner) super Yang-Mills ($\mathcal{N} = 1$ Sym), theoretical issues under investigation by the current projects are reviewed. This introduction is rather a theoretical overview trying to focus on the interesting physical questions and relevant theoretical objects.

Both theories are introduced simultaneously, which makes the theory part compact but not pedagogical. It should be stressed that one flavour QCD and $\mathcal{N} = 1$ Sym have fundamental differences.

2.1 Introduction to the theories

2.1.1 One flavour QCD

Quantum chromodynamics is the theory of strong interactions. The flavour symmetry $SU(3)_f$ is believed to play an essential role, since it is is approximately realised by the hadron particle spectrum observed at low energy. In addition to this, it was realised that the quarks also have an additional degree of freedom called colour that can assume three different values. Therefore, the Lagrangian of strong interactions is invariant under an additional $SU(N_c)$-symmetry.

Consider standard QCD with $N_f = 6$ (3 additional flavour were discovered) and $N_c = 3$, one constructs a theory of QCD based on the gauge principle. The QCD Lagrangian reads (in compact notations and in Minkowski space-time)

$$\mathcal{L} = -\frac{1}{4}\mathrm{Tr}_C(G_{\mu\nu}G^{\mu\nu}) + \sum_f^6 \bar{\Psi}_f \left(i\gamma^\mu \mathcal{D}_\mu - m_f\right)\Psi_f. \tag{2.1}$$

In explicit notations, $\Psi_{f,\alpha,a}(x)$ is the fermionic Dirac spinor field, of spin 1/2, describing the quarks and $f \in \{u(p), d(own), s(trange), c(harm), b(ottom), t(op)\}$ indexes the flavour, $\alpha \in \{1, ..., 4\}$ the spinor and $a \in \{r(ed), g(reen), b(lue)\}$ the colour. x describes the position in space-time. Tr_C is the trace taken over

the colour indices. $A_{\mu,\,a}(x) \in SU(N_c)$ is the bosonic field describing the gluons, of spin 1, transmitting the strong interactions. More explicitly, in term of its generator $A_\mu = A^a_\mu \tau_a$, $\tau_a \in su(N_c)$. $\mathcal{D}_\mu = \partial_\mu - igA_\mu$ is the covariant derivative and $G_{\mu\nu,\,a} = G^a_{\mu\nu}\tau_a$, with $G_{\mu\nu,\,a} = \partial_\mu A_{\nu,\,a} - \partial_\nu A_{\mu,\,a} + g f_{abc} A_{\mu,\,b} A_{\nu,\,c}$. Under the action of $SU(N_c = 3)$, Ψ_f and A_μ transform respectively in the fundamental and adjoint representation of $SU(N_c)$.

For low energy QCD or close to the chiral limit ($m_u = m_d = m_s = 0$), only the up, down and strange flavours are considered and $N_f = 3$. Reducing the number of flavours further, one flavour QCD corresponds to the Yang-Mills theory

$$\mathcal{L}_{Y.-M.} = -\frac{1}{4}\mathrm{Tr}_C(G_{\mu\nu}G^{\mu\nu}) + \bar{\Psi}\left(i\gamma^\mu \mathcal{D}_\mu - m_f\right)\Psi, \tag{2.2}$$

where Ψ is the unique quark field.

As will be emphasised later, the one flavour QCD model lacks important features of standard QCD, such as chiral symmetry.

2.1.2 $\mathcal{N} = 1$ Sym

Supersymmetry has been proposed as a possible extension of the standard model. However, since no trace of it was found in the explored phenomenology, it is assumed to be spontaneously broken close to the electroweak scale. In general, supersymmetry also offers the possibility of a more fundamental quantum field theory. Therefore, there is a strong interest in understanding non-perturbative mechanisms in supersymmetric gauge theories.

The simplest supersymmetric gauge theory, the minimal ($\mathcal{N} = 1$ fermionic-bosonic super-partner) supersymmetric extension of Yang-Mills theory, has the following Lagrangian (for details about its derivation from the Wess-Zumino gauge, see [45])

$$\mathcal{L} = -\frac{1}{4}\mathrm{Tr}_C(G_{\mu\nu}G_{\mu\nu}) + \frac{i}{2}\mathrm{Tr}_C(\bar{\lambda}\gamma^\mu \mathcal{D}_\mu \lambda) - m_{\tilde{g}}\mathrm{Tr}_C(\bar{\lambda}\lambda), \tag{2.3}$$

where the $\lambda_{\alpha,\,a}(x)$ are the Majorana Grassmannian fermion fields called *gaugino* or *gluino*, put in explicit notations (α, a are respectively the spinor and colour adjoint representation indices). The fields λ satisfies the Majorana conditions: $\bar{\lambda} = \lambda^T C$, where C is the charge conjugation matrix. The fermions fields λ are here in their adjoint representation and one has $\lambda_\mu = \lambda^a_\mu \mathrm{T}_a$, $\mathrm{T}_a \in Ad_{su(N_c)}$. $\mathcal{D}_\mu = \partial_\mu + iA_\mu$ is the covariant derivative. A_μ represents the gluon fields and $G_{\mu\nu}$ are defined as in QCD.

Supersymmetry occurs under the condition for the gaugino mass $m_{\tilde{g}} = 0$, which can been shown as the above Lagrangian is left invariant under infinitesimal transformation with a Grassmannian parameter ϵ:

$$\delta A^a_\mu = 2i\bar{\epsilon}\gamma_\mu \lambda^a, \quad \delta\lambda^a = -\sigma_{\mu\nu}F^a_{\mu\nu}\epsilon.$$

2.2 Symmetries of the massless theory

2.2.1 One flavour QCD

The massless ($m_q = 0$) Lagrangian in eq.(2.1) admits the following $U_A(1)$ axial symmetry

$$\Psi \to e^{i\alpha\gamma_5}\Psi, \quad \bar{\Psi} \to \bar{\Psi}e^{i\alpha\gamma_5}.$$

This symmetry is broken explicitly by a mass term, which is rotated into the complex plane by the $U_A(1)$ symmetry:

$$\Psi \to e^{i\alpha\gamma_5}\Psi, \quad m\bar{\Psi}\Psi \to m_1\bar{\Psi}\Psi + m_5\bar{\Psi}\gamma_5\Psi, \tag{2.4}$$

with $m_1 = \cos(2\alpha),\ m_5 = m\sin(2\alpha)$.

Nevertheless, the axial symmetry is anomalous, i.e. broken at the quantum level. This can be seen through the triangular anomaly, which for the one flavour QCD anomalous current $A^\mu(x) = \bar{\Psi}(x)\gamma^\mu\gamma_5\Psi(x)$ reads, in term of the topological density $q(x)_{Y.-M.}$,

$$\partial_\mu A^\mu(x) = N_f q(x)_{Y.-M.} \neq 0, \qquad q(x)_{Y.-M.} \equiv \frac{g^2}{32\pi^2}\epsilon_{\mu\nu\rho\sigma}\mathrm{Tr}_C(F^{\mu\nu}F^{\rho\sigma}). \tag{2.5}$$

Recall that the Lagrangian in eq.(2.1) admits a CP-violating $\Theta_{Y.-M.}$-term

$$\mathcal{L}_{\Theta_{Y.-M.}} = \Theta_{Y.-M.}\, q(x)_{Y.-M.}.$$

In the path integral formalism, the measure is non-invariant under $U_A(1)$ transformations and under axial transformation, a term proportional to $q(x)_{Y.-M.}$ arises in the Lagrangian density from the path integral measure [50] .

Summarising, the action of $U_A(1) : \Psi \to e^{i\frac{\alpha}{2}\gamma_5}\Psi$ affects the theory parameters in the following manner

$$m \to m\, e^{i\alpha\gamma_5}, \quad \Theta_{Y.-M.} \to \Theta_{Y.-M.} - \alpha \tag{2.6}$$

One flavour QCD versus $N_f > 1$ QCD

In contrast to standard QCD, the one flavour version of QCD has no chiral symmetry, which can directly be seen considering the chiral symmetry for an arbitrary number of flavours N_f

$$SU(N_f)_L \otimes SU(N_f)_R \otimes U(1)_A \otimes U(1)_V \ \ (N_f > 1), \tag{2.7}$$

$$U(1)_A \otimes U(1)_V \ \ (N_f = 1). \tag{2.8}$$

Since the axial symmetry vanishes anomalously, the one flavour theory is left with the ordinary vector symmetry. This difference between the one flavour QCD and standard QCD has deep consequences that are going to be discussed in subsection 2.4.1.

2.2.2 $\mathcal{N} = 1$ Sym

The massless ($m_{\tilde{g}} = 0$) $\mathcal{N} = 1$ Sym Lagrangian eq.(2.3) admits the following $U(1)_R$ symmetry:

$$\lambda \to e^{-i\alpha\gamma_5}\lambda, \quad \bar{\lambda} \to \bar{\lambda}e^{-i\alpha\gamma_5}$$

As for one flavour QCD, this symmetry is anomalously broken and also affects the path integral measure.

For $\mathcal{N} = 1$ Sym, the anomalous $\Theta_{SY.-M.}$-term reads

$$\mathcal{L}_{\Theta_{SY.-M.}} = 2N_c\Theta_{SY.-M.}\, q(x)_{SY.-M.},$$

with $q(x)_{SY.-M.} = \frac{1}{32\pi^2}\epsilon^{\mu\nu\rho\sigma}F^a_{\mu\nu}F_{\rho\sigma}$.

As for one flavour QCD, the action of $U(1)_R : \lambda \to e^{i\alpha\gamma_5}\lambda$ in eq.(2.3) is summarised as

$$m_{\tilde{g}} \to m_{\tilde{g}}\, e^{-2i\alpha\gamma_5},\ \Theta_{SY.-M.} \to \Theta_{SY.-M.} - 2N_c\alpha \tag{2.9}$$

In the $\mathcal{N} = 1$ Sym case, the final picture is slightly different. An anomaly is indicated by a non-vanishing divergence of the axial current. However, as shown in eq.(2.9), this quantity is rotated by $U(1)_R$. Thus, in the supersymmetric case ($m_{\tilde{g}} = 0$), the anomalous symmetry leaves an Z_{2N_c} subgroup of $U(1)_R$ unbroken ($\alpha \equiv \frac{k\pi}{N_c}$, $k = 0,\, 1,\, ,\cdots ,\, 2N_c - 1$).

2.3 Particle states of the theories with one flavour

For the one flavour QCD and the $\mathcal{N} = 1$ Sym models, the particle spectrum is under investigation. Since confinement is assumed for both theories, the observed particle spectra appear as colourless states formed out of the fundamental elements of the theories (quarks for one-flavour QCD, gluinos and gluons for $\mathcal{N} = 1$ Sym). However, with one flavour, the number of available colourless states is strongly reduced.

As physical quantities have to be extracted, low-energy approximations of one flavour QCD or $\mathcal{N} = 1$ Sym are realised by effective theories (chiral perturbation theory (χPT) for ordinary QCD (for an introduction [14]), Veneziano-Yankielovicz effective theory for $\mathcal{N} = 1$ Sym [16]).

2.3.1 Mesonic sector

For $\Phi(x)$, the field Ψ in the one flavour QCD or λ in the $\mathcal{N} = 1$ Sym theory. The unique mesonic states available are given by the following pseudoscalar (P) and scalar (S) interpolating operators

$$0^- : \quad P(x) = \bar{\Phi}(x)\gamma_5\Phi(x), \tag{2.10}$$

$$0^+ : \quad S(x) = \bar{\Phi}(x)\Phi(x). \tag{2.11}$$

0^+ and 0^- summarise the spin and parity of those states. Depending on their quantum numbers, these states are labelled in analogy with their counterparts in ordinary $N_f = 3$ QCD.

One flavour QCD For reasons to become clear later, the unique quark state is labelled Ψ_s. One has $\eta' = \eta_s \equiv \bar{\Psi}_s \gamma_5 \Psi_s$ for the pseudoscalar and $\sigma_s = \bar{\Psi}_s \Psi_s$ for the scalar state.

$\mathcal{N} = 1$ **Sym** Equivalently, for fermionic states transforming in the adjoint representation, the effective action of Veneziano and Yankielovicz [16] describes the gluino-balls $a - \eta' \equiv \bar{\lambda}\gamma_5\lambda$ for the pseudoscalar state and $a - f_0 = \bar{\lambda}\lambda$ for the scalar one. The label $a-$ specify that the fields transform in the adjoint representation.

2.3.2 Additional states considered

One flavour QCD For one flavour QCD, one can introduce baryonic fields with $\Delta_i(x) \equiv \epsilon_{abc}[\psi^T_{s,\,a} C \gamma_i \psi_{s,\,b}(x)]\psi_{s,\,c}$. It is analogous to the Δ^{++} of QCD, with spin/parity $\frac{3}{2}^+$.

$\mathcal{N} = 1$ **Sym** One considers the spin $\frac{1}{2}$ gluino-glueball $\tilde{\chi}$ [16] [45].

2.4 Probing the vacuum structure

Call Φ one of the fields $\{\Psi_s,\, \lambda\}$ introduced above. The scalar and pseudoscalar condensates are then defined here as

$$\text{scalar}: \ \langle \bar{\Phi}\Phi \rangle \tag{2.12}$$

$$\text{pseudo} - \text{scalar}: \ \langle \bar{\Phi}\gamma_5\Phi \rangle, \tag{2.13}$$

where $\langle \, ... \, \rangle$ is the vacuum expectation value, expressed by statistical averages in path integral formalism.

For theoretical reasons to be explained below and because they can be directly measured on the lattice, those quantities can give useful information about the vacuum structures of the $N_f = 1$ QCD and $\mathcal{N} = 1$ Sym theories.

2.4.1 Hypothetical CP breaking in one flavour QCD

In general, strong interactions are believed to be CP-invariant. However, as one of the bare quark masses turns out to become negative, Dashen [1] and Creutz [4] [3] have shown that a CP-breaking phase is realised in an effective theory of QCD.

As an introduction, an imprecise but suggestive effective model proposed in [3] gives the picture. Recall first that the mass term rotates under the anomalous symmetry $U_A(1) : \Psi_s \to e^{i\alpha\gamma_5}\Psi_s, \ \ m\bar{\Psi}_s\Psi_s \to m_1\bar{\Psi}_s\Psi_s + m_5\bar{\Psi}_s\gamma_5\Psi_s$.

From the one flavour QCD Lagrangian in eq.(2.1), one constructs an effective theory with the unique light pseudoscalar meson state η_s. Analogously to standard QCD, one expects from conventional chiral symmetry arguments $m^2_{\eta_s} \sim m_q$. In $N_f = 3$ QCD, the η_s mass gets a mass from the axial anomaly, which suggests to set

$$m^2_{\eta_s} \sim m_q + c$$

instead, with c an additive constant. As a next step, a typical, self-interacting potential $V(\eta_s) = \frac{m_q+c}{2}\eta_s^2 + \lambda\eta_s^4$ is considered. Mimicking standard QCD, it may be completed with a linear part as

$$V(\eta_s) = \frac{m_q + c}{2}\eta_s^2 + \lambda\eta_s^4 + m_5\eta_s.$$

Let the η_s mass become negative for $m_1 < -c$, the potential shape signals a spontaneous symmetry breaking, with the η_s field acquiring an expectation value

$$\langle\eta_s\rangle \sim \langle\bar{\Psi}_s\gamma_5\Psi_s\rangle \sim \sqrt{\frac{|m_1| - c}{4\lambda}} \neq 0.$$

As $\langle\bar{\Psi}_s\gamma_5\Psi_s\rangle$ is a CP-odd field, the CP-symmetry is broken.

For a higher number of flavours, a similar discussion becomes rigorous. There, in the formalism of an effective theory with underlying chiral symmetry, it can be shown that the vacuum becomes unstable as one bare quark mass parameter gets negative. The CP-symmetry is expected to be broken as the degenerated vacua are CP-odd [4] [5]. The situation is summarised in Fig.(2.1).

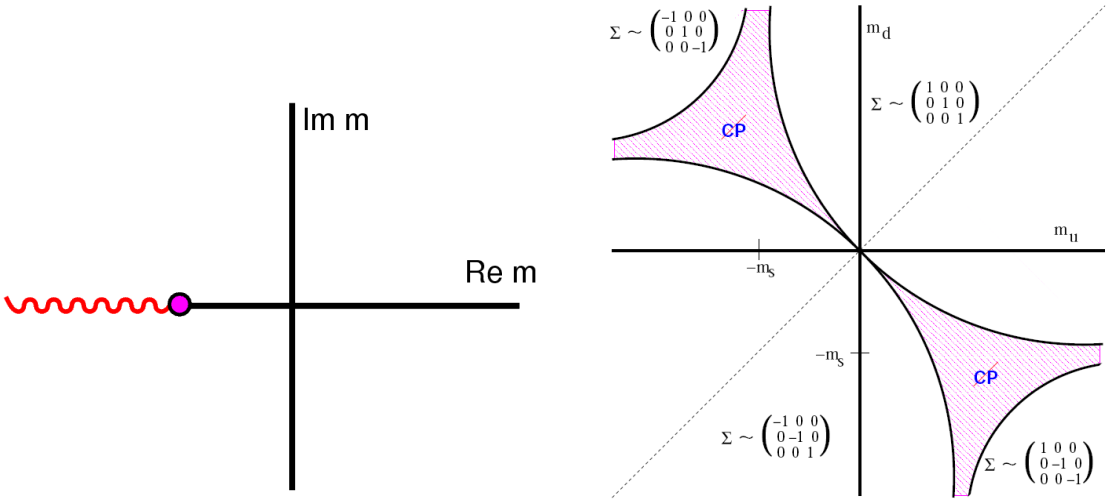

Figure 2.1: In the complex plane, the hypothetical phase diagram for one flavour QCD. The wavy line in the negative mass region would correspond to a first order phase transition ending at a second critical point [3]. The CP-symmetry would be spontaneously broken for a negative quark mass. The physical region is along the real line as a complex mass can be rotated away by the anomalous symmetry $U_A(1)$. On the right, for $N_f = 3$, the situation can be more consistently studied analytically and the following phase diagram is found (m_u, m_d are tuned while m_s is fixed)[4] .

2.4.2 Spontaneous breaking of chiral symmetry in $\mathcal{N} = 1$ Sym

Theoretical arguments indicate that the vacuum of Sym develops a non-vanishing gluino condensate, implying spontaneous breaking of the discrete chiral symmetry Z_{2N_c} into $Z_2 : \lambda \to -\lambda$. The vacuum structure is sketched in Fig.(2.2), where the $k = 0, \ldots, N_c - 1$ label the N_c degenerate vacua related by transformations within the quotient group Z_{2N_c}/Z_2. The gluino condensate could be analytically evaluated by different methods [44] and is predicted to be

$$\langle \bar{\lambda}\lambda \rangle = c\Lambda^3 e^{\frac{i2\pi k}{N_c}}, \tag{2.14}$$

where Λ is the dynamical scale of the theory introduced by dimensional transmutation.

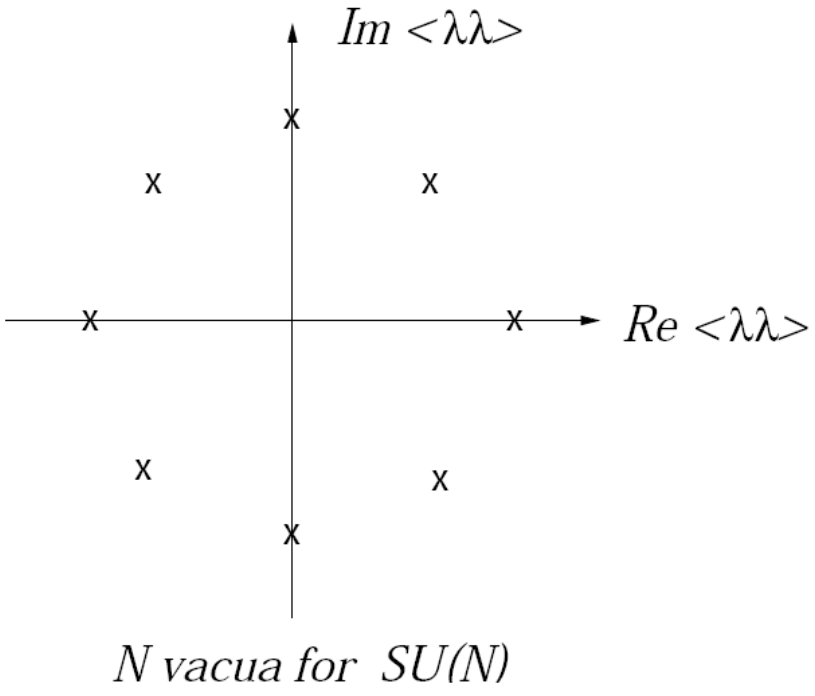

Figure 2.2: The gluino condensate $\langle \lambda\lambda \rangle$ serves as order parameter labelling distinct vacua in supersymmetric gluodynamics. For the $SU(N_c)$ group, there are N_c discrete vacua.

2.5 Planar equivalence and relations between one flavour QCD and $\mathcal{N} = 1$ Sym

Planar equivalence provides with an aesthetic and intriguing theoretical frame, which approximately connects $\mathcal{N} = 1$ Sym and one flavour QCD. The general

picture is described below and sketched in Fig.(2.3).

In the framework of the t'Hooft large-N_c expansion, the planar Feynman graphs start to strongly dominate the Feynman graphs entering the perturbation theory (see for example [13]). In such an expansion, it is possible to see that several theories have identical planar graphs, although fundamental quantities may be different.

If, in addition to this, the expanded theories have similar vacuum structures, one speaks of *common sector* for the set of quantities becoming similar at large N_c (in terms of planar graphs). At large N_c, perturbative results can be imported/exported within the common sector.

The orientifold-A (Antisymmetric) theory is a construction corresponding to one flavour QCD at $N_c = 3$. In addition to this, it is at large N_c planar equivalent to $\mathcal{N} = 1$ Sym [8]. For this reason, a partial confirmation of planar equivalence may be found in the one flavour theory, where a prediction from the planar equivalence theory can be tested for $m_{\eta'}/m_\sigma$ [10].

Planar equivalence also gives arguments for the existence of confinement in $\mathcal{N} = 1$ Sym.

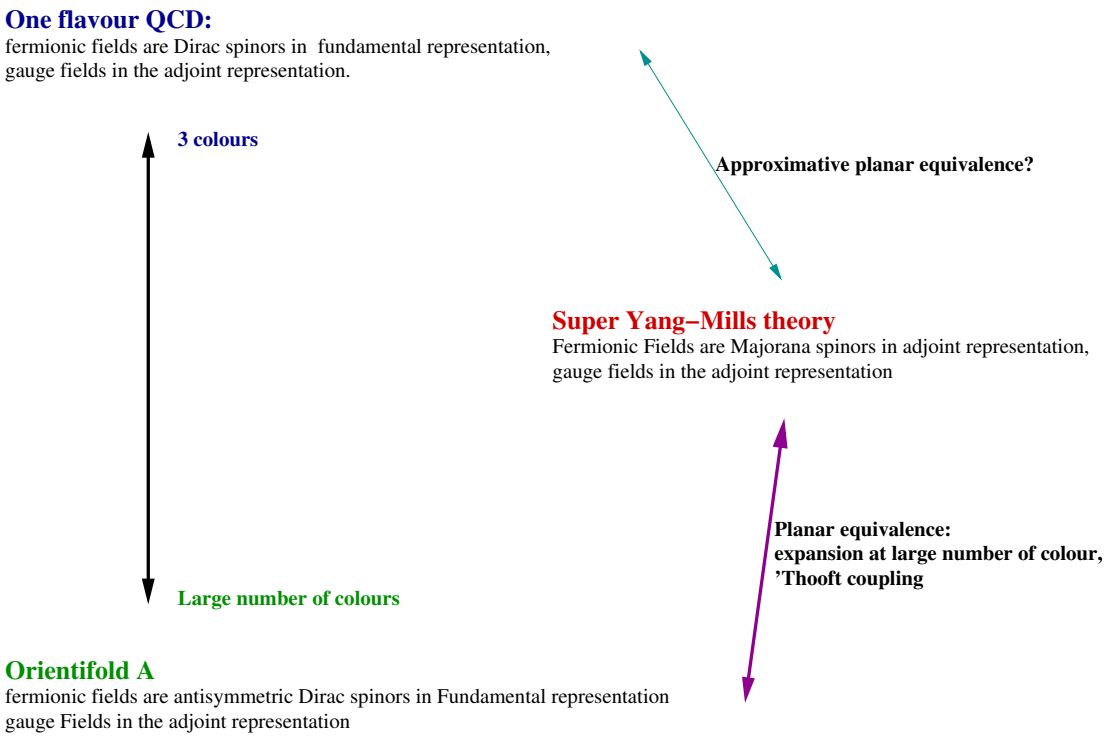

Figure 2.3: Picture summarising the approximative relation between one flavour QCD and $\mathcal{N} = 1$ Sym through planar equivalence. The orientifold A theory simply turns out to be one flavour QCD if $N_c = 3$.

2.6 Theoretical issues around one flavour QCD

2.6.1 The strong CP problem

Although the CP-symmetry is broken in nature and in the weak interactions, the strong sector of the standard model seems to be CP-invariant. In eq.(2.6), it was noticed that, in the Lagrangian, the CP-symmetry breaking terms rotate under the axial symmetry $U_A(1)$. Nonetheless, $\Theta_{Y.-M.}$ is forced to be zero by experimental results.

This arbitrariness of Nature in the fixing of $\Theta_{Y.-M.} = 0$ and the lack of theoretical explanation for it is known as the strong CP-problem. A vanishing up quark mass $m_u \to 0$ is discussed as a possible way out [6] [7].

2.6.2 Determinant sign in one-flavour QCD

An other important issue is the possibility, with a negative quark mass, of negative determinants in the one flavour QCD theory. In that case, the path integral expectation values have to be reweighted, which requires computations of the determinant signs (see Chapters 4, 6).

A non-positive fermionic measure is a prerequisite for a spontaneous CP-breaking in QCD, as shown by Vafa and Witten [2].

2.6.3 Absence of chiral symmetry and consequences

The effective version of standard QCD is constructed assuming a spontaneous breaking of the chiral symmetry. The goldstone bosons resulting of the process are identified with low energy mesonic states, after explicit chiral symmetry breaking (see for example [14]).

The effective theory constructed through chiral perturbation theory gives, among other results, the GMOR (Gell-Mann/Oakes/Renner) relations between the mesonic states and the lowest bare quark masses (up and down quarks in the approximation $m_q \equiv m_u = m_d$)

$$M_\pi \propto m_q^2. \tag{2.15}$$

In addition to fix a lower bound $m_q > 0$ for the quark masses, the relation in eq.(2.15) distinguishes unambiguously between the two following cases:

- $m_q > 0 \iff M_\pi > 0$: chiral symmetry is explicitly broken.
- $m_q = 0 \iff M_\pi = 0$: chiral symmetry remains.

2.6.4 The problem of a quark mass definition in one flavour QCD

In one flavour QCD, a definition of the physical quark mass faces the following issues:

- In the absence of chiral symmetry, no GMOR relations fix a lower boundary for the quark mass parameters.
- No explicit breaking of chiral symmetry distinguishes between phases with vanishing or non-vanishing quark masses.

Recall that the quark mass entering the QCD Lagrangian is a bare parameters. Physical quark masses M_q appear in the theory along the renormalisation group action. This process is renormalisation scheme dependant. However, because of the GMOR relations, one still anticipates $M_q > 0 \iff M_\pi > 0$, $M_q = 0 \iff M_\pi = 0$.

As chiral symmetry is lifted in the one flavour QCD case, in absence of GMOR relation, more freedom is allowed for the renormalisation and the situations $M_q > 0$, $M_q = 0$ can be reached starting from the same bare quark mass [3]. As a result, an ambiguity appears.

2.7 Partially quenched extension of one flavour QCD

It has been chosen to consider the situation where the one flavour model is embedded within an partially quenched extension by adding to the unique quark Ψ_s an extra valence quarks Ψ_V which is *quenched*, so that it does not contribute to the Boltzmann-weight of the gauge configurations.

The contributions from the valence quark Ψ_V can be cancelled through the introduction of a bosonic *ghost quark* $\tilde{\Psi}$ of identical mass m_V [17]. With this construction, the partition function is equivalent to the one flavour QCD version (with unique quark Ψ_s), what can be directly seen considering the theory partition function

$$\begin{aligned} Z = & \int \mathcal{D}A\, \mathcal{D}[\Psi_s \bar{\Psi}_s]\, \mathcal{D}[\Psi_V \bar{\Psi}_V]\, \mathcal{D}[\tilde{\Psi}\bar{\tilde{\Psi}}] \\ \times & \; e^{-S_g - \bar{\Psi}_s(\gamma_\mu D_\mu + m_s)\Psi_s - \bar{\Psi}_V(\gamma_\mu D_\mu + m_V)\Psi_V - \tilde{\Psi}(\gamma_\mu D_\mu + m_V)\tilde{\Psi}} \\ = & \int \mathcal{D}A\, e^{-S_g}\, \frac{\det(\gamma_\mu D_\mu + m_V)}{\det(\gamma_\mu D_\mu + m_V)} \det(\gamma_\mu D_\mu + m_s). \end{aligned}$$

Moreover, the so-called sea sector composed by the Ψ_s quark remains invariant under the partial quenching extension [18].

In addition to this, the setting $m_V = m_s$ restores a chiral symmetry into the extended theory. It can also be shown [19], if the quark masses vanish simultaneously, that the partially quenched theory has a graded chiral symmetry of form

$$SU(N_F|N_V)_L \otimes SU(N_F|N_V)_R, \tag{2.16}$$

where the partially quenched theory has two sectors:

- the fermionic sector, of grade $N_F = 2$, is composed of the see and valence quarks Ψ_s, Ψ_V.
- the bosonic sector, with grade $N_V = 1$, is composed of the ghost quark $\tilde{\Psi}$.

In addition to the "physical" η_s and σ states built on the quark field Ψ_s, the particle spectrum is extended by 8 degenerated pions π^a, $a = \{1, \ldots, 8\}$ satisfying a $SU(3)$-symmetric PCAC relation. In that context a PCAC-quark mass can be introduced [64] and the one flavour theory is extended into the well known frame of multicolour QCD. This allows for consistency checks (with partially quenched

chiral perturbation theory (PQχPT) and an extended particle spectrum) and to test definitions for the one flavour quark mass (PCAC quark mass?).
As the theory is realised, only the sea sector is simulated. The "partial quenching frame" is completely virtual in that sense that its implementation concerns the analysis only.

i

Chapter 3

Theories on the lattice

riesonthelattice.tex

3.1 Introduction

A hypercubic, finite sized lattice is considered as a discretisation of the Euclidean space-time. It can be used as natural regularisation for a quantum field theory in Euclidean space path integral formulation. In such a formulation, the quark fields live on the lattice points and are indexed with an $x \in \mathcal{Z}_4$, while gauge fields are associated with links $(x,\, \hat{\mu})$, with $\mu = 1,\, 2,\, 3,\, 4$ labelling the lattice directions. The lattice spacing is constant and fixed by a.

In this setup, derivatives can be replaced by difference operators. The forward and backward difference operators are defined as $(a = 1)$

$$\partial^{\mu}_{x,\,y} = \delta_{x+\hat{\mu},\,y} - \delta_{x,\,y}, \qquad \partial^{\mu\ *}_{x,\,y} = \delta_{x,\,y} - \delta_{x-\hat{\mu},\,y}.$$

With this, a massless free fermion action, with fermion fields $\{\psi_x\}$ can be constructed as:

$$\frac{1}{2}\sum_{x,\,y} \bar{\psi}_x \gamma_\mu (\partial^{\mu}_{x,\,y} + \partial^{\mu\ *}_{x,\,y})\psi_y$$

For a theory with gauge interaction (colour group $SU(N_c)$), a parallel transporter is included in the finite differential operator to ensure gauge invariance.

$$\nabla^{\mu}_{x,\,y} = U(x,\,\mu)\delta_{x+\hat{\mu},\,y} - \delta_{x,\,y}, \qquad \nabla^{\mu\,*}_{x,\,y} = \delta_{x,\,y} - U(x-\hat{\mu},\,\mu)^{\dagger}\delta_{x-\hat{\mu},\,y},$$

whereas $U(x,\,\mu) \in SU(N_c)$, where it can be expressed, in terms of the vector potential, A_μ as

$$U(x,\,\mu) = \mathcal{P}\exp\left[i\int_0^1 d\tau\, A^{\mu}(x + (1-\tau)\hat{\mu})\right].$$

$\mathcal{P}$ denotes a τ-ordering and $A_\mu \in SU(N_c)$. On the lattice, for a path C running on lattice links $b \in$ C, the parallel transporter becomes $U(\mathrm{C}) \equiv \prod_{b\in \mathrm{C}} U(b)$. Under gauge transformation, $U(x,\,\mu)$ transforms as $\tilde{U}(x,\,\mu) = V(x)U(x,\,\mu)V^{\dagger}(x+\hat{\mu})$, $V(x) \in SU(N_c)$.

This implies gauge invariance for the following quantities

$$\bar{\psi}_x \nabla_{x,y} \psi_y, \quad \mathrm{Tr}\, U(C_{xx}),$$

C_{xx} denoting some closed path. Thus, a first naive, local gauge invariant action reproducing a theory like QCD in the continuum limit ($a \to 0$) is given by

$$S_{naive} = -\frac{2}{g^2} \sum_p \mathrm{ReTr}(U_p) + \sum_{x,y} \bar{\psi}_x D_{x,y} \psi_y, \tag{3.1}$$

where U_p are fixed to be the smallest closed loops or plaquette (directed product of 4 neighbouring link matrices $U_{x,\mu}$) and

$$D_{x,y} = \frac{1}{2} \gamma^\mu (\nabla^\mu + \nabla^{\mu *})$$

is the naive Dirac operator.

3.1.1 Doublers and Nilsen-Ninomiya No-Go theorem

However, the lattice action in eq.(3.1) is "contaminated" by fermionic "doublers". Put in the Fourier space, the free Dirac operator

$$\tilde{D}(p) = i \sum_\mu \gamma^\mu \sin(p^\mu).$$

exhibits 16 zeros in the first Brillouin zone, at $\{(0,0,0,0),\ (\pi,0,0,0),\ ...,(\pi,\pi,\pi,\pi)\}$.

For the fermionic theory, the general question of a reasonable lattice discretisation should be adressed bearing in mind the following Theorem:

NO-GO Theorem (Nielsen-Ninomiya) The following conditions can not hold simultaneously:

1. $D(x)$ is local.
2. $\tilde{D}(p)$ behaves for $p << 1$ as $i\gamma^\mu p^\mu + \mathcal{O}(p^2)$.
3. There are no doublers.
4. $\gamma_5 D + D\gamma_5 = 0$ (chiral symmetry) holds.

The Wilson approach choses to sacrifice the condition 4. For a general discussion concerning chiral symmetry and alternative choices of operators, see for example [53].

3.1.2 Wilson-Dirac operator

Following this strategy, Wilson suggested a modified Dirac operator

$$D_W = \frac{1}{2}[\gamma^\mu (\nabla^\mu + \nabla^{\mu *}) - r \nabla^\mu \nabla^{\mu *}]. \tag{3.2}$$

The additional term $\nabla^\mu \nabla^{\mu *}$ breaks the chiral symmetry, but gives large masses to the doublers, while leaving the pole at $p = 0$ unchanged. This has for effect to quench out the doubler contributions. By construction, the Wilson term vanishes as $a \to 0$, where the continuum theory is expected to be restored.

3.2 Wilson-Dirac operator eigenspectrum

3.2.1 From continuum to the Wilson formulation on the lattice

As the space-time is discretised and the volume made finite, the continuous fields are replaced by discrete variables and the allowed momentum components are the discrete elements of the Brillouin zone $\mathbf{q} \equiv \{q_k = \frac{2\pi}{L}\nu_k;\ \ k = 1, 2, 3\}$, $0 \leq \nu_k \leq L-1$. The Dirac operator Eigenspectra for the theory in continuum with finite and infinite volumes are sketched on the left part of Fig.(3.1).

For the free case ($U_\mu = 1$), consider the Wilson-Dirac action which, in the momentum space ($\psi(x) = \int dq\, \exp(iqx)\tilde{\psi}(q)$), turns out to be

$$D_W = m + \frac{1}{a}\sum_\mu (i\sin(p_\mu)\gamma_\mu + 1 - \cos(p_\mu)), \qquad r = 1.$$

One observes that the Wilson term has for effect to map the eigenvalues from the vertical line onto the complex plane. In addition to this, considering the doublers, one observes that the mass term is shifted $m \to m + 2ra^{-1}n_\pi$, with n_π the number of momentum components equal to π. This picture is sketched in Fig.(3.1), in the right window.

Further comments can be made considering the following additional features.

In continuum:

γ_5-symmetry (or chiral invariance) With $D = \gamma^\mu D_\mu$, it follows from the definition of $\gamma_5 = i\gamma_0\gamma_1\gamma_2\gamma_3$ and $\{\gamma^\mu,\, \gamma^\nu\} = \gamma^\mu\gamma^\nu + \gamma^\nu\gamma^\mu = 2g^{\mu\nu}$, that

$$\{D,\, \gamma_5\} = 0,$$

where γ_5 acts on the spinor space.

Eigenvalues D is anti-hermitian, as a result, its eigenvalues are strictly imaginary and D is normal. Therefore, it is equivalent to consider left or right eigenvalues. It holds $D\gamma_5 v_\lambda = -\gamma_5 D v_\lambda = -\lambda_D \gamma_5 v_\lambda$, and the eigenvalues $\{\lambda_D,\, -\lambda_D\}$ come in pairs, with their orthonormal eigenvectors $\{v_\lambda,\, \gamma_5 v_\lambda\}$.

On the lattice:

It is standard to reorganise the Wilson-Dirac operator using the following notations

$$D_W[U] \equiv D_{yd,\,xc}[U] = \delta_{yx}\delta_{dc} - \kappa\sum_{\mu=1}^{4}[\delta_{y,\,x+\mu}(1+\gamma_\mu)U_{dc,\,x\mu} + \delta_{y+\mu,\,x}(1-\gamma_\mu)U^T_{dc,\,y\mu}], \tag{3.3}$$

where the *Hopping parameter* κ controls the parameters dependance and is defined as

$$\kappa \equiv \frac{1}{2am + 8r}. \tag{3.4}$$

The *Hopping matrix* M is introduced as the Wilson-Dirac operator is rewritten $D_W = \mathbf{1} + \kappa M$.

Eigenvalues and eigenvectors D_W is non-normal and for reasons discussed in the appendix B, its left $\{\langle L_\lambda|\}$ and right $\{|R_\lambda\rangle\}$ eigenvectors have to be treated distinctly. The Wilson-Dirac operator is local, thus, for the lattice points x, $y \in \mathcal{Z}_4$, one decomposes the eigenvectors as $|R_\lambda\rangle = \sum_x |R_{\lambda,\,x}\rangle$, with

$$\sum_y \quad D_{W,\,xy}\,|R_{\lambda,\,y}\rangle = \lambda\,|R_{\lambda,\,x}\rangle \iff D_W\,|R_\lambda\rangle = \lambda\,|R_\lambda\rangle\,, \tag{3.5}$$

$$\sum_y \quad \langle L_{\lambda,\,y}|\,D_{W,\,yx} = \lambda\,\langle L_{\lambda,\,x}| \iff \langle L_\lambda|\,D_W = \lambda\,\langle L_\lambda|\,,$$

$$\langle L_\lambda|R_\lambda\rangle = \textstyle\sum_x \langle L_{\lambda,\,x}|R_{\lambda,\,x}\rangle\,. \tag{3.6}$$

γ_5-hermiticity The continuum γ_5-symmetry takes the form

$$D_W^\dagger = \gamma_5 D_W \gamma_5. \tag{3.7}$$

From eq.(3.5) , one has $\sum_y \gamma_5 D_{W,\,xy}\gamma_5\gamma_5\,|R_{\lambda,\,y}\rangle = \lambda\gamma_5\,|R_{\lambda,\,x}\rangle$. γ_5-hermiticity gives $\sum_y D^\dagger_{W,\,yx}\gamma_5\,|R_{\lambda,\,y}\rangle = \lambda\gamma_5\,|R_{\lambda,\,x}\rangle$ and it follows

$$\langle R_{\lambda,\,y}|\,\gamma_5 D_{W,\,yx} = (|R_{\lambda,\,y}\rangle)^\dagger\gamma_5 D_{W,\,yx} = \lambda^*(|R_{\lambda,\,x}\rangle)^\dagger\gamma_5 = \lambda^*\,\langle R_{\lambda,\,x}|\,\gamma_5. \tag{3.8}$$

This implies that the complex eigenvalues of D_W, $\{\lambda_D\}$ show up in conjugate eigenpairs $\{\lambda_D,\,\lambda_D^*\}$. This discussion is completed in appendix B.

Even-odd parity Consider the operator $\Xi(x,y) = (-1)^{x_1+\ldots+x_2}\delta_{(x-y)} \otimes 1_{spinor} \otimes 1_{color}$, having the property $\Xi^2 = 1$, $\Xi^+ = \Xi$. One can show

$$\Xi M \Xi = -M.$$

It follows that the Wilson-Dirac operator eigenvalues are paired $1 \pm \kappa\lambda_M$, where λ_M are Hopping matrix M eigenvalues.

Boundedness It can be shown that the eigenspectrum λ_M of M is bounded [35] as

$$|\lambda_M| < 8r. \tag{3.9}$$

3.2.2 The non-hermitian Wilson-Dirac operator D_W eigenspectrum

Because of the above discussion, the eigenvalues are expected to lie within a bounded area. For the free fermions, the eigenspectrum is realised as above and exhibits horizontal and vertical symmetries because respectively of γ_5-hermiticity and even-odd parity.

Doublers regions appear in the picture as shifted versions of the physical eigenspectrum, which lies on the left. As a resulting artefact, four holes appear in Fig.(3.1). As the continuum is approached, the doublers are washed out to the right.

As they come into the picture, the complex fields complicate the eigenspectrum in Fig.(3.1). With increasing κ, the eigenspectrum is more and more

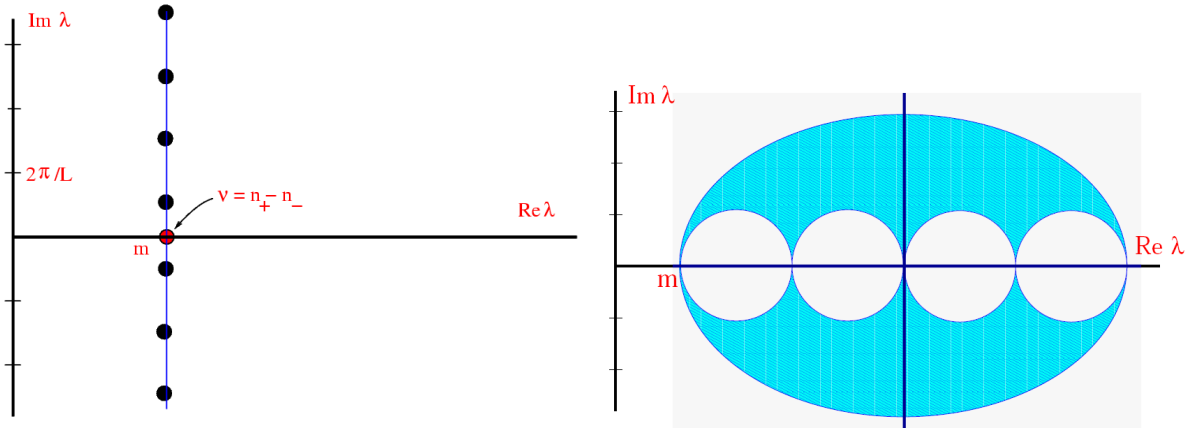

Figure 3.1: On the left, the Dirac operator eigenspectrum is sketched in continuum. Its eigenvalues are continuously spread along the line and get discretised values as boundaries are fixed. On the right, the free Wilson-Dirac operator is schematically sketched. Its eigenvalues lie within the blue domain.

deformed, new real eigenpairs appear and the eigenspectrum is expanded while the lowest eigenvalues are shifted in the direction of the left half of the complex plane.

Recall that the fermionic mass takes the form of the $\det(D_W) = \prod_{i=0}^{N} \lambda_i$. Therefore, configurations with eigenvalues distributed very close to zero have the tendency to be underrepresented in principle, for statistical and algorithmic reasons [56].

For one flavour QCD, in connection to the problem of defining a mass in this theory, an intriguing issue is the eigenspectrum behaviour as the bare quark mass is successively reduced (κ increased). This is discussed for the interacting theory in Fig.(3.2).

3.2.3 Hermitian Wilson-Dirac operator

On the lattice, it follows from $D_W^\dagger = \gamma_5 D_W \gamma_5$ that D_W admits a normal, hermitian version

$$Q \equiv \gamma_5 D_W . \tag{3.10}$$

3.2.4 Eigenvalues of Q vs eigenvalues of D_W

In continuum

For D_0, the massless non-hermitian Wilson-Dirac operator, one has $D_0 v_\lambda = i\lambda v_\lambda$, $\lambda \in \mathrm{R}$. Thus, for $D = D_0 + m$, one obtains $D v_\lambda = \lambda^m v_\lambda$, with $\lambda^m = (i\lambda + m)$.

Now, by chiral symmetry $\{\gamma_5, D_0\} = 0$, it comes $\gamma_5 v_\lambda = v_{-\lambda}$. Let $Q = \gamma_5 D$, one has $Q v_\lambda = \gamma_5 (D_0 + m) v_\lambda = (-D_0 + m)\gamma_5 v_\lambda = (i\lambda + m) v_{-\lambda}$. Therefore, in

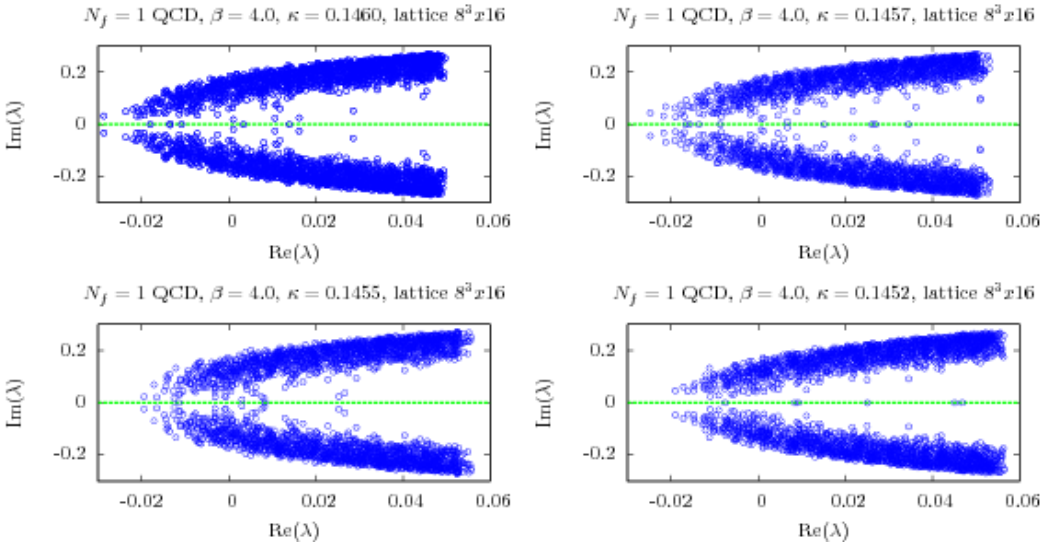

Figure 3.2: For $N_f = 1$ QCD and for 8^3x16 lattices, the lowest part of 5 configurations generated with different κ's are compared. As expected, D_W's eigenspectrum is shifted onto the negative part of the complex plane as κ is increased. The eigenvalues are concentrated on the outer boundaries while the inner eigenspectrum is less "inhabited".

the subspace spanned by $\{v_\lambda, v_{-\lambda}\}$, Q reads

$$Q = \begin{pmatrix} 0 & i\lambda + m \\ -i\lambda + m & 0 \end{pmatrix}.$$

Diagonalisation gives

$$\lambda_Q = \pm\sqrt{\lambda^2 + m^2} = \pm|\lambda^m|, \qquad v_Q = \begin{pmatrix} 1 \\ \pm\frac{m-i\lambda}{\sqrt{\lambda^2+m^2}} \end{pmatrix} \tag{3.11}$$

On the lattice

Astonishingly, there is no known analytic relation between the eigenvalues of Q, $\{\lambda_Q\}$ and of D_W, $\{\lambda_D\}$. However, the experience shows that small eigenvalues for one operator strongly hint at small eigenvalues for the other one. This knowledge will be discussed further in chapter 7.
Obviously, it holds

$$D_W |R_\lambda\rangle = 0 \Longleftrightarrow \gamma_5 D_W |R_\lambda\rangle = Q |R_\lambda\rangle = 0. \tag{3.12}$$

For that reason, one can get a whole set of real eigenvalues of D_W considering

$$\mathcal{H}(\rho) = \gamma_5(D_W - \rho 1).$$

This, because for the set $\{\{\lambda\}, \{|R_\lambda\}\rangle\}$ of real eigenvalues/eigenvectors of D_W, there is a value ρ_λ for which

$$\gamma_5(D_W - \rho_\lambda 1) |R_\lambda\rangle = \mathcal{H}(\rho_\lambda) |R_\lambda\rangle = 0. \tag{3.13}$$

The spectral flow method described in section 4.3 is based on this mapping between the zero modes of both non-hermitian and hermitian operators D_W and Q.

3.2.5 Even-odd preconditioned Dirac-Wilson operator

The preconditioning idea is useful to accelerate the convergence of different inversion algorithm. In addition to this, its use also improves the determinant sign computations (see section 6.5.1).

The Hopping matrix M connects the even sites to the odd ones and inversely (see for example [12]), whereas the denomination odd-even is given by a simple numbering on the four-dimensional lattice. The even/odd fields ψ_{even}/ψ_{odd} and the corresponding even-odd preconditioned Dirac operator $\tilde{D}$ read

$$\Psi \equiv \begin{pmatrix} \psi_{even} \\ \psi_{odd} \end{pmatrix}, \quad \tilde{D} = \begin{pmatrix} 1 & \kappa M_{eo} \\ \kappa M_{oe} & 1 \end{pmatrix}.$$

This construction is based on the identity

$$\det \begin{pmatrix} A & B \\ C & D \end{pmatrix} = \det(A) \det(D - CA^{-1}B),$$

which ensures the determinant conservation under the so-called LU decomposition:

$$D_{prec} \equiv L^{-1}\tilde{D}U = \begin{pmatrix} 1 & 0 \\ 0 & 1 - \kappa^2 M_{oe}M_{eo} \end{pmatrix},$$

where

$$L \equiv \begin{pmatrix} 1 & 0 \\ -\kappa M_{oe} & 1 \end{pmatrix}, \quad U = \begin{pmatrix} 1 & -\kappa M_{eo} \\ 0 & 1 \end{pmatrix}.$$

Preconditioned Dirac-Wilson operator eigenvalues

Let $v = (v_e, v_o)$, $v_o \neq 0$ the even-odd decomposition of D_W's right eigenvector with eigenvalue λ. From above, it comes

$$\kappa M_{eo} v_o = (1 - \lambda) v_e,$$
$$\kappa M_{oe} v_e = (1 - \lambda) v_o$$

Thus, for D_{prec}, one gets

$$D_{prec} v_o = (1 - \kappa^2 M_{oe} M_{eo}) v_o = v_o - \kappa M_{oe}(1 - \lambda) v_e \tag{3.14}$$
$$= v_o - (1 - \lambda)^2 v_o = \left(2\lambda - \lambda^2\right) v_o. \tag{3.15}$$

One finds the relation

$$\lambda_{prec} = 2\lambda - \lambda^2. \tag{3.16}$$

In addition to this, notice that the preconditioning matrix conserves the γ_5-hermiticity. The non-hermitian Wilson-Dirac operator and its preconditioned version eigenspectra are shown in Fig.(3.2).

3.3 Wilson-Dirac operator eigenvalues

Since the real eigenvalues of the lattice Wilson-Dirac operator are of central importance in general and in this work, they deserve a special treatment.

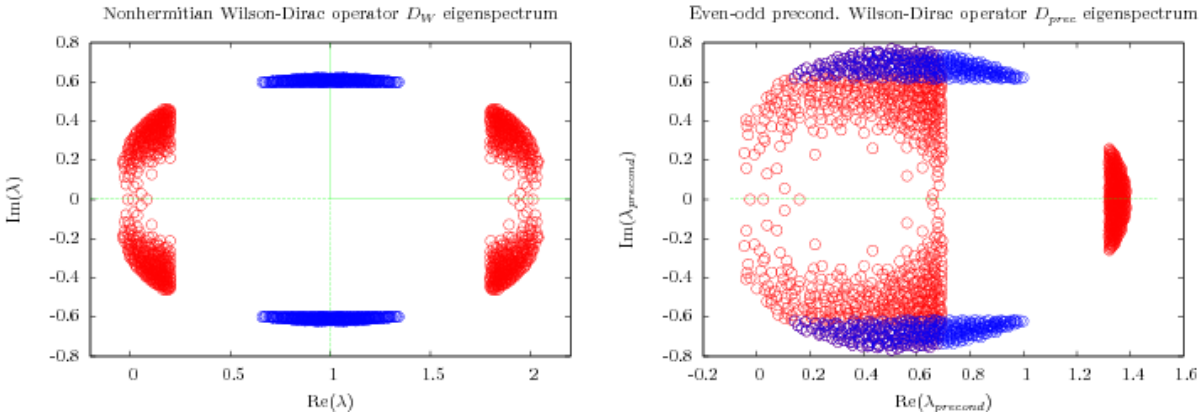

Figure 3.3: A sketch of the non-hermitian Wilson-Dirac operator eigenspectrum on the left and of its preconditionned counterpart on the right. The eigenvalues were computed on a 6^4 test configuration, for one flavour QCD, making use of the Arnoldi algorithm as explained in the next sections. $D_{precond.}$ conserves the γ_5-hermiticity resulting in a symmetry around the real axis. In practice and for relatively large lattices, the Wilson-Dirac operator D_W eigenspectrum is only partially accessible numerically.

3.3.1 Zero modes in continuum

The zero modes is the set of the Dirac operator D eigenmodes with eigenvalues $\lambda_D = 0$. γ_5-hermiticity ($\{D, \gamma_5\} = 0$) forces the zero modes of D to appear in pairs $\{v_0, (+iE)\}$, $\{\gamma_5 v_0, (-iE)\}$, i.e.

$$Dv_0 = iEv_0 \iff D\gamma_5 v_0 = -iE\,(\gamma_5 v_0)\,. \tag{3.17}$$

For there corresponding chirality, $\chi \equiv (v_0, \gamma_5 v_0)$, one obtains

$$\chi = (v_0, \gamma_5 v_0) \neq 0 \iff E = 0. \tag{3.18}$$

Thus:

- Only zero modes can have a non-vanishing chirality in continuum. The chiralities pick a values $\chi = +1$ or $\chi = -1$.

Among other issues, it is worth mentioning that the continuum zero modes are connected to the topology:

- The Atiyah-Singer Index theorem connects zero modes chirality and the topological density $\nu[A] = n_+ - n_-$, whereas n_+, n_- are the number of zero modes with respectively positive and negative chirality.

3.3.2 Pseudo zero modes on the lattice

For right eigenvalues/eigenvectors pairs $\{|R_\lambda\rangle\,, \lambda\}$, the lattice chirality reads $\chi_{latt.} \equiv (|R_\lambda\rangle)^\dagger \gamma_5 |R_\lambda\rangle)$ (a sum over space-time elements, the number of flavour and colours is implied). With γ_5-hermiticity, one finds

$\lambda^*(|R_\lambda\rangle)^\dagger\gamma_5 \left|R_{\tilde{\lambda}}\right\rangle = \left(|R_\lambda\rangle)^\dagger\gamma_5\right) D_W \left|R_{\tilde{\lambda}}\right\rangle = \tilde{\lambda}(|R_\lambda\rangle)^\dagger\gamma_5 \left|R_{\tilde{\lambda}}\right\rangle$, which leads to the conclusion

$$\chi_{latt.} \equiv (|R_\lambda\rangle)^\dagger\gamma_5 |R_\lambda\rangle) \neq 0 \iff \lambda = \lambda^*. \tag{3.19}$$

- Only the Dirac-Wilson operator real eigenvalues have non-vanishing chiralities.
- Eigenvector chiralities is realised within the boundaries $\{[-1,\, 0],\, [0,\, +1]\}$ (see chapter 8 and [40]).
- The lattice version of the Index theorem exists on the lattice with $\nu[A] = n_+ - n_-$.

This analogy with the zero-modes in continuum supports the interpretation of the lattice Wilson-Dirac real eigenvalues as lattice zero modes (remnants of the continuum zero modes).

3.3.3 Spectral decompositions

In order to illustrate the role of the Dirac eigenvalues/eigenvectors in the theory, recall the standard form of the generating functional of the Green function, expressed with Grassmannian sources $\{\eta,\, \bar{\eta}\}$ localised on the lattice points.

$$Z[\eta,\, \bar{\eta}] = \int [d\bar{\psi}\, d\psi] \exp\{-\sum_{x,\, y} \bar{\psi}_y D_{W\, yx} \psi_x + \sum_x [(\bar{\eta}_x \psi_x) - (\bar{\psi}_x \eta_x)]\}. \tag{3.20}$$

It comes

$$\langle \psi_y \bar{\psi}_x \rangle = \partial_{\bar{\eta}_y} \partial_{\eta_x} \frac{Z[\eta,\, \bar{\eta}]}{Z[0,\, 0]}|_{\eta=\bar{\eta}=0} = D^{-1}_{W\, yx} = \Delta_{yx}, \tag{3.21}$$

which gives the propagator. Alternatively, the propagator can be expressed by its eigenvalues/eigenvectors of D_W, as derived in appendix B,

$$D^{-1}_{W\, xy} = \sum_\lambda \frac{1}{\lambda} \frac{|R_{\lambda,\, x}\rangle\langle L_{\lambda,\, y}|}{\langle L_\lambda | R_\lambda \rangle}, \tag{3.22}$$

Thus, the knowledge of the whole eigenvalues/eigenvectors set would allow for the reconstruction of the full theory. Therefore, the eigenvalues/eigenvectors distribution not only provides with a footprint of realised lattice configurations.

From eq.(3.22), one can guess that the low eigenspectrum probably plays a crucial role in the spectral decompositions. Because of this, techniques reconstituting correlation functions, the topological charge from a limited amount of eigenvalues/eigenvectors (in the low eigenvalues spectrum) were developed (as stochastic estimator or the spectral decompositions presented in chapter 8).

The pseudoscalar condensate $\langle \bar{\psi}\gamma_5\psi \rangle$

The pseudoscalar condensate reads, in more explicit notations

$$\langle \sum_x \bar{\psi}_x \gamma_5 \psi_x \rangle = \mathrm{Tr}_x\, (D^{-1}_W \gamma_5). \tag{3.23}$$

Notice $\sum_x \partial_{\eta_x} \gamma_5 \partial_{\bar{\eta}_x} = -\sum_x \gamma_5 \partial_{\eta_x} \partial_{\bar{\eta}_x} = \sum_x \gamma_5 \partial_{\bar{\eta}_x} \partial_{\eta_x}$, which application on $\frac{Z[\eta,\, \bar{\eta}]}{Z[0,\, 0]}|_{\eta=\bar{\eta}=0}$ with eq.(3.21) leads to eq.(3.23).

3.4 Theories on the lattice in the Wilson formalism

3.4.1 One flavour QCD

In explicit notations, the quark field dependant part of the Wilson lattice action reads $S_f = \sum_x \bar{\psi}^a_x D_W \psi^a_x$. With D_W as in eq.(3.3), we have explicitly

$$S_f = \sum_x \{\bar{\psi}^a_x \psi^a_x - \kappa \sum_{\mu=1}^{4} [\bar{\psi}^a_{x+\hat{\mu}}(1+\gamma_\mu) U_{ab,\,x\mu} \psi^b_x + \bar{\psi}^a_x (1-\gamma_\mu) U^T_{ab,\,x\mu} \psi^b_{x+\hat{\mu}}]\}, \quad (3.24)$$

where the *hopping parameter* κ is as in eq.(3.4).

3.4.2 $\mathcal{N} = 1$ Sym on the lattice

Supersymmetry can not be defined in a straightforward way on the lattice, as the discretisation leaves no generators of the Poincarré algebra and adds doublers in the fermionic sector. However, for $\mathcal{N} = 1$ Sym, a Wilson lattice formulation is expected to restore supersymmetry in the continuum limit [46].

Recall that the $\mathcal{N} = 1$ Sym theory contains Majorana fermions in their adjoint representation. For its realisation, consider the lattice Wilson fermionic action [45]

$$S_f = \sum_x \{\bar{\psi}^a_x \psi^a_x - \kappa \sum_{\mu=1}^{4} [\bar{\psi}^a_{x+\hat{\mu}} V_{ab,\,x\mu}(1+\gamma_\mu)\psi^b_x + \bar{\psi}^a_x V^T_{ab,\,x\mu}(1-\gamma_\mu)\psi^b_{x+\hat{\mu}}]\},$$

where $\kappa = \frac{1}{2am_g+8}$, $r = 1$ and $V_{x,\,\mu}$ is defined from the fundamental link variables $U_{x\mu} \in SU(N_c)$ through

$$V_{ab,\,x\mu} \equiv V_{ab,\,x\mu}[U] \equiv 2\mathrm{Tr}(U^+_{x\mu} T_a U_{x\mu} T_b) = V^*_{ab,\,x\mu} = (V^{-1}_{ab,\,x\mu})^T.$$

Plaquettes entering the gauge action are now built on $V_{ab,\,x\mu} \in \mathrm{Adj}_{SU(N_c)}$.

In order to obtain the lattice formulation for a theory with Majorana fermions, consider the following relations

$$\lambda^1 = \frac{1}{\sqrt{2}}(\psi + C\bar{\psi}^T), \qquad \lambda^2 = \frac{i}{\sqrt{2}}(-\psi + C\bar{\psi}^T),$$

with λ satisfying the Majorana condition $\bar{\lambda}^j = {\lambda^j}^T C$ $(j = 1, 2)$. The above relations can be inverted as

$$\psi = \frac{1}{\sqrt{2}}(\lambda^1 + i\lambda^2), \qquad \psi_C = C\bar{\psi}^T = \frac{1}{\sqrt{2}}(\lambda^1 - i\lambda^2).$$

Applying this to the action introduced above, one arrives to the following Wilson action

$$S_f = \frac{1}{2}\sum_x \sum_{j=1}^{2} \{\bar{\lambda}^{j\,a}_x \lambda^{j\,a}_x - \kappa \sum_{\mu=1}^{4} [\bar{\lambda}^{j\,a}_{x+\hat{\mu}} V_{ab,\,x\mu}(1+\gamma_\mu)\lambda^{j,\,b}_x + \bar{\lambda}^{j,\,a}_x V^T_{ab,x\mu}(1-\gamma_\mu)\lambda^{j\,b}_{x+\hat{\mu}}]\}.$$

In terms of the of fields in adjoint representation V, this can be formulated with the adjoint Wilson-Dirac operator $D_W[V]$ ($U \leftrightarrow V$ in eq.(3.3)). With this,

$$S_f = \sum_{xc,\, yd} \bar{\psi}_y^d D_{W,\, yd,\, xc}[V] \psi_x^c = \frac{1}{2} \sum_{j=1}^{2} \{ \sum_{xc,\, yd} \bar{\lambda}_y^{j\, d} D_{W,\, yd,\, xc}[V]\, \lambda_y^{j\, c} \} \tag{3.25}$$

Next, comparing formulations built on Dirac or Majorana spinors the fermionic path integrals read

$$\prod_{j=1}^{2} \int [d\lambda^j] e^{-\frac{1}{2} \bar{\lambda}^j D_W[V] \lambda^j} = \det(D_W[V]) = \int [d\bar{\psi} d\psi] e^{-\bar{\psi} D_W[V] \psi}. \tag{3.26}$$

This relation explicitly shows how the theory with Majorana spinors is constructed from a standard formulation with Dirac spinors. Thus, by construction, one finds for the path integral over the Majorana fermion fields the following relation.

$$\int [d\lambda] e^{-\frac{1}{2} \bar{\lambda} D_W[V] \lambda} = \int [d\lambda] e^{-\frac{1}{2} \lambda M \lambda} \equiv \text{Pf.}(M), \quad M \equiv C D_W[V] = -M^T$$

where $\text{Pf.}(M)$ is the *Pfaffian* and C is the charge conjugation matrix. Therefore,

$$\det\left(D_W\right)[V] = \det(M) = [\text{Pf.}(M)]^2. \tag{3.27}$$

Moreover, in addition to γ_5-symmetry, the Wilson-Dirac operator admits the following symmetries, with C the conjugation matrix and $B \equiv C\gamma_5$,

$$\gamma_5 D_W \gamma_5 = D_W^\dagger, \tag{3.28}$$

$$C D_W C = D_W^T. \tag{3.29}$$

For a right eigenvector $|R_\lambda\rangle$, one has $D_W |R_\lambda\rangle = \lambda |R_\lambda\rangle$. Using alternatively 3.28 and 3.29, one can show the following relations:

$$\begin{aligned} D_W^T C |R_\lambda\rangle = \lambda (C |R_\lambda\rangle) &\Leftrightarrow D_W^\dagger (C |R_\lambda\rangle)^* = \lambda^* (C |R_\lambda\rangle)^* \\ &\Leftrightarrow D_W \gamma_5 (C |R_\lambda\rangle)^* = \lambda^* \gamma_5 (C |R_\lambda\rangle)^*. \end{aligned}$$

Applying eq.(3.28) on the left eigenvectors $(\gamma_5 |R_\lambda\rangle)^\dagger$, it comes:

$$(\gamma_5 |R_\lambda\rangle)^\dagger D_W = (D_W^\dagger \gamma_5 |R_\lambda\rangle)^\dagger = (\gamma_5 D_W |R_\lambda\rangle)^\dagger = \lambda^* (\gamma_5 |R_\lambda\rangle)^\dagger.$$

Therefore, one finds $\{|R_\lambda\rangle, \lambda\}$, $\{\gamma_5 (C |R_\lambda\rangle)^*, \lambda^*\}$ as right eigenpairs and $\{(\gamma_5 |R_\lambda\rangle)^\dagger, \lambda^*\}$, $\{(C |R_\lambda\rangle)^\dagger, \lambda\}$ as left eigenpairs. The eigenpairs were completed making use of eq.(B.4).

Therefore, a degeneracy of order 2 is expected for the (real and complex) eigenvalues. Notice also that the doublers have identical chiralities ($|R_\lambda\rangle^\dagger \gamma_5 |R_\lambda\rangle$), what can be checked by a trivial computation.

In this scheme, for each lattice spacing, a necessary condition for the realisation of supersymmetry (in the continuum limit) requires a careful tuning of κ ($\kappa_{crit.} \sim m_g = 0$). This tuning is made considering the mesonic states or the scalar condensate.

3.4.3 Configurations generation

In the one flavour QCD, the number of colour is fixed to $N_c = 3$ and the gauge fields belongs to $SU(3)$. For $\mathcal{N} = 1$ Sym, the theory is based on the $SU(2)$ colour symmetry.

The dynamic realisation of those theories is based on polynomial hybrid Monte-Carlo (PHMC), two step multi-boson algorithm (see [47]) with tree level Symanzik improved action and stout smearing (among others, see [64], [59] for complements).

Chapter 4

The Sign Problem

4.1 Generalities

Consider first the quantum mechanical partition function

$$Z = \mathrm{Tr}[\exp(-\beta\hat{H})], \quad \beta = \frac{1}{T},$$

where T is the temperature. An equivalent formulation is constructed in the path integral formalism setting $\beta = \frac{i}{\hbar}(t' - t) = La$. As usual, the time was divided into imaginary intervals of length a. In a next step, one introduces a complete set of basis states (in the bra and ket formalism $\{|n\rangle\}$) between the operators $\exp(-a\hat{H})$. The resulting transfer matrix elements are of the form $\left\langle n\middle|\exp(-a\hat{H})\middle|n'\right\rangle$.

At this point, depending on the basis choice, this quantity can be complex, real positive and negative. Since we assume $\hat{H}$ to be hermitian, $Z \in \mathrm{R}$ and for some path $\mathcal{P}$, the Boltzmann factor takes the general form

$$\mathrm{Sgn}[\mathcal{P}]|\exp(-S[\mathcal{P}])|,$$

where $\mathrm{Sgn}[\mathcal{P}] \equiv \pm 1$ fixes the Boltzmann weight sign.

Notice now that one could in principle choose a Hamiltonian eigenvectors basis such that $H|n\rangle = E_n|n\rangle$. In that case, $\mathrm{Sgn}[\mathcal{P}] = 1$ is fixed, since $\left\langle n\middle|\exp(-a\hat{H})\middle|n'\right\rangle = \exp(-aE_n)\,\delta_{n',\,n}$. However, this basis is obviously not known for the cases considered there.

For simulations, the following point is trivial but of importance: only paths with positive, real Boltzmann weight admit a direct statistical interpretation. This is not the case anymore if Boltzmann weights can also become negative.

Luckily, this issue can be circumvented if the measure sign is known. Consider an observable $\mathcal{O}$, in the formalism introduced above, its statistical average over the whole set of paths $\{\mathcal{P}\}$ can be redefined as

$$\langle\mathcal{O}\rangle = \frac{1}{N_{\mathcal{P}}}\sum_{\mathcal{P}}^{N_{\mathcal{P}}}\mathcal{O}[\mathcal{P}]\,\mathrm{Sgn}[\mathcal{P}_n]\,|\exp(-S[\mathcal{P}_n])| = \frac{\langle\mathcal{O}\,\mathrm{Sgn}\rangle_{||}}{\langle\mathrm{Sgn}\rangle_{||}},$$

where $\langle ... \rangle_{||} = \frac{1}{N_{\mathcal{P}}} \sum_n \, ... \exp(-S[\mathcal{P}_n])$. Truncating the observables $\mathcal{O} \to \{\mathcal{O}, \text{sgn}\}$ restores the path integral including negative weights.

However, the modified averages may be completely spoiled by the determinant sign. In order to show this, the above statistical average is decomposed into its positive and negative contributions

$$\langle \mathcal{O} \rangle = \frac{\sum_i^{N_+} \mathcal{O} - \sum_i^{N_-} \mathcal{O}}{N_+ - N_-},$$

where N_+, N_- are the numbers of paths with positive resp. negative measure respectively. From this, one easily sees that the sign fluctuations of the statistical weight can play a critical role on the averages if ($N_+ \approx N_-$) (or even worse $N_+ = N_-$).

4.2 Sign problem in the one flavour theories

4.2.1 One flavour QCD

Recall that the partition function reads

$$Z = \int [dA \, d\bar{\psi} \, d\psi] \, \exp(-S_g(A) + \bar{\psi} D_W(A) \psi) = \int [dA] \, \exp(-S_g(A)) \det(D_W(A)).$$

$\det(D_W(A))$ can take a negative value and $\sigma_{QCD} \equiv \text{Sgn}(\det(D_W(A))) = \pm 1$. For some observable $\mathcal{O}$, one gets the following corrected expectation value

$$\langle \mathcal{O} \rangle_{e^{S_g + S_f}} = \frac{\int dA [\mathcal{O} \, \sigma_{QCD}] \, |\det(D_W(A)) e^{-S_g(A)}|}{\int dA [\sigma_{QCD}] \, |\det(D_W(A)) e^{-S_g(A)}|} = \frac{\langle \mathcal{O} \, \sigma_{QCD} \rangle_{|e^{S_g + S_f}|}}{\langle \sigma_{QCD} \rangle_{|e^{S_g + S_f}|}}. \quad (4.1)$$

Through a similarity transformation, the Dirac operator can be diagonalised and $\det(D_W(A)) = \prod_i^N \lambda_i$. Therefore, all the information about the fermionic measure sign is concentrated in the eigenspectrum. However, as seen in Chapter 3, the hermitian and non-hermitian versions of the Wilson-Dirac operator have very different eigenspectra.

Hermitian Wilson-Dirac operator

In term of its hermitian version eigenvalues $\lambda_Q \in \mathrm{R}$, the Wilson-Dirac operator determinant reads

$$\det[Q(A)] = \prod_{(\lambda_Q)_i \in \mathrm{R}}^{N} (\lambda_Q)_i \, .$$

Under the action of γ_5, approximately one half of the eigenvalues become negative. Thus, the information relevant for the determinant sign is contained in the number of negative eigenvalues N_- or equivalently in the difference between negative resp. positive eigenvalues N_+, resp. N_- and

$$\sigma_{QCD} = (-1)^{N_-}, \quad \sigma_{QCD} = (-1)^{\frac{N_+ - N_-}{2}}.$$

Non-hermitian Wilson-Dirac operator

Because of the vertical and horizontal eigenspectrum symmetries, one finds

$$\det(D_W(A)) = \prod_{\lambda_{D,i}\in \mathrm{R}} \lambda_{D,i} \prod_{\lambda_{D,j}\in \mathrm{C}} |\lambda_{D,j}|^2,$$

because the complex eigenvalues are paired. As a result, the eigenvalues relevant for the sign problem are the real, negative ones and σ_{QCD} is as above.

4.2.2 $\mathcal{N} = 1$ Sym

In the case of $\mathcal{N} = 1$ Sym, the partition function reads (see eq.(3.26))

$$\int [d\lambda]\, e^{-\frac{1}{2}\bar{\lambda} Q \lambda} = \mathrm{Pf.}(M).$$

Thus, in this case $\sigma_{Sym} \equiv \mathrm{Sgn}\,(\mathrm{Pf.}(M))$. For $\mathcal{N} = 1$ Sym, the sign problem comes from the Pfaffian sign and the corrected expectation values are of the same form as in eq.(4.1).

As $\det(D_W[V]) = \prod_{j=1}^{2} \int [d\lambda^j] e^{-\frac{1}{2}\bar{\lambda}^j D_W[V]\lambda^j}$, $\det(D_W[V]) \geq 0$. From eq.(3.27), it thus holds

$$\mathrm{Pf.}(M) = \pm\sqrt{\det(D_W[V])} = \int [d\lambda^j] e^{-\frac{1}{2}\bar{\lambda} D_W[V]\lambda}. \tag{4.2}$$

Therefore, the Pfaffian is real, but can have any sign. In the case of $\mathcal{N} = 1$ Sym, the Pfaffian sign can actually be extracted from the eigenvalues computation. Recall the symmetries listed in eq.(3.28) and eq.(3.29)

$$C D_W[V] C^{-1} = (D_W)^T, \quad B(Q)B^T = (Q[V])^T,$$

impose a degeneracy of order 2 to the eigenvalues. Nevertheless, by construction, only one half of the eigenspectrum has to be considered for the computation of the Pfaffian sign.

Hermitian Wilson-Dirac operator

Since the Wilson-Dirac operator $Q[V]$ eigenvalues $\lambda_Q \in \mathrm{R}$ are paired, $\det[Q[V]]$ is positive since

$$\det[Q[V]] = \prod_i \lambda_Q^2 \geq 0.$$

Recall that the hermitian Wilson-Dirac operator eigenvalues are approximately distributed within two sets of negative resp. positive eigenvalues. In addition to this, the $\mathrm{Pf}(M)$ is a polynomial function. As a result, it is continuous and its sign changes as an eigenvalue λ_Q flips it sign.

Thus, σ_{Sym} is found considering one half of $Q[V]$ eigenvalues. $\mathrm{Pf}(M) = \prod_{i=1}^{N/2} \lambda_{Q_i}$, where $Q[V]$ eigenspectrum is simply taken without degeneracy, which halves the number of considered eigenmodes $N/2$. As for QCD, the Pfaffian sign is given by the number of positive or negative eigenvalues N_+ and N_- (with $N_+ + N_- = N/2$).

$$\sigma_{Sym} = (-1)^{N_-}, \quad \sigma_{Sym} = (-1)^{\frac{N_+ - N_-}{2}}$$

.

Non-hermitian Wilson-Dirac operator and degeneracy lifting

In practice, as a result of D_W non-normality, the Arnoldi algorithm fails to detect the eigenvalue degeneracy in most of the computations. In those cases, the determinant sign computation is identical to the one flavour QCD case. Only the negative real eigenvalues matter.

Nevertheless, the situation becomes ambiguous in the few computations where doublers are detected. Because of this, the eigenvalue doubling in $\mathcal{N} = 1$ Sym is specially discussed in the Appendix C, where a pragmatic solution of this ambiguity is proposed.

4.3 Sign problem computation for one flavour QCD and $\mathcal{N} = 1$ Sym

As showed above, in the Wilson-Dirac formulation, the fermionic measure is given by the Wilson-Dirac eigenvalue spectrum. Depending on the Wilson-Dirac operator considered (D_W or Q), 2 strategies are available.

4.3.1 Non-hermitian Dirac-Wilson operator D_W eigenvalues direct computation

The determinant sign depends on the set $\{\lambda\} \in \mathrm{R}$, $\lambda \leq 0$.

A first approach consists in simply computing, all the negative, real eigenvalues (see Fig.(4.1)). Although real eigenvalues located deep into the eigenspectrum are dificult to extract, this approach was used for this work.

4.3.2 Hermitian Wilson-Dirac operator $Q = \gamma_5 D_W$ and the eigenflow method

As an alternative strategy, the Hermitian Wilson-Dirac operator can be considered. Recall first the Dirac operator decomposition with the Hopping matrix M: $D_W = \mathbf{1} - \kappa M$. From the boundaries conditions on $\lambda_M \leq 8r$ and as $\lambda_{D_W} = 1 - \kappa\,\lambda_M$, one observes that $\kappa \leq \frac{1}{8}$ forces the non-hermitian Wilson-Dirac operator eigenvalues to settle away from 0 such that $\det(D_W) \geq 0$. In turn, the hermitian Wilson-Dirac operator determinant is positive, with eigenvalues distributed into positive and negative sets with even elements (with an even number of elements).

Starting from that situation with $\kappa \leq \frac{1}{8}$, the *eigenflow method* consists in tracking the eigenvalue evolution as κ is smoothly tuned up to $\kappa_{simulation}$, as in Fig.(4.2). A low, real eigenvalue sign flip corresponds to a determinant or Pfaffian sign flip.

However, this method faces several problems increasing dangerously with the lattice size and as the bare quark or gluino mass becomes small or negative:

- Because the κ-steps are finite, the method is not exact or more precisely does not only depend on the eigenvalue computation precision.

  It is not always clear how to trace the eigenvalues flow. Given the data available, one has to trace the most probable eigenvalue flows from several possible. The data is sometimes ambiguous.

- Since the method advances with finite κ-steps, many eigenvalues computations have to be performed. The method becomes slow, in particular for larger lattice, where many small eigenvalues have to be evaluated.

For those reason, this method was disregarded, in the exception of consistency checks for the determinant sign computation.

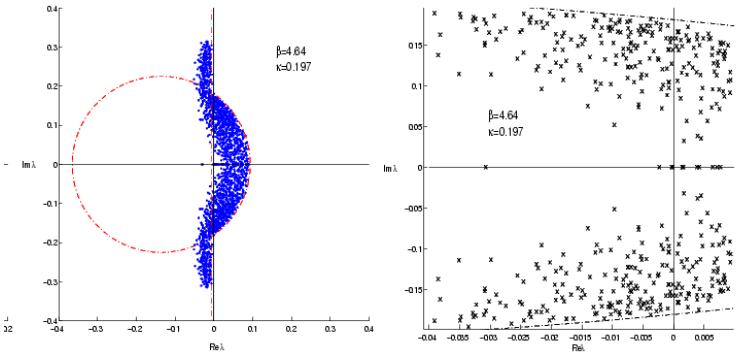

Figure 4.1: For the $N_f = 2$ QCD model with low, degenerated quarks, 100 exceptional (low eigenspectrum is very low) configurations on lattice 8^3x16 were studied in [56]. For clarity, a blow up is proposed on the right. The eigenvalues of the Wilson operator D_W are distributed around zero. Only the real eigenvalues matter for the determinant sign computation.

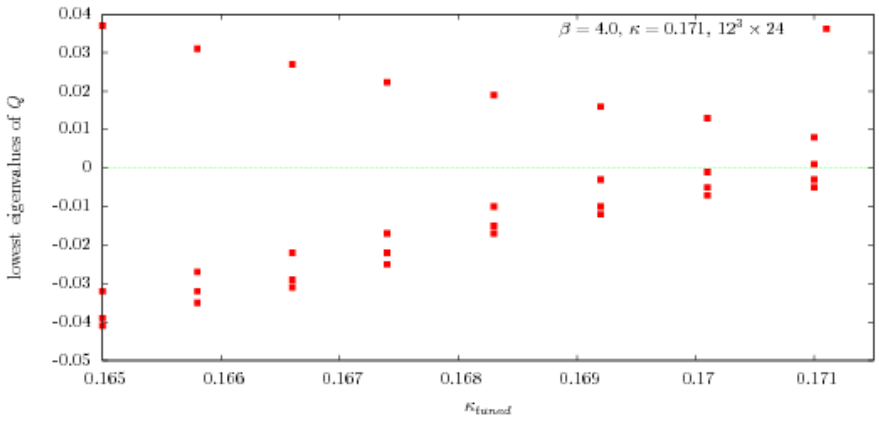

Figure 4.2: Illustration of the conjugate flow method. For a given configuration, the lowest eigenvalues of the Dirac-Wilson hermitian operator are tracked with κ "flowing" between 1/8 and $\kappa_{simulation}$. Crossings of the real axis indicate determinant sign flips. Additional small eigenvalues complicate the pictures and make the computation of the determinant or Pfaffian sign ambiguous.

-

Chapter 5

The Arnoldi algorithm

5.1 The numerical problem

In the last chapter, of two basic strategies introduced for computing the determinant sign, the more direct one consisting in computing D_W's real eigenvalues was selected.

An important practical problem is the huge size of the concerned Wilson-Dirac operators $\mathcal{O}(\text{latt.}^4 * 4 * 3)$, which contain $\mathcal{O}((\text{latt.}^4 * 4 * 3)^2)$ complex elements (recall that typically, latt. ~ 16). In practice, however, these matrices have a sparse structure (see chapter 3) and thus contain $\mathcal{O}(\text{latt.}^4 * 4 * 3)$ non-zero elements. As a result, considering that K eigenvalues have to be computed for the determinant sign evaluation, the eigenproblem scale is of order $K \times \mathcal{O}(\text{latt.}^4 * 4 * 3)$.

The Arnoldi algorithm is specialised for the sparse matrix eigenvalues computational problem. Among other candidates, the Arnoldi algorithm suits the strategy chosen for the Dirac operator determinant sign computation (from D_W, which is non-hermitian, non-normal and non-symmetric). It is the result of considerable theoretical and numerical efforts.

Before the algorithm performances and behaviour are presented in the next section, the Arnoldi algorithm is introduced. The goal is to provide a basic understanding of the method reviewing its underlying main mathematical and technical aspects. The algorithm version used in this work is the parallelised ARPACK version [32]. For more complete introductions, see [22], [24].

5.2 Some basics

5.2.1 Introductory examples

Power method Consider $A \in \mathrm{C}^{n \times n}$, diagonalisable, and let λ_i, x_i be eigenvalue/eigenvector pairs ($1 \leq i \leq n$).
Consider also the eigenvalues to be ordered as $|\lambda_1| > ... \geq |\lambda_n|$, with λ_1 simple and define $\tilde{A} \equiv A/\lambda_1$.

Let $v_0 \in \text{span}\{x_1, x_2, ..., x_n\}$, some vector within the eigenspace spanned by the eigenvectors of A. Let $v_0 = \sum_{i=1}^{n} \gamma_i x_i$, $\gamma_i \in \text{C}$, $\gamma_1 \neq 0$. Therefore, for $k \in \mathcal{N}_+$, one has

$$\tilde{A}^k v_0 = \sum_{i=1}^{n} \frac{A^k x_i}{\lambda_1^k} \gamma_i = x_1 \gamma_1 + \sum_{i=2}^{n} \left(\frac{\lambda_i}{\lambda_1} \right)^k \gamma_i x_i.$$

Obviously, since $|\frac{\lambda_i}{\lambda_1}|^k \to 0 \, (k \to \infty)$ for $2 \leq i \leq n$, $\tilde{A}^k v_0$, will tend to be parallel to x_1. The ratio $\left| \frac{\lambda_2}{\lambda_1} \right|$ gives the algorithmic convergence rate.

Shifted power method The above method can be enhanced considering the simple transformation $\hat{A} \equiv \frac{A - \mu \mathbf{1}}{\lambda_1 - \mu}$. Indeed, the convergence factor introduced above becomes $|\frac{\lambda_2 - \mu}{\lambda_1 - \mu}|$ (compare $\frac{1,1}{1,2}$ and $\frac{0,1}{0,2}$). Obviously, the eigenvalues should be reordered according to the shift.

Power method with polynomial transformation In a similar manner, the convergence may also be improved considering any polynomial transformation of order n, $P_n(x)$:
$\breve{A} = \frac{P_n(A)}{P_n(\lambda_1)}$, whereas the eigenvalues were reordered such that
$|P_n(\lambda_1)| > ... > |P_n(\lambda_n)|$. The new convergence factor reads $\left| \frac{P_n(\lambda_j)}{P_n(\lambda_1)} \right|$.

5.2.2 Schur decomposition

Schur decomposition theorem Let $A \in \text{C}^{n \times n}$, then $\exists Q \in \text{C}^{n \times n}$, unitary, such that

$$AQ = QR, \tag{5.1}$$

- R is upper triangular[1] and contains the eigenvalues of A on its diagonal.
- Q can be chosen such that the eigenvalues λ_i appear in any order along the diagonal.

See [22] for a proof. Obviously, this structure is very interesting for eigenvalue problems and the purpose of the algorithms introduced below is to partially realise this decomposition.

5.2.3 QR algorithms

The QR algorithm In order to realise a Schur decomposition, the power method can be generalised as follows:
Let $A \in \text{C}^{n \times n}$, the QR-decomposition consists in the construction of a sequence $\{A_k\}$ of unitarily similar matrices. Set

$$A_1 = A \equiv Q_1 R_1$$
$$A_{k+1} \equiv R_k Q_k = Q_{k+1} R_{k+1},$$

[1] a matrix is *upper triangular* if its non-zero elements are strictly in the diagonal and above it.

where Q_k, $R_k \in \mathrm{C}^{n\times n}$ are respectively unitary and upper triangular.

A *QR-decomposition* $A = QR$ can always be made and rearranging the terms, it can be seen that $A_{k+1} = Q^\dagger A_k Q = (Q_1 ... Q_k)^\dagger A_1 (Q_1 ... Q_k)$. Under the condition $|\lambda_1| > |\lambda_2| > ... > |\lambda_n|$ on the eigenvalues and under basic assumptions on the eigenspace of A and starting columns of Q_1, it can be shown that the sequence defined above converges against an upper triangular matrix. Additionally, the algorithm convergence rate is $|\lambda_p/\lambda_{p+1}|$.

Shifted QR algorithm In the spirit of the polynomial transformation, consider now a version implementing shifts in the QR-decomposition.

$$Q_s(A_s - \mu_s \mathbf{1}) = R_s,$$
$$A_{s+1} = R_s Q_s^\dagger + \mu_s \mathbf{1},$$

where Q_s, $R_s \in \mathrm{C}^{n\times n}$ are orthogonal and upper triangular respectively. As above, it comes $A_{s+1} = Q_s A_s Q_s^\dagger$, but one can additionally write
$Q_s^\dagger Q_{s+1}^\dagger (R_{s+1} R_s) = (A_s - \mu_s \mathbf{1})(A_s - \mu_{s+1}\mathbf{1})$.
Overall, this corresponds to an iterated QR decomposition for
$M \equiv A_s^2 - (\mu_s + \mu_{s+1}) A_s + \mu_s \mu_{s+1} \mathbf{1}$,

$$\tilde{Q}_s \equiv Q_s Q_{s+1},\ \tilde{R}_s \equiv R_s R_{s+1},$$
$$\tilde{Q}_s \tilde{R}_s \equiv M.$$

Iterating this technique, one can implement polynomial transformations in the QR-decomposition, improving the convergence rates: $\left|\frac{\lambda_p}{\lambda_{p+1}}\right| \to \left|\frac{P_n(\lambda_p)}{P_n(\lambda_{p+1})}\right|$.

5.2.4 Krylov space and Lanczos methods

For large sparse matrices $A \in \mathrm{C}^{n\times n}$ eigenvalues computation, efficient methods are constructed on *Krylov spaces*.

Krylov space: $\mathcal{K}_k(A, v_0) = span\{v_0, Av_0, ..., A^k v_0\}$ can be constructed by a set of an initial vector v_0 (chosen as above, within the space spanned by A's eigenvectors), an iteration number $k \in \mathcal{N}_+$, a matrix A (A can be a matrix multiplication).

5.3 The Arnoldi factorisation

For a general square matrix, the Arnoldi method is an orthogonal projection method for approximating an eigenspectrum subset. The method builds, step by step, a basis for a Krylov subspace.

A k-step Arnoldi factorisation of $A \in C^{n\times n}$ is of the form:

$$AV_k = V_k H_k + f_k e_k^T,$$

where $V_k \in C^{n\times k}$ s.t. $V_k^\dagger V_k = \mathbf{1}$ and has orthonormal columns,
$H_k \in \mathrm{C}^{k\times k}$ and is upper Hessenberg[2],
f_k satisfies $V_k^\dagger f_k = 0$ and is the *residual* .

[2] a matrix is *upper-Hessenberg* if, for each columns, its non-zero elements are strictly just below the diagonal or over it ($A_{i,j} = 0,\ j \in \{i+1, i+2, ...\}$).

The setting $f_k = 0$ realises the *Hessenberg decomposition*:

$$V_k^\dagger A V_k = H_k,\ k \geq 0.$$

A is reduced into an Hessenberg form through an orthogonal projection of A onto the Krylov space $\mathcal{K}_k(A, v_0)$.

From the eigenvalues of H_k, the eigenvalues of A can be retrieved. By the Schur decomposition theorem, $\exists\, Z_k \in \mathrm{C}^{k\times k}$ such that $H_k Z_k = Z_k T_k$, with T_k upper triangular with eigenvalues on its diagonal. Thus, it comes $A(V_k Z_k) = (V_k Z_k)T_k$. More precisely,

Theorem: Arnoldi algorithm convergence for a k-step Arnoldi factorisation of $A \in \mathrm{C}^{n\times n}$, with H_k upper-Hessenberg, it holds:

$$f_k = 0 \iff v_0 = Q_k y,\ y \in \mathrm{C}^n,$$
with $Q_k^\dagger Q_k = \mathbf{1}$, $AQ_k = Q_k R_k$, R_k upper triangular of order k with eigenvalues on its diagonal.
Q_k has orthonormal columns.

The Arnoldi factorisation iteratively transposes a $n \times n$ eigenvalue problem into a $k \times k$ smaller one ($k \ll n$), whose eigenvalues are easy to extract, for example with the QR-decomposition.

5.3.1 Arnoldi factorisation convergence and precision

In practice, $f_k = 0$ never occurs and some evaluation of the numerical precision is needed. Consider a k-step Arnoldi factorisation $AV_k = V_k H_k + f_k e_k^T$. Let y be a normalised eigenvalue of H_k, such that $H_k y = \theta y$ and set $x \equiv V_k y$ ($V_k^\dagger V_k = \mathbf{1}$). The pair ($\theta$, x) is called a *Ritz pair* and it holds

$$\theta = y^\dagger H y = (V_k y)^\dagger A (V_k y) = x^\dagger A x.$$

The Ritz pairs are numerical approximations. Their accuracy can be evaluated through the *Rayleigh quotient residual* $r(x) = Ax - \theta x$. With the vector norm $\|\,.\,\|_2$, it holds

$$\|r(x)\|_2 = \|Ax - \theta x\|_2 = \|(AV_k - V_k H_k)y\|_2 = |\beta_k e_k^T y|,$$

where $\beta_k = \|f_k\|_2$.

The Ritz pairs become exact eigenpairs of A if $f_k = 0$. The Rayleigh quotient residual evaluates the precision and the algorithm iterates until a certain precision threshold is reached for $\|r(x)\|_2$.

5.3.2 Lanczos methods and Krylov subspaces

The connection between the Arnoldi iteration and the Krylov subspaces can be explored more thoroughly (here for the real case) considering the *Krylov matrix*

$$\mathcal{K}_m(A, v_0) = [\ v_0\ Av_0\ \ldots\ A^{m-1}v_0\ ],\qquad A \in \mathrm{R}^{m\times m}.$$

Let $\{e_1, ..., e_n\}$ be an orthonormal basis, consider an orthogonal matrix $V \in \mathrm{R}^{m\times m}$. If $V^T A V = H$, with H upper-Hessenberg, and $v_0 = V e_1$, one has

$$\mathcal{K}_m(A, v_0) = V\,[\ e_1\ He_1\ \ldots\ H^{m-1}e_1\ ],$$

which is a QR-factorisation of $\mathcal{K}_m(A, v_0)$.

Krylov subspaces

The *Rayleigh quotient* is defined as: $r(x) = \frac{x^T Ax}{x^T x}$, $x \neq 0$. Consider A as above, with extremal eigenvalues $\{\lambda_{max}, \lambda_{min}\}$. Suppose $\{q_i\}$ a sequence of orthonormal vectors and the matrix $Q_j = [q_1, \ldots, q_j]$. Then, *the Courant-Fisher Minimax theorem* states that

$$M_j \equiv \max_{y \neq 0} \frac{y^T (Q_j^T A Q_j) y}{y^T y} \leq \lambda_{max},$$
$$m_j \equiv \min_{y \neq 0} \frac{y^T (Q_j^T A Q_j) y}{y^T y} \geq \lambda_{min}.$$

The iteration $\{M_j, m_j\} \rightarrow \{M_{j+1}, m_{j+1}\}$ improves the approximation of $\{\lambda_{max}, \lambda_{min}\}$ (except if $\{\lambda_{max}, \lambda_{min}\} \in \text{span}\{q_1, ..., q_j)\}$). Suppose $u_j, v_j \in \text{span}\{q_1, \ldots, q_j\}$, such that $M_j = r(u_j)$, $m_j = r(v_j)$. One observes that the direction of most rapid convergence for the sequences $\{M_j\}$, $\{m_j\}$ is given by the gradient

$$\nabla r(x) = \frac{2}{x^T x}(Ax - r(x)x) \in \text{span}\{x, Ax\}. \tag{5.2}$$

As a result, one can ensure $M_{j+1} > M_j$ and $m_{j+1} < m_j$, if

$$\{\nabla r(u_j), \nabla r(v_j)\} \in \text{span}\{q_1, \ldots, q_j, q_{j+1}\}. \tag{5.3}$$

Both conditions eq.(5.2) and eq.(5.3) can be simultaneously fulfilled if

$$\text{span}\{q_1, \ldots, q_j\} = \text{span}\{q_1, Aq_1, \ldots, A^{j-1}q_1\} \equiv \mathcal{K}_j(A, q_1).$$

Thus, the eigenvalues evaluation is improved as the Krylov space is expanded. Nevertheless, the method and its efficiency remain completely based on an initial vector v_0.

5.3.3 Dependence of the initial vector

The Arnoldi factorisation proves to be unique in the following sense:

Implicit Q theorem Let $A_k W_k = W_k H_k + f_k e_k^T$ and $A_k U_k = U_k G_k + r_k e_k^T$ be two length k Arnoldi factorisations as above, where W_k, U_k, G_k, H_k, f_k, r_k are as in the above definition.

If the first column of U_k and W_k are identical, then: $G_k = H_k$, $r_k = f_k$.

By construction, v_0 is the first column of the decompositions compared above. Therefore, v_0 completely determines the convergence properties of the k-step Arnoldi factorisation.

5.4 Restarting the Arnoldi algorithm

In turn, the iteration efficiency, the convergence pattern and thus which eigenvalues are extracted are determined by v_0. A further issue concerns the iterative construction of V_k, without loss of numerical orthogonality [27].

Therefore, it becomes interesting to recursively *restart* initial v_0 as linear combination of partially converged eigenvectors. The next subsection describes the final version of the Arnoldi algorithm, as it was developed in [32].

5.4.1 The implicit restarted Arnoldi factorisation or the final project

Let $A \in \mathrm{C}^{n\times n}$, consider again the typical Arnoldi factorisation of length $m = k + p$:

$$AV_m = V_m H_m + f_m e_m^T.$$

This factorisation can be compressed into an other factorisation of order k retaining the eigeninformation of interest. Consider a shifted QR-iteration applying p shifts implicitly:

$$A\tilde{V}_m = \tilde{V}_m \tilde{H}_m + f_m e_m^T Q,$$

where $\tilde{V}_m \equiv V_m Q$, $\tilde{H}_m \equiv Q^\dagger H_m Q$ and $Q \equiv Q_1 Q_2 \ldots Q_p$. Q_j is the orthogonal matrix associated with the j^{th} shift μ_j.

As described in subsection 5.2.4, the shifted QR-iteration is an enhanced power method where shifts are encoded. Thus, those iterations implicitly implement a polynomial transformation

$$v_0 \rightarrow \mathrm{P}_n(A)\, v_0, \quad \mathrm{P}_n(A) = \prod_{i=1}^{n} (A - \mu_i 1).$$

This polynomial is designed such that the convergence properties are improved for a specific eigenspectrum subsector. For doing this, ideas introduced in section 6.2.1 are iteratively realised by internal routines.

It can be shown that $e_m^T Q = (\sigma e_k^T, \hat{q}^T)$, $\hat{q} \in \{e_{k+1}, \ldots, e_{k+n}\}$. As a result, an updated and reduced k-step Arnoldi factorisation is realised

$$A\tilde{V}_k = \tilde{V}_k \tilde{H}_k + f_k e_k^T Q.$$

5.4.2 Basics about eigenvalues selection, deflation and eingenvalues purging

In addition to implicit restarting, the ARPACK Arnoldi algorithm contains additional features. Algorithmic schemes capable of truncating an upper-Hessenberg decomposition (case $f_k = 0$), selecting out wanted eigenvalues and purging unwanted ones were implemented. Such ideas are sketched in this section, avoiding technical details.

Deflation Suppose, after a k-step Arnoldi factorisation

$$H^{(k)} = \begin{bmatrix} H_{11}^k & H_{12}^k \\ \epsilon e_1 e_j^T & H_{22} \end{bmatrix}.$$

If ϵ is small, it may be set to zero. This is a type of *deflation*. Two Hessenberg matrices remain and the eigenvalues contained in H_{11} can be considered to have converged.

Locking After the deflation has taken place, further iterations can be restricted to H_{22} and H_{12}. H_{11}'s eigenvalues were locked in that sense H_{11} will remain unchanged under the next algorithm iterations.

Purging After deflation, it is important to get rid of some unwanted eigenvalues. This can be done by considering simple transformations [26].

Eigenvalues reordering In principle, the Ritz eigenvalues can be reordered from the largest to the smallest, for example. This implies a careful reordering of the corresponding eigenvectors.

5.5 The ARPACK Arnoldi algorithm convergence patterns and its computational modes

The final algorithm, as implemented within the frame of the ARPACK project is a collection of *fortran* 79 routines. The computational modes available are summarised in Fig.(5.1).

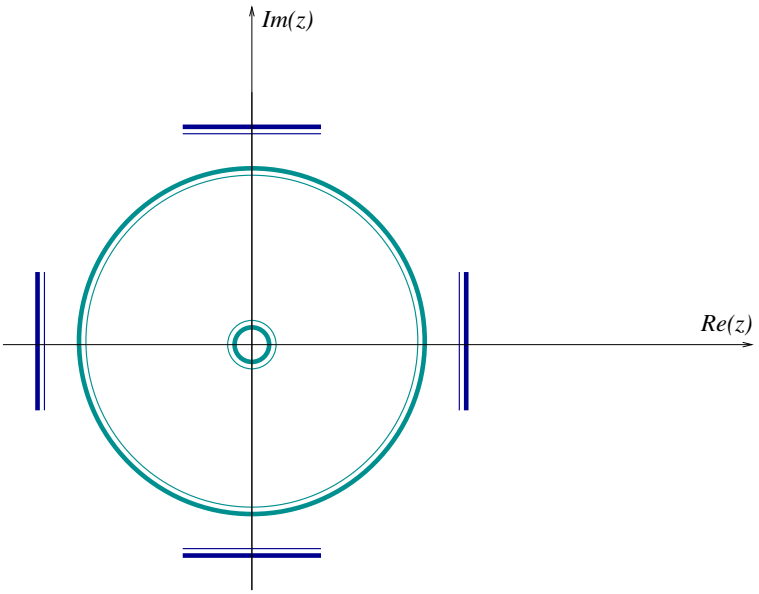

Figure 5.1: Schematic picture of the different Arnoldi basic computational modes. The Arnoldi algorithm is organised to compute a fixed number of complex eigenvalues following simple criteria. The choice can be made to compute the eigenvalues with Largest or Smallest Real, Imaginary parts or Magnitude. Overall, the modes are classified through the capital letters **LR**, **LI**, **LM** (for largest real, etc..) or **SR**, **SI**, **SM** (for smallest real, etc..).

5.5.1 Convergence pattern

Although the eigenvalues evaluation is made after orthogonal projection on H_k, the Arnoldi algorithm iteratively extends the Krylov space from an initial vector v_0. In contrast to the power method (convergence rate $|\lambda_2/\lambda_1|$), Lanczos methods converge with rate $|\lambda_2/\lambda_1|^{2(j-1)}$ after j iterations. This comes from the fact that the maxima of $r(x) = x^\dagger Ax/x^\dagger x$ are evaluated along the gradient

of maximal convergence, which is achieved through the underlying construction on a Krylov spaces $\mathcal{K}_j(A, v_0)$.

The largest eigenvalues converge first and the algorithm progression is faster where the eigenvalue density is low[3].

5.5.2 Organisation of the Arnoldi algorithm

The Arnoldi algorithm of [32] presents itself as a set of routines and the communication with the matrix multiplication has to be organised. Thus, the computation time is distributed between the operation of the ARPACK routines and the matrix multiplications.

5.5.3 Approximated eigenvectors

After convergence, the partial Schur form of H_m is computed $H_m Q_k = Q_k R_k$, with R_k upper triangular. The wanted Ritz value are in the diagonal of R_k. The Schur eigenvectors are then given forming $V_m Q_k$ [4].

[3]For a picture, see the *Arnoldi lenses* in [23], where the domain of converged eigenvalues first enclose the eigenspectrum before it "flows" into it, where the eigenvalue density is the lowest. See also tests with the operator D_W in Fig.(6.4) and Fig.(6.7).

[4]see ARPACK documentation for alternative implementations

Chapter 6

Computation of the real Wilson-Dirac operator eigenvalues

For already mentioned reasons, an efficient computation of the lowest real eigenvalues can become a critical issue, in term of computational velocity, memory as well as precision.

At first sight, given the eigenvalue distribution and the Arnoldi computational modes, one may consider the application of simple computational strategies, as described in Fig.(6.1). As one is primarily interested in the real eigenvalues, this approach turns out to be inefficient.

For this reason, alternative computational strategies are presented in section 6.2. They are based on the idea of explicit restarting or acceleration, which is achieved trough polynomial transformations of the eigenspectrum.

6.1 The behaviour of the Arnoldi algorithm for the Wilson-Dirac eigenproblem

After the Arnoldi algorithm mathematical aspects were reviewed, an empiric study of the algorithm real performances and behaviour for the Wilson-Dirac operator eigenproblem is required.

6.1.1 Performances of the Arnoldi algorithm

This study was done for the one flavour QCD model considering two sets of 100 stout-smeared configurations $\beta = 4.0$, $\kappa = 0.1460$, with lattice sizes $8^3 \times 16$ and $12^3 \times 16$. Those configurations have small eigenvalues and their determinant is likely to be negative.

Computation mode: LR or SM One refers to the summary of Fig(5.1) for the Arnoldi computational modes. Fig(6.1) illustrates possible practical applications on the real eigenspectra. For the computation of Wilson-Dirac

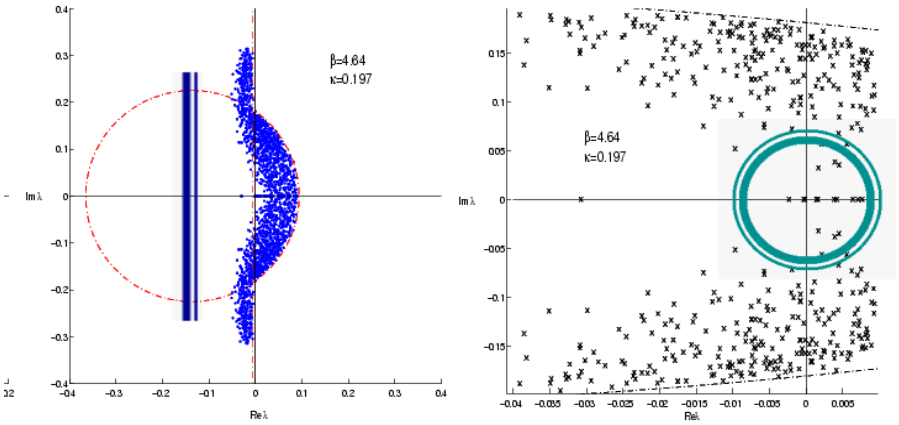

Figure 6.1: For the $N_f = 2$ QCD model with low, degenerated quarks, 100 exceptional (low eigenspectrum is very low) configurations 8^3x16 were studied in [56]. Their eigenspectra are represented, with a blow up on the right. The circle and the line represent two basic Wilson-Dirac operator eigenvalues computational strategies with Arnoldi. The application of the SR computational mode is sketched on the left picture. The right picture illustrates an alternative application of the SM mode. Such strategies turn out to be inefficient.

operator eigenvalues, a standard choice consists in choosing the LR mode on a transformed Dirac operator

$$D_W \rightarrow -D_W + \sigma \mathbf{1},$$

where the minus sign ensures that the lowest eigenvalues of D_W are extracted first with the LR mode of the Arnoldi algorithm (because of the eigenspectrum symmetries, this is an irrelevant detail):

- Because the computational SM mode convergence is slower in practice.
- With the SM mode, determinant sign computations are forced to include the whole set of complex eigenvalues settling around zero (this can be seen on Fig(6.1), where hundreds of eigenvalues would have to be computed before the smallest real eigenvalue is reached).
- The LR mode is suited to the acceleration techniques presented in the section 6.2.

Precision and convergence as a function of the Ritz value As seen in section 5.3.1, the Ritz value evaluates the numerical precision reached by the Arnoldi algorithm. Decreasing the required Ritz values increases the computational precision. From the eigenvalues extracted by the Arnoldi algorithm factorisation, eigenpairs $\{\lambda, v_\lambda\}$ can be constructed, where v_λ is a right eigenvector of D_W. The *numerical eigenvalue* $\lambda_{num.}$ is constructed as

$$\lambda_{num.} \equiv \frac{1}{N} \sum_i^N \frac{(D_W v_\lambda)_i}{(v_\lambda)_i},$$

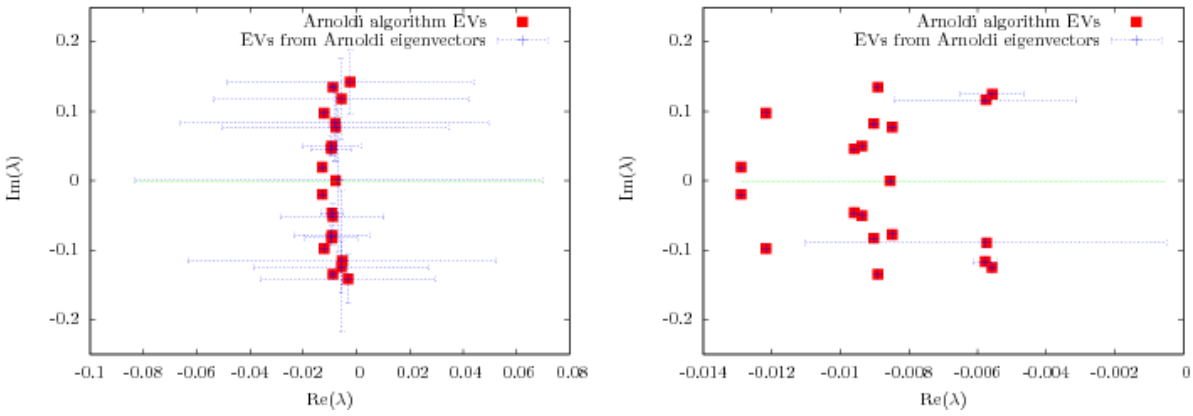

Figure 6.2: For the one flavour QCD model and a lattice $8^3 \times 16$, a configuration generated with $\beta = 4.0$, $\kappa = 0.146$ is considered. 20 Eigenvalues were extracted with required Ritz estimates set at 0.01 on the left and 0.005 on the right. As in eq.(6.1), the errors were constructed from the standard deviation $\sigma_{num.}$. The eigenvalues were computed with the LR mode on the transformed operator $-D_W + \mathbf{1}$. The eigenvalues of D_W are retrieven from the eigenvectors.

with N the eigenproblem dimension.

- A numerical standard deviation can be constructed comparing the values $\frac{(D_W v_\lambda)_i}{(v_\lambda)_i}$ and $\lambda_{num.}$ as

$$\sigma_{num.} = \sqrt{\frac{1}{N}\sum_i^N \left(\frac{(Dv_\lambda)_i}{(v_\lambda)_i} - \lambda_{num.}\right)^2} \tag{6.1}$$

- Recall that the eigenvalue spectrum exhibits horizontal and vertical symmetries.

These properties allow for a practical evaluation of the eigenvalues extraction quality. Fig(6.2) shows that the computational precision gradually improves with increasing Ritz estimates. In addition to this, $\sigma_{num.}$ furnishes a convincing upper boundary for the numerical precision of eigenvalues computations.

As expected (discussion in section 5.3.2), the leftmost eigenvalues of D_W converge much faster as shown in Fig(6.2).

Convergence speed vs the computed eigenvalue number and the lattice size Fig.(6.3) shows the following aspects of the Arnoldi algorithm behaviour:

- On the lattices considered ($8^3 \times 16$ and $12^3 \times 16$), for different Ritz values, the number of iterations realised before convergence is almost identical. For the matrix multiplication, more operations (factor $\approx \left(\frac{12}{8}\right)^3$)) are involved for larger lattices. The number of iterations increases linearly with the number of computed eigenvalues.

- The computation time increases approximately exponentially with the number of computed eigenvalues.

As more eigenvalues have to be treated, one concludes with [38] that more operations are involved inside of the Arnoldi routines.

Translation/scaling dependance As for the power method, translations $D_W \to -D_W + \sigma \mathbf{1}$ or scaling σD_W transform the eigenvalue distribution, which in turn affects the Ritz estimates (translations change the convergence behaviour while scalings change the "effective" Ritz estimate).

For $D_W \to -D_W + \sigma \mathbf{1}$, the convergence velocity increases with larger σ's. However, as seen in Fig.(6.4) and Fig.(6.5), the computed eigenspectrum gets distorted. If more precision is imposed, the σ-shift dependance is almost cured (Fig.(6.6)).

Algorithm stability As discussed in the last section, for computations with the LR mode, the Arnoldi algorithm converges first for the outer eigenvalues, before more inner ones get extracted. The algorithm progression depends on the eigenvalue density.

Since the eigenvalues reordering takes place at finite precision, this convergence scheme influence the eigenvalue selection. The eigenvalues extracted are only approximately the largest (see Fig.(6.4) and Fig.(6.5)). This issue is critical, since the most relevant information is contained in the inner eigenspectrum.

Therefore, it was important to test in practice whether there is a subdomain of computed eigenvalues where the LR criterion is consistently realised (all the largest, real eigenvalues are extracted within a certain range). The question of computational convergence and consistency is discussed variating the σ-shifts, the precision and the number of computed eigenvalues in Fig.(6.6) and Fig.(6.7) (different shifts were chosen in order to force different convergence "histories").

Fig.(6.6) shows that different computations strategies lead to similar extractions. Fig.(6.7) illustrates typical convergence patterns and that the eigenspectrum is consistently reproduced for a subdomain of computed eigenvalues.

Caution It is impossible to know exactly wether the Arnoldi algorithm misses inner eigenvalues. Fig.(6.7) shows that this is an issue.

Because of D_W non-normality, degenerated or almost degenerated eigenvalues are likely to be not detected. This issue is particularly severe for the $\mathcal{N} = 1$ Sym case, as shown in appendix C.

6.1.2 Arnoldi Algorithm behaviour and performances, practical wisdom:

The following list summarises relevant issues around the eigenvalues computation. The Arnoldi LR mode is chosen for the problem of computing the real eigenvalues of D_W.

- With the LR criterion, the Arnoldi algorithm computes first and with precision of higher order the largest eigenvalues. They converge faster and are extracted with a precision of higher order.

- The Arnoldi algorithm performances depend on the eigenvalues separation. The most isolated eigenvalues converge much faster and are more precisely extracted.
- The computation time increases approximately exponentially with the number of computed eigenvalues. This comes mostly from the Arnoldi routines.
- Scalings and translations of the eigenspectrum highly affect the Arnoldi algorithm behaviour and its performance. In practice, the eigenvalues were extracted around 1.
- With the LR mode criterion, the algorithm computes eigenvalues from the right to the left of the complex plane. However, in practice and independently of the computational precision, this scheme is only approximately realised.

  For an eigenspectrum extracted with sufficient precision (in respect to $\sigma_{num.}$ and the eigenspectrum symmetries), the LR mode is exactly realised inside of the spectral window formed by the largest third of the extracted eigenvalues. This issue depends on the eigenvalues distribution and density.
- Degeneracy is hidden in practical computations. For non-normal lattices, doubler eigenmodes appear only as a very high precision is reached.

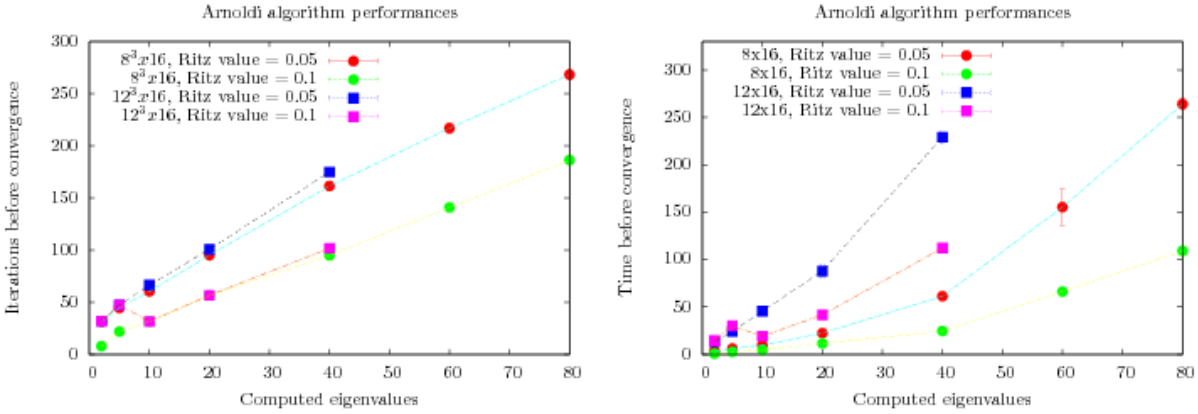

Figure 6.3: The eigenspectrum of $(-D_W+\sigma\mathbf{1})$ is computed with the Arnoldi LR mode. The computation time as well as the iterations required before convergence are studied in relation with the Ritz value and the number of computed eigenvalues. The increase is linear for the iterations number and nearby exponential for the computation time. This difference is caused by the Arnoldi algorithm routines.

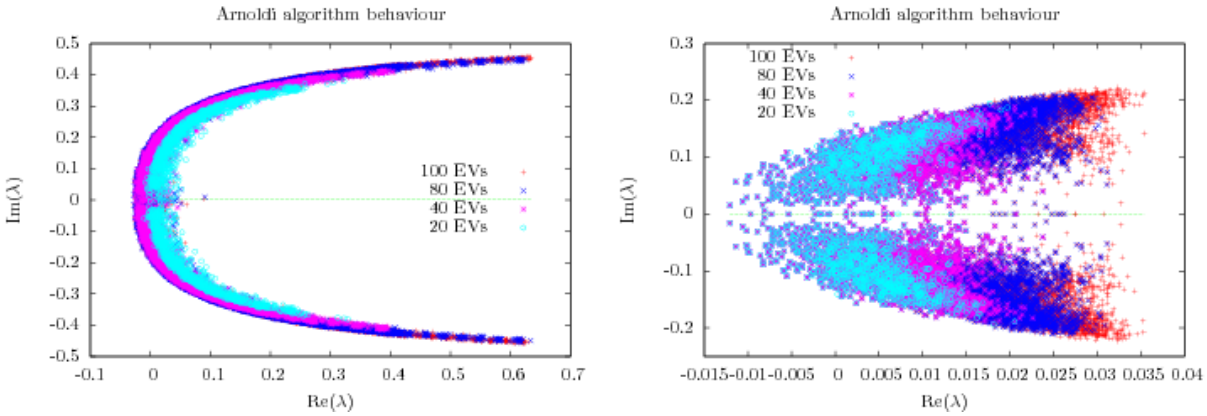

Figure 6.4: Eigenvalue computations with the Arnoldi algorithm on a set of 100 configurations ($N_f = 1$ QCD, $\beta = 4.0$, $\kappa = 0.1460$, $8^3 \times 16$). Computations are compared for two different Ritz criteria: 0.05 on the left and 0.00001 on the right. The number of eigenvalues collected with the Arnoldi LR mode on the operator $(-D_W + \sigma\mathbf{1})$, $\sigma = 5.0$ was varied from 20 to 100. Eigenvalues of the initial operator D_W were reconstructed from the eigenvectors. Independently of the precision, the LR mode is only approximately realised while the external eigenvalues converge faster and are extracted first. The figures illustrate typical Arnoldi extraction patterns in function of the precision.

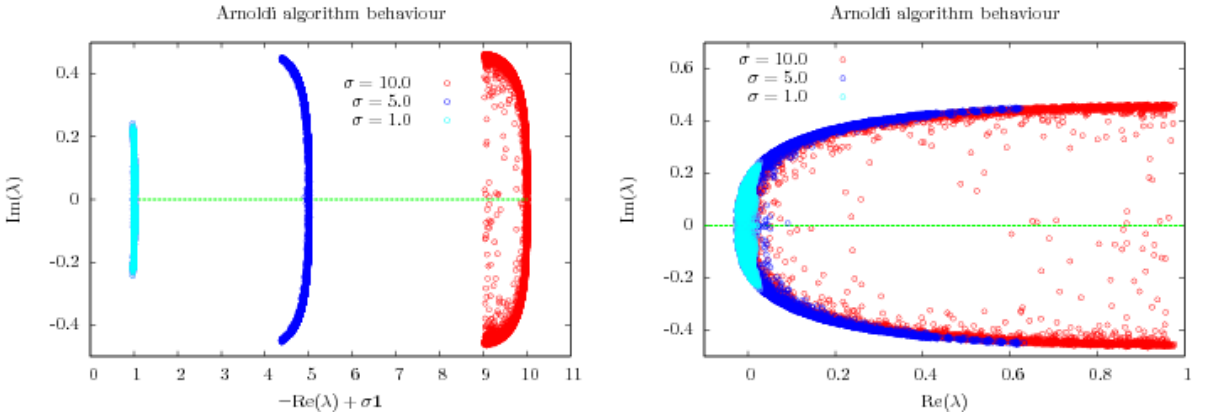

Figure 6.5: For the eigenspectrum of $(-D_W + \sigma\mathbf{1})$ and 5 fields configurations ($N_f = 1$ QCD, $\beta = 4.0$, $\kappa = 0.1460$, $8^3 \times 16$), the computation time and the extraction quality depend on σ. On the left, the shifts $\sigma \in \{1.0, 4.0, 10.0\}$ were applied for eigenvalue computations and the eigenvalues are plotted as they were found with the Arnoldi LR mode, with Ritz criterion 0.01. One finds a factor 10 between the computation times of the fastest ($\sigma = 10.0$) and the slowest ($\sigma = 1.0$) computations. On the other hand, as the eigenspectra of D_W are reconstructed and compared on the right figure, the computations with larger σ show more deviation in the extraction patterns and the LR mode is less realised in practical computations (the inner eigenvalues are skipped while the outer eigenspectrum is computed).

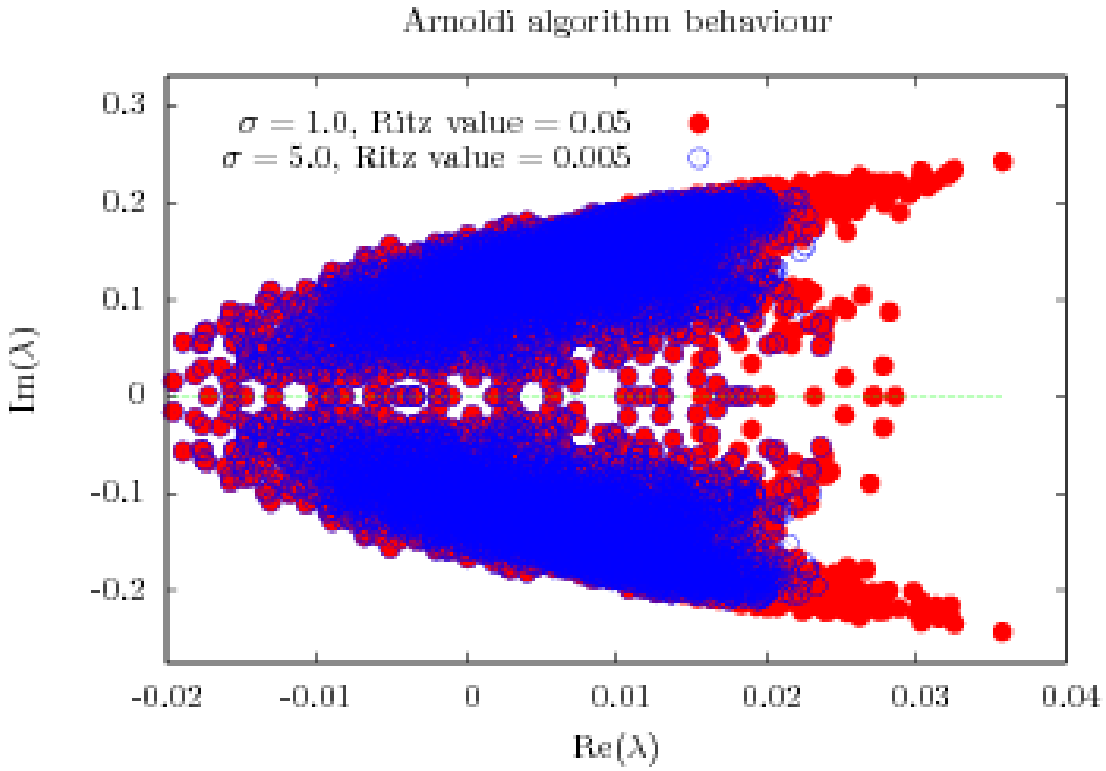

Figure 6.6: In order to test the computational consistency, two computations are compared. For 100 configurations ($N_f = 1$ QCD, $\beta = 4.0$, $\kappa = 0.1460$, $8^3 \times 16$), the 80 largest eigenvalues were computed with the LR mode after the transformation $(-D_W + \sigma \mathbf{1})$ with $\sigma = 1.0$ (Ritz coefficient 0.0005) and $\sigma = 5.0$ (Ritz coefficient 0.00005). The resulting eigenvalues found for D_W were plotted. Both eigenspectra appear to match exactly for the eigenvalues close to zero while more distant eigenvalues show different extraction patterns.

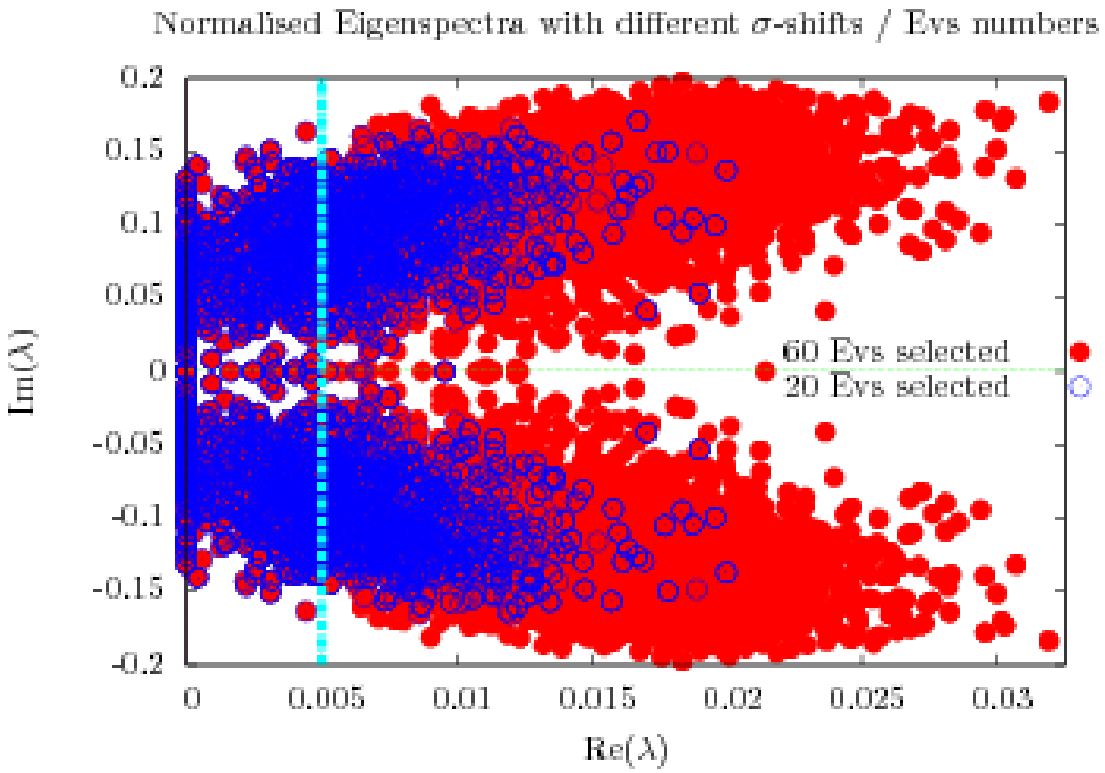

Figure 6.7: Does the LR computational mode compute consistenly the largest real eigenvalues in practice? The LR mode was used for the extraction of eigenvalues of $(-D_W + \sigma\mathbf{1})$. The computations were performed with Ritz criterion 0.00001, different σ-shifts ($\sigma = 1.0$, $\sigma = 5.0$) and 20 or 60 computed eigenvalues. For more visibility, the lowest extremities of the eigenspectra of D_W were all set to 0. This experience puts in evidence that the LR criterion is precisely realised only for the most outer $\sim 1/2 - 1/3$ of the computed set. The approximative cut-off is represented by the turquoise line.

6.2 Polynomial transformations on the Wilson-Dirac operator

As shown in the last section, the Arnoldi algorithm behaviour strongly depends on the number of eigenvalues to be extracted, as well as their distribution and density. For that reason, a standard technique consists in computing eigenvalues on a transformed version of the initial eigenspectrum. Transformations enhancing the algorithm performances are known as *polynomial acceleration* or *restarting* strategies. Notice that *Implicit restarting* is already implemented during Arnoldi algorithm iterations (Chebyshev polynomials realised with the QR algorithm, ...) and follows similar ideas as the ones exposed below.

6.2.1 Polynomial acceleration

Polynomial acceleration (or *Explicit* restarting), in this context, consists in transforming the initial spectrum into another one, on which the Arnoldi algorithm acts more efficiently. A simple strategy is to deform the eigenspectrum such that the domain of wanted eigenvalues gets expanded while the domain of unwanted ones is contracted.

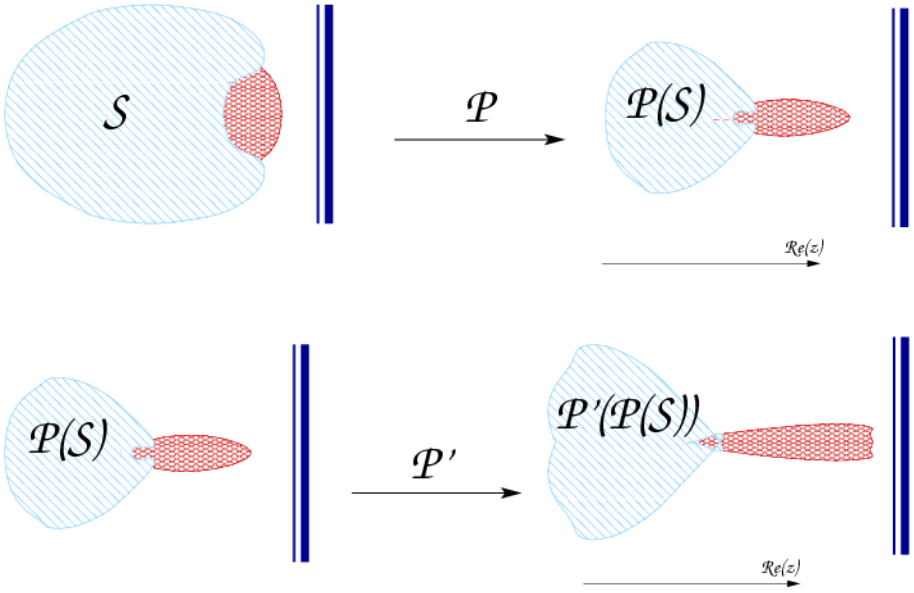

Figure 6.8: Idea of explicit restarting. The spectrum on the left is mapped onto the right, which is better suited for the eigenvalues extraction, with the LR mode, of a particular eigenvalue domain. In this example, the set of wanted eigenvalues is represented by the red area. As shown on the lower figures, the polynomial transformation can be iterated.

In order to achieve this, the possible operations on the matrix multiplication are polynomial transformations, shifts and matrix inversions. Since they are expensive in term of computation time (in particular with small eigenvalues), matrix inversions were not considered here.

In the next sections, transformations are presented which apply the preconditioning idea focusing on the extraction of the lowest, real eigenvalues of the Wilson-Dirac operator.

The power and the "peeling" polynomial transformation techniques are based on the simple observation that only complex eigenvalues rotate under the $z \to z^n$ transformation. A further idea, introducing Faber polynomials, is an alternative procedure.

The question of optimality

Because the methods presented are based on arbitrary choices, the question of *optimality* for the computational strategy is difficult to address.

Eigenvalue recovery

After some polynomial transformation $D_W \to P(D_W)$, the initial eigenvalue spectrum can be retrieved applying the inverse transformation $P(D_W) \to D_W$ (in the domain where the transformation is bijective).

Alternatively, since the Arnoldi algorithm computations evaluate the eigenvectors of the modified eigenspectrum $P(D_W)$, they can be used to reconstitute the initial eigenspectrum (recall that $D_W v_\lambda = \lambda v_\lambda \iff P(D_W)v_\lambda = P(\lambda)v_\lambda$).

6.2.2 Power transformation

For the eigenvalues within the eigenspectrum, one considers the notation $z = \rho e^{i\theta}$, $z \in \mathrm{C}$. Obviously, real eigenvalues have vanishing θ angles. Another basic observation is that complex eigenvalues rotate under a power transformation as $z \to z^n$, $z^n = \rho^n e^{in\theta}$.

Power transformation

For $-D_W + \sigma\mathbf{1}$, the transformed Wilson-Dirac operator, the power transformation is simply

$$P_{\sigma,\,n}(D_W) = (-D_W + \sigma\mathbf{1})^n.$$

This transformation can be designed to have the following effects (see Fig.(6.9)):

- It lowers the eigenvalue density on the right part of the transformed eigenspectrum.
- The complex eigenvalues are partially rotated outside of the window where Arnoldi computes the eigenvalues (with the LR mode). As a result, less eigenvalues have to be considered.

Trigonometric considerations This pictorial description may be completed in the following manner: consider the transformation presented above

$$z \to (z+\sigma)^n \equiv y = \xi e^{i\phi}, \quad \rho < \sigma \leq 2\rho.$$

We are interested in the complex eigenvalues $z = \rho e^{i\theta} \in \mathrm{C}$, with $\theta \approx 0$, such that the following approximations can be derived

$$\rho \to \xi = \left((\cos(\theta)\rho + \sigma)^2 + (\rho\sin(\theta))^2\right)^{n/2} \cong \rho^n \left(1 + \frac{\sigma}{\rho}\right)^n.$$

$$\Longrightarrow \rho^n \lessapprox \xi \lessapprox 2^n \rho^n$$

$$\tan(\phi/n) = \rho\sin(\theta)/(\rho\cos(\theta) + \sigma) = \frac{\frac{1}{2}\sin(2\theta) - \sin(\theta)\sigma/\rho}{\cos^2(\theta) - (\sigma/\rho)^2} \cong \theta\frac{1-\sigma/\rho}{1-(\sigma/\rho)^2}$$

$$\Longrightarrow \tfrac{1}{3}n\theta \lessapprox \phi \lessapprox n\theta$$

- Thus, small angles can be expanded by appropriated power transformations.
- On the other hand, some combinations of $\{\sigma,\, n\}$ with n too large may cause eigenvalue sectors to overlap i.e. eigenvalues rotated outside of the computational window (the rightmost eigenvalues) reappear in it after they performed a complete rotation, leading to ambiguities and cancelling the transformation positive effects.

  This issue is taken under control considering very simple geometrical notions. Let L be the eigenspectrum width and H its height, then the maximum number of authorised rotations n_{max} is approximately given by $n_{max} \approx 2\pi/\arctan(H/(L+\sigma))$.
- Consider σ such that the outer right part of the eigenvalue spectrum lies just above 1. In this case, the eigenvalues on the right of 1 are going to rotate and expand while the remaining eigenvalues are going to rotate and contract.

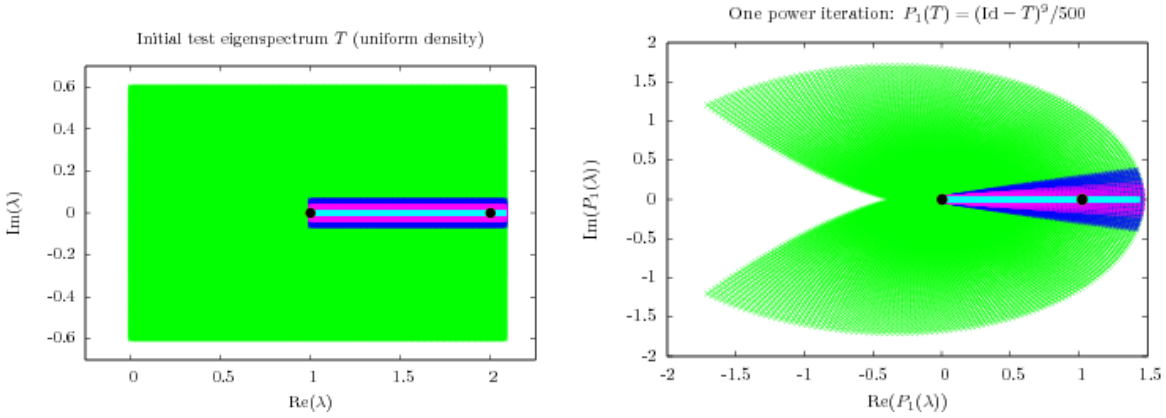

Figure 6.9: On the left, an initial test eigenspectrum with constant eigenvalue density and similar to $-D_W + 2.0 \cdot \mathbf{1}$ is represented. On the right, the test eigenspectrum is represented after one polynomial transformation. The black dots localise the transformed zero and the eigenspectrum centre. After such a transformation, the eigenvalues are extracted from the right with the Arnoldi algorithm (LR mode).

Technical issue

Those basic ideas allow for appropriate choices of $\{\sigma, n\}$. Obviously, polynomials of higher order will lower the spectrum density and rotate the eigenvalues better. However, the polynomial order also fixes the number of matrix multiplication operations. The balance between polynomial order and algorithmic speed is discussed in [38].

6.2.3 Faber polynomial transformation

As an alternative to the power method, the problem of finding the best polynomials can be addressed making use of more elaborated mathematical tools. To sketch the idea, [20] proposes to enclose the unwanted eigenvalues within an ellipsoidal or polygonal hull $\mathcal{E}$, as in Fig.(6.10). Then, the construction of polynomial transformations separating both regions can be addressed analytically as a minmax problem:
For a given $k \in \mathrm{N}$, one considers $\mathcal{P}_k$, the set of polynomial of order $< k$. A polynomial $p_k \in \mathcal{P}_k$, normalised as $p_k(\lambda) \leq 1$, $\forall \lambda \in \mathcal{E}$ and achieving the minimum

$$\min_{\{\mathrm{p_k} \in \mathcal{P}_\mathrm{k} |\, \mathrm{p_k}(\lambda_1)=1\}} \max_{\{\lambda \in \mathcal{E}\}} \|\mathrm{p_k}(\lambda)\|_2$$

is sought. For a polygonal hull, such a polynomial can be analytically constructed using Chebyshev bases and p_k is a Chebyshev polynomial [20].

As an alternative strategy, [33] shows that, for polygonal hulls, Faber polynomial can be considered, as shown in Appendix A. They achieve the polynomial transformation sketched in Fig.(6.11). First, the Faber polynomials should show better performances. Second, they can be generated by an existing, matlab based software [31].

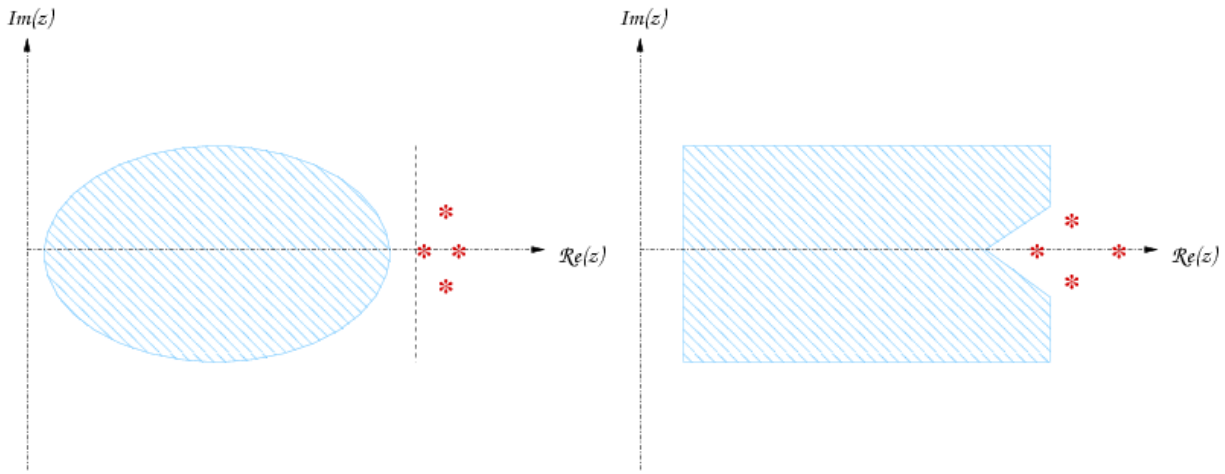

Figure 6.10: Illustrations of ellipsoidal and polygonal hulls separating wanted and unwanted eigenvalues. The unwanted eigenvalues are within the magenta shape. The magenta dots on the right represents some wanted eigenvalues.

This approach has the advantage to be analytical, the coefficients being mathematically set. Nonetheless, the strategy arbitrariness remains and is traded off against choices of polygonal shape and polynomial orders.

Transformation behaviour

Using the software proposed by [31]. The Faber polygons can be constructed in the complex plane. Polygonal shapes are tested in Fig.(6.12) and Fig.(6.13), where the enclosing polygonal hulls considered as well as the resulting transformed eigenspectrum are plotted.

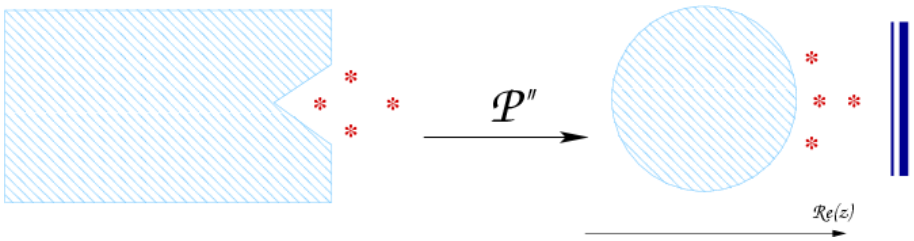

Figure 6.11: Faber polynomial transformation idea. According to a polygonal hull separating the wanted/unwanted eigensectors, a Faber polynomial transformation projects the wanted eigenvalues onto the right, outside of circle where unwanted eigenvalues get enclosed. After the Faber transformation, the wanted eigenvalues are collected with the Arnoldi algorithm in LR mode (blue bars).

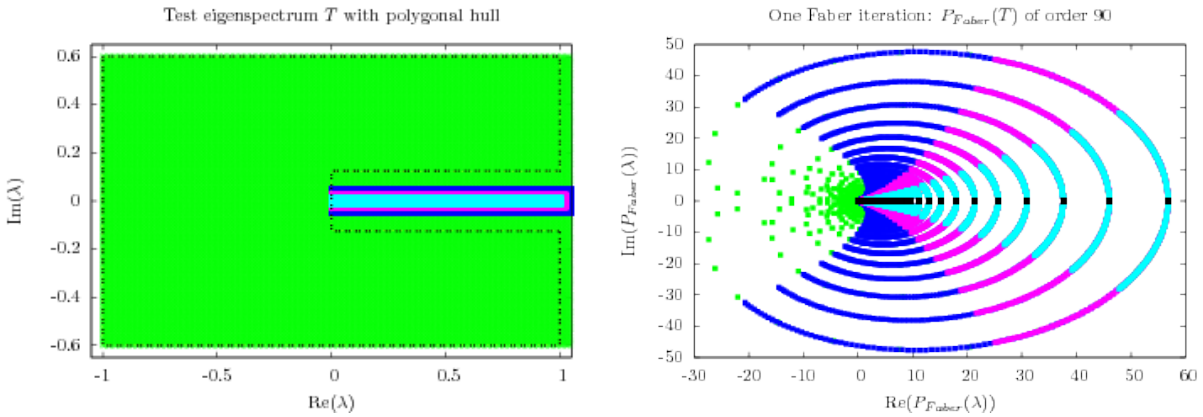

Figure 6.12: The Faber transformation is tested on a pseudo-eigenspectrum with constant density. The resulting test eigenspectrum and the polygonal hull are presented on the left. The corresponding transformed eigenspectrum is shown on the right.

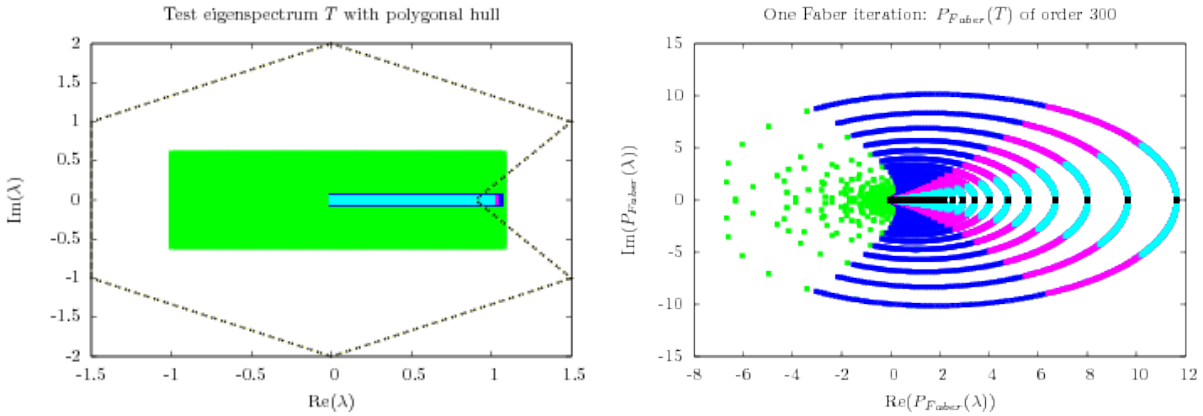

Figure 6.13: The Faber transformation is tested on a pseudo-eigenspectrum with constant density. The test eigenspectrum and the polygonal hull are presented on the left. The corresponding transformed eigenspectrum is shown on the right.

6.2.4 The "peeling" method

The *peeling method* consists in applying the power method iteratively onto D_W's eigenspectrum, until the real eigenvalues are sufficiently expanded and isolated.

Because of the overlapping problem mentioned above, a power method transformation cannot rotate all of the complex eigenvalues away (as they reenter the spectrum after $2\pi n\,(n \in \mathrm{N})$ rotations). Nevertheless, in theory, this can be achieved by iterations of the power method transformation.

"Peeling" procedure

1. apply the power transformation $P_{\sigma,\,n}(D_W) = (D_W + \sigma\mathbf{1})^n/R$ according to the initial eigenspectrum $\mathcal{S}$. R normalises the polynomial.

2. according to the new eigenspectrum $\tilde{\mathcal{S}} \equiv P_{\sigma,\,n}(\mathcal{S})$ boundaries, design a new polynomial $P_{\tilde{\sigma},\,\tilde{n}} = (D_W + \tilde{\sigma}\mathbf{1})^{\tilde{n}}/\tilde{R}$. This way, a new eigenspectrum $\tilde{\tilde{\mathcal{S}}} \equiv P_{\tilde{\sigma},\,\tilde{n}}(P_{\sigma,\,n}(\mathcal{S}))$ is obtained.

3. ... iterate further ...

The ideas are the following: 1. rotates the complex eigenvalues with a first power transformation. 2. rotates the eigenvalues with largest real part anew. Depending on the shift, the transformed complex eigenvalues that were rotated to the left side of the eigenspectrum are heavily contracted on the left of the transformed zero, while eigenvalues with larger real part are expanded. As a result, complex eigenvalues are purged in the sense that they will not reappear in Arnoldi computations with LR mode. This is illustrated in Fig.(6.9), Fig.(6.14) and Fig.(6.15).

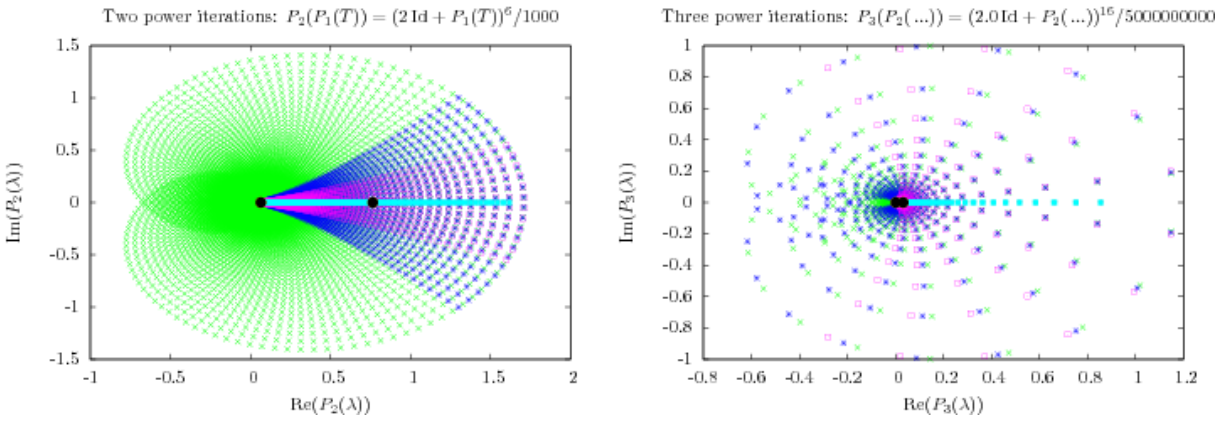

Figure 6.14: After successive iterations, the number of complex eigenvalues on the right of the zero was reduced to the elements inside of the magenta area (see Fig.(6.9)). Successive normalisations are applied for numerical reasons, while the shifts $\{\sigma_1, \ldots, \sigma_n\}$, orders $\{n_1, \ldots, n_n\}$ and normalisations $\{R_1, \ldots, R_n\}$ are chosen such that the rotated eigenvalues do not reenter the transformed eigenspectrum on the right of the transformed zero.

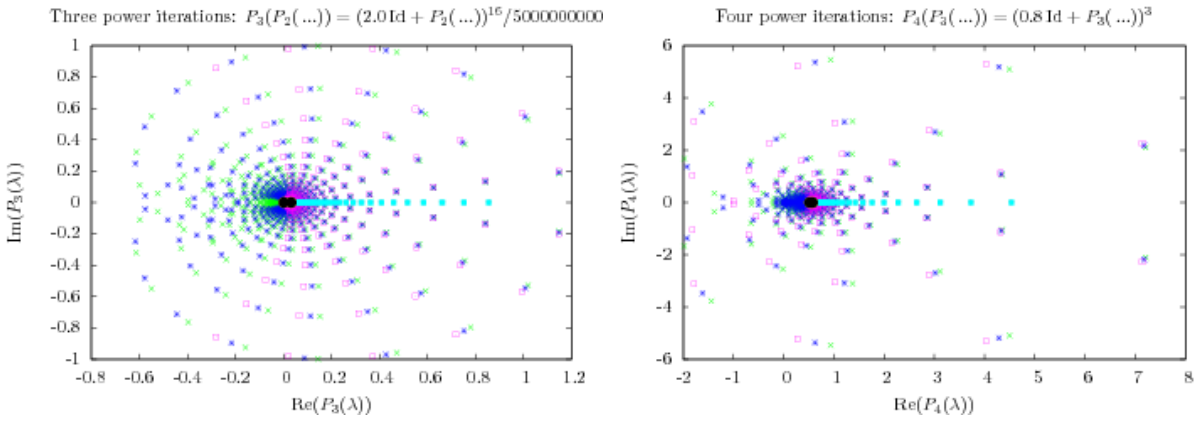

Figure 6.15: Outer eigenvalues get peeled away. They get contracted onto the transformed zero from the left. More inner eigenvalues get compressed onto the zero from the right. On the right, eigenvalues outside the magenta area (see Fig.(6.9)) can be considered to have been successfully peeled away.

"Peeling method" and two practical approaches

In theory, a complete or quasi-complete extraction of the inner eigenspectrum is possible. This is first shown through a simple and pedestrian approach, which is made more practicable in a second step.

"Pedestrian Peeling"

1. Depending on an initial eigenvalue spectrum $\mathcal{S}$, one carefully designs a polynomial $z \to P_{\sigma,N}(z)$ rotating the complex eigenvalues with largest imaginary part onto the left of the transformed zero $P_{\sigma,N}(0)$.
   The parameters $\{\sigma, N, R\}$ are chosen avoiding eigensector overlapping on the right of the transformed zero.

2. For the new transformed eigenspectrum $P_{\sigma,N}(\mathcal{S})$, the outer eigenspectrum borders are evaluated with the LR, SR, LI and SI criteria (this can be done with the computation of a few extremal eigenvalues).

3. restart in 1. with $\mathcal{S} \Leftarrow P_{\sigma,N}(\mathcal{S})$

The strategy is illustrated in Fig.(6.16) and Fig.(6.17). Careful choices of polynomial transformations, designed using simple geometrical computations, would allow for an iterative (albeit long) purging of all complex eigenvalues.

However, this method, although simple enough to be automatised, is very unpractical. Indeed, a polynomial has to be successively constructed with iteration orders similar to the number of complex eigenvalues to be peeled away.

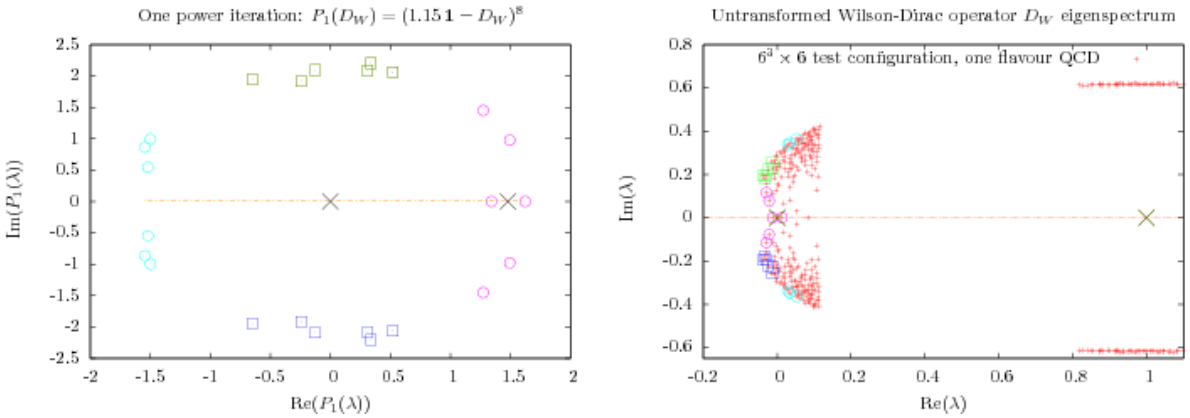

Figure 6.16: On the left, the outer eigenvalues of $P_8(D_W) = (1.15 \cdot \mathbf{1} - D_W)^8$ are shown as they were extracted by the Arnoldi algorithm with LR, SR, LI and SI criteria. On the right, the red points show the initial eigenspectrum D_W. From the eigenvectors of $P_8(D_W)$, the eigenvalues found are plotted onto the initial eigenspectrum D_W (with their respective colours and point types).

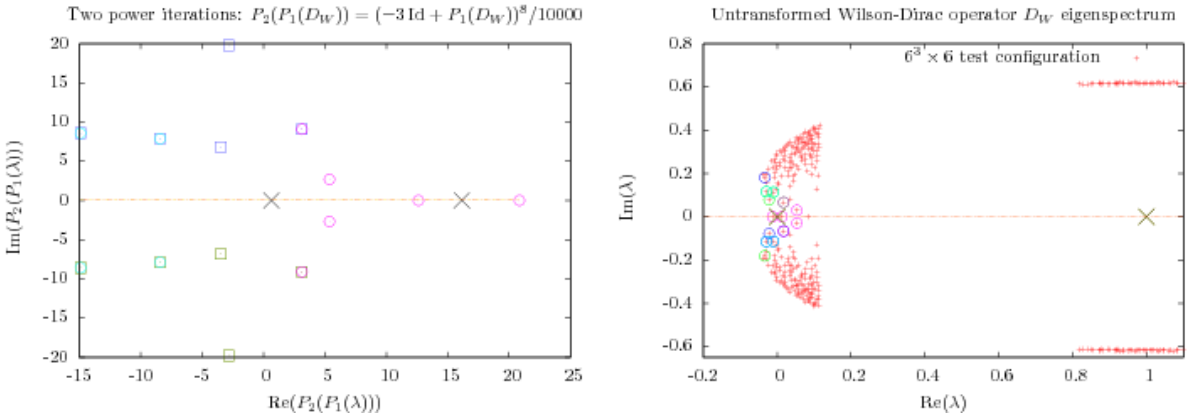

Figure 6.17: Starting from Fig.(6.16), an additional iteration was implemented before the eigenvalues were extracted with the LR, SR, LI and SI modes. The left figure shows the new eigenspectrum boundaries for $\tilde{P}_8(P_8(D_W))$, while D_W is partially reconstructed on the right figure. The additional iteration allows for a deeper extraction of the real eigenvalues. The right figure also shows that the eigenvalue extraction of Fig.(6.16) do partially not reenter the computations.

"Peeling piecewise"

Depending on the configurations to be studied, it is useful to design general "peeling polynomials".

In order to do this, eigenvalues sectors are considered instead of isolated eigenvalues. Basically, one proceeds as in the pedestrian case, but the "peeling strategy" is designed on a test eigenspectrum. They are basically two cases to be considered:

External eigenvalues These are the eigenvalues on the left of the D_W eigenspectrum and close to zero. After the transformation $-D_W + 2 \cdot \mathbf{1}$, these eigenvalues become the mostright ones. They are not dramatically contracted by the successive iterations of the power method. As a result, the external sector can be peeled to the left of zero within a finite number of iterations. This is shown on Fig.(6.14) and Fig.(6.16) and in the following discussion.

Each time that the eigenvalues are sufficiently rotated i.e. $\theta \in [-2/3\pi,\, 2/3\pi]$ ($z = \rho e^{i\theta} \in \mathrm{C}$), the next σ-shift can be chosen such that they get iteratively "compressed" against the transformed zero" by the next iteration. The sector is considered to be cut out and one proceeds further to a more inner one.

Internal eigenvalues The eigenvalues of D_W more inside of the eigenspectrum get contracted under the combined action of power transformations, shifts and normalisations. The successive iterations have for effect to contract these eigenvalues against the real axis and the transformed zero (see Fig.(6.15)). As a result, they are not peeled while the inner eigenspectrum density increases. The extraction strategy completely looses its efficiency.

However, within a finite iteration number, an eigenvalue sector can be considered to have been peeled away. In Fig.(6.14), the eigenvalues outside the blue radius can be considered to have been eliminated as this particular sector does not reenter the Arnoldi computations. Similarly, in Fig.(6.15), the region outside the magenta band was successfully peeled away.

As a sector is cut off, the peeling strategy can be extended to more inner sectors, just ensuring carefully that sectors already peeled do not reenter the eigenspectrum. This iterative procedure is illustrated in Fig.(6.18) and Fig.(6.19).

Technical issues and "peeling method" in practice

Transformations shift and polynomial order: The polynomial transformations efficiency is eigenproblem dependant (lattice size, κ, theory, eigenvalue extraction depth, ...) and, in practice, numerous tests are necessary.

Total polynomial order: Recall first that the order of "peeling polynomial" $P_{tot.} = P_2(P_1(\ldots))$ is multiplicative: $\mathrm{order}_{tot} = \mathrm{order}_1 \cdot \mathrm{order}_2$ and corresponds to the number of matrix operations to be executed. This represents an additional constraint to be dealt with.
For that reason, complicated peeling strategies can become seriously limited in practice.

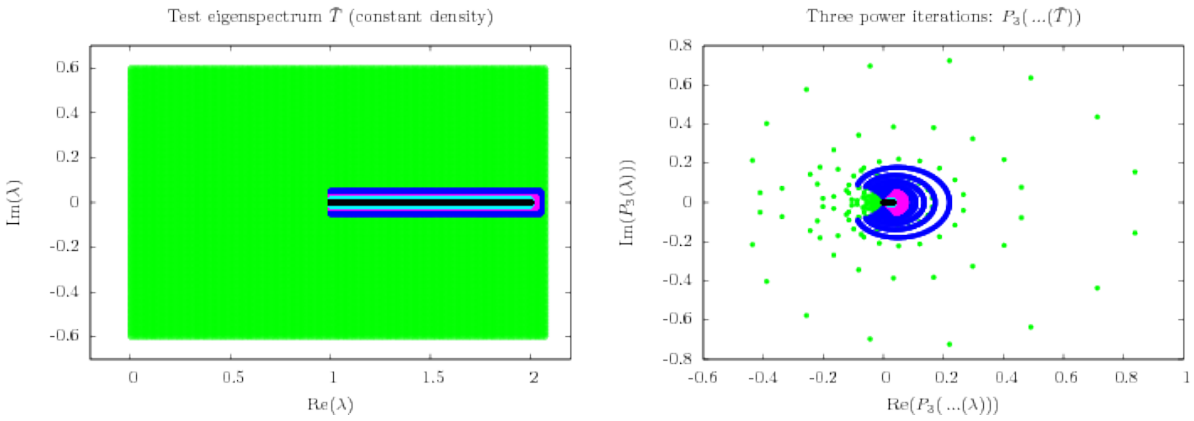

Figure 6.18: On the left, an initial test eigenspectrum with constant eigenvalue density is decomposed into several distinct eigensectors. The right figure shows the test eigenspectrum as it was transformed after 3 successive power transformations.

Additional bottlenecks The axes of Fig.(**??**), on the lower right figure, clearly indicate that numerical issues are likely to appear during the recursive process. Until a certain point, this can be kept under control with appropriate renormalisations.

In practice, the deep, inner eigenspectrum is difficult to extract properly, since it is heavily contracted by the initial transformations adapted to the outer spectrum.

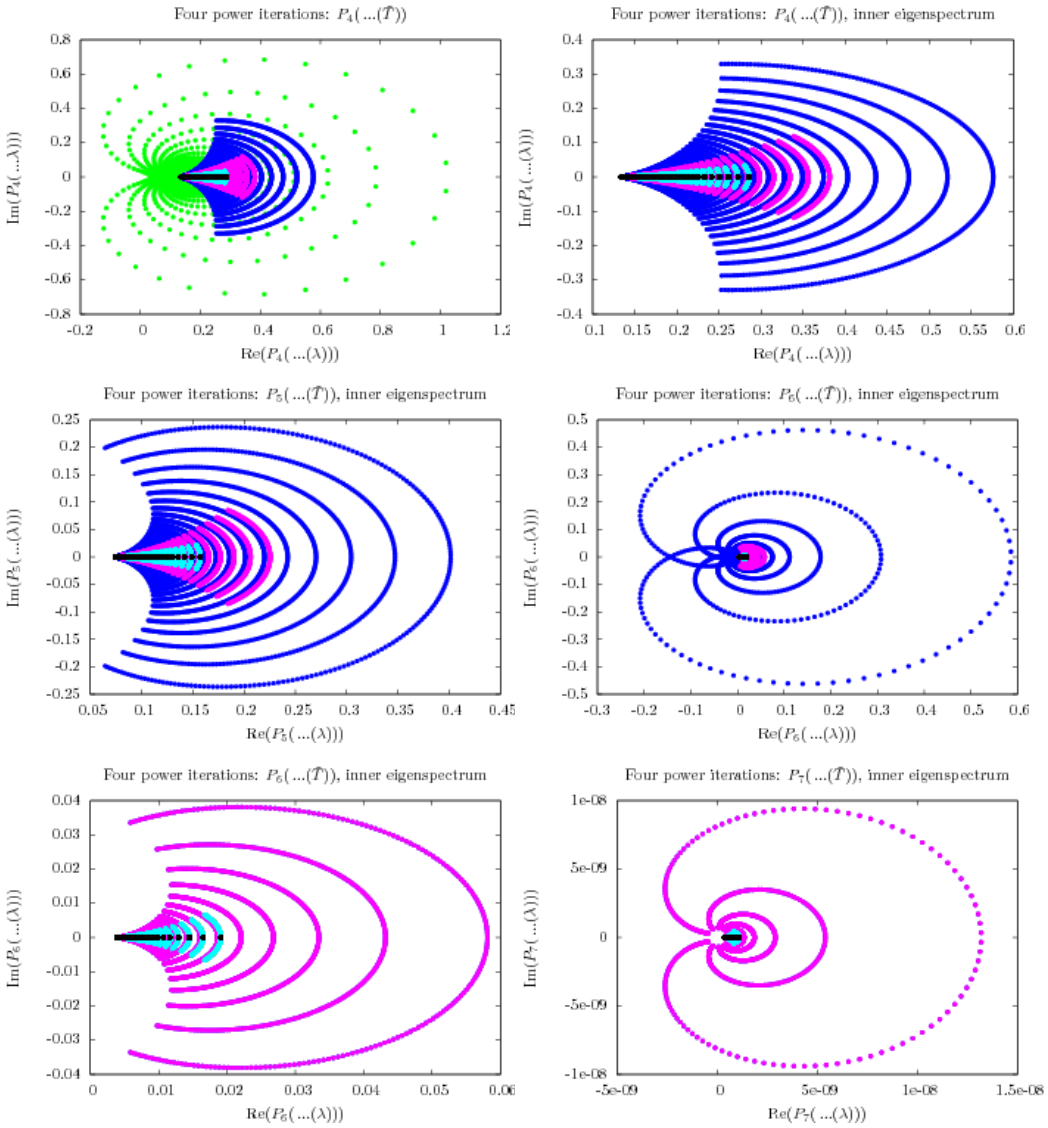

Figure 6.19: As an outer eigenspectrum is cut away, one proceeds iteratively with more inner sectors. The power method is iterated adapting the transformation parameters each time. Efficient peeling strategies can be constructed.

6.2.5 Mixing Faber polynomial and peeling approaches/Peeling with Faber polynomials.

As showed in the last subsections, the peeling method is particularly efficient for the outer sector. Nevertheless, the inner eigenspectrum is heavily compressed, which reduces the method efficiency.

As an alternative, although the Faber polynomial extraction efficiency is inferior on the outer spectrum, the inner eigenspectrum is less contracted under its action. In addition to this, as eigenvalues are rotated onto the eigenspectrum left, they are also effectively contracted onto zero.

This suggests the implementation of polynomial transformations alternating power and Faber iterations, or even peeling strategies based on Faber polynomial transformations. This is adapted on two examples, in Fig.(6.20) and Fig.(6.21).

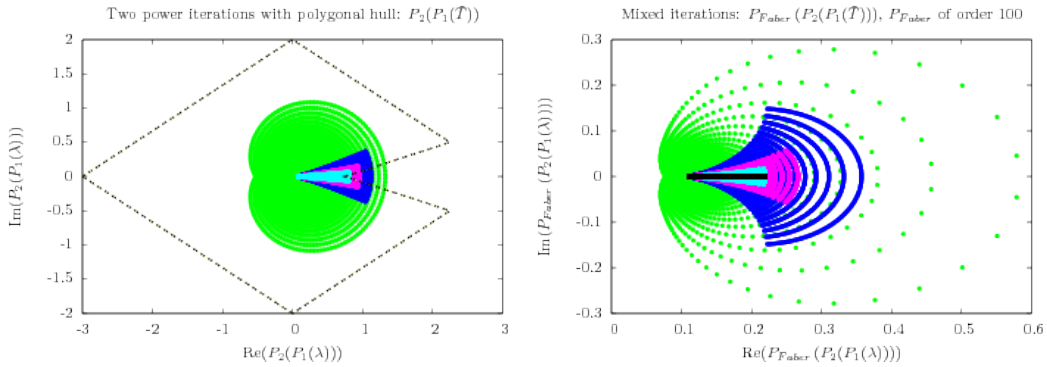

Figure 6.20: The left figure was achieved after two power transformations. According to the Faber polynomial transformation approach, a polygonal hull is sketched. The right figure represents its transformation after Faber transformation.

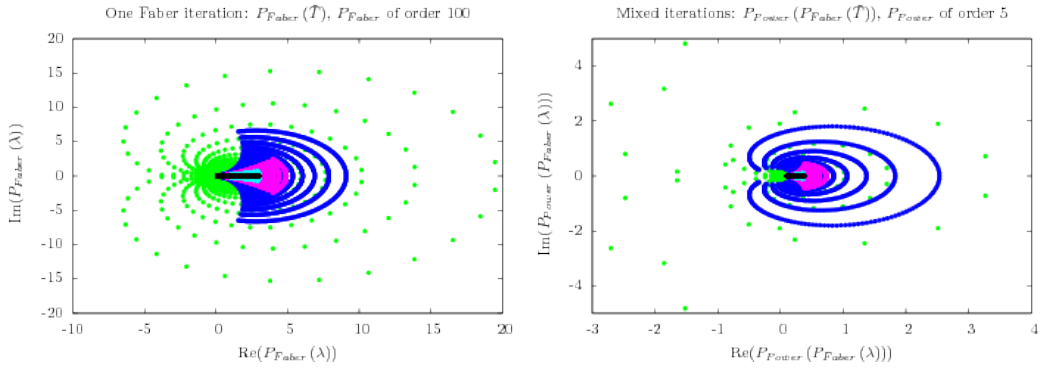

Figure 6.21: The left figure is the test eigenspectrum after Faber transformation. A power transformation is then applied, with as a result the right figure.

6.3 Comparisons, performances, results

The last pictures illustrated quantitatively how the "peeling" and Faber polynomial transformations act on the outer eigenspectrum. However, the polynomial action on the eigenspectrum internal part is less clear.

6.3.1 Spectral windows

In order to study this closer, consider a test eigenspectrum, with constant density. After a polynomial transformation, the eigenvalues are ordered in respect with their real part. Because they are supposedly picked first by the Arnoldi algorithm LR mode computations, the eigenvalues having the largest real part after polynomial transformation are put in evidence in the initial spectrum. A picture emerges, where the different methods can be tested and compared as in Fig.(6.22) – Fig.(6.28). As the spectral windows were extended for broader perspective, a red windows enclose the area where D_W eigenspectrum is expected.

With this method, complicated extraction polynomials can be precisely designed in tuning the transformation parameters. In particular, polynomials can be successively refined until the complex eigenvalues with very low imaginary part and the real ones are extracted only (Fig.(6.24) and Fig.(6.31)).

Eventually, starting from a polynomial transformation and such a spectral windows, the transformed Wilson-Dirac operator $R \cdot (\sigma \mathbf{1} - D_W)$ shifts σ and scaling R may be adjusted for efficienit computations.

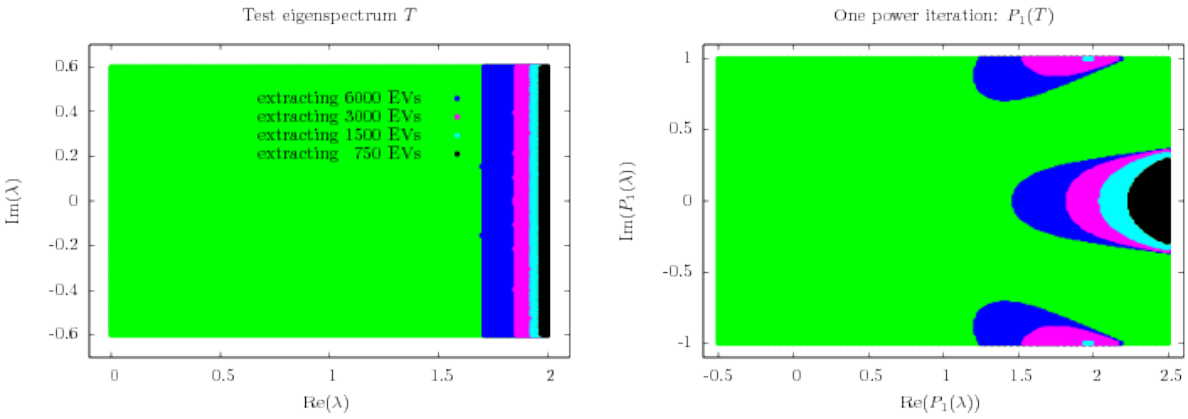

Figure 6.22: After polynomial transformation, computing the 750, 1500, 3000 and 6000 eigenvalues with largest real part on a test eigenspectrum with constant density would extract, with the Arnoldi algorithm LR mode, the black, turquoise, magenta and blue sectors respectively. On the left, the method is illustrated on the original eigenspectrum (after the transformation $\mathbf{1}$). On the right, the extraction takes place after the power method was applied.

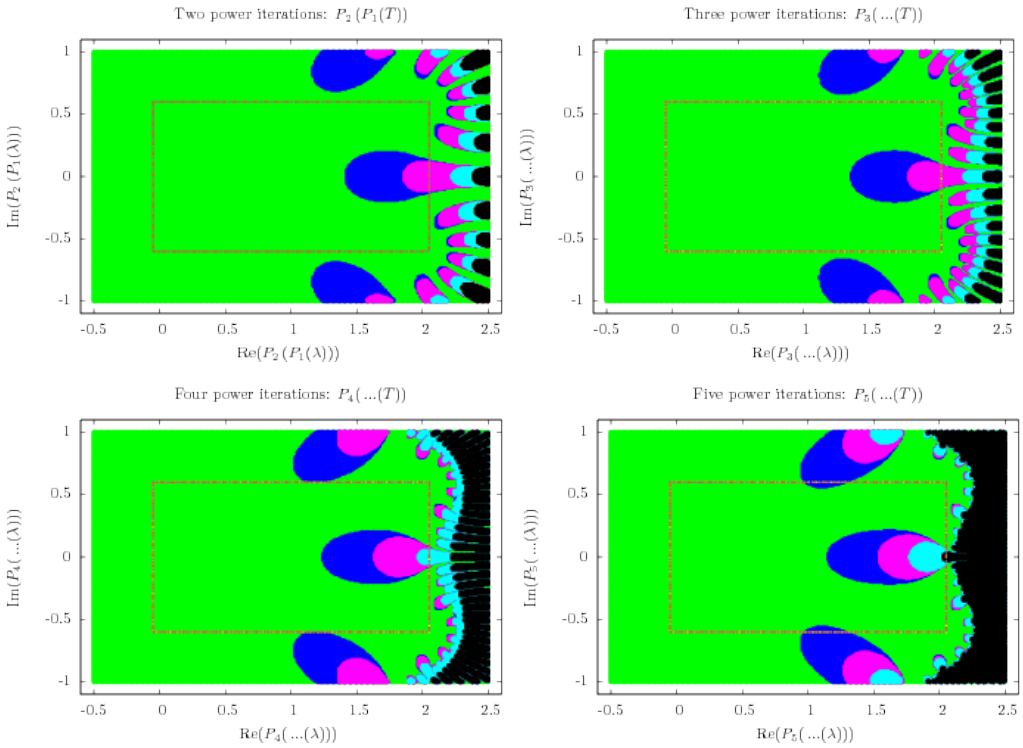

Figure 6.23: Spectral windows for successive power transformations. The *peeling* strategy is similar to the one presented above. For each iteration of the power method, the parameters are readjusted. $2.0 \cdot \mathbf{1} - D_W$ eigenspectrum typically lies within the red, rectangular shape. The extraction becomes deeper as the iterations number increases and a fractal-like form arises. The order of P_5 is 528.

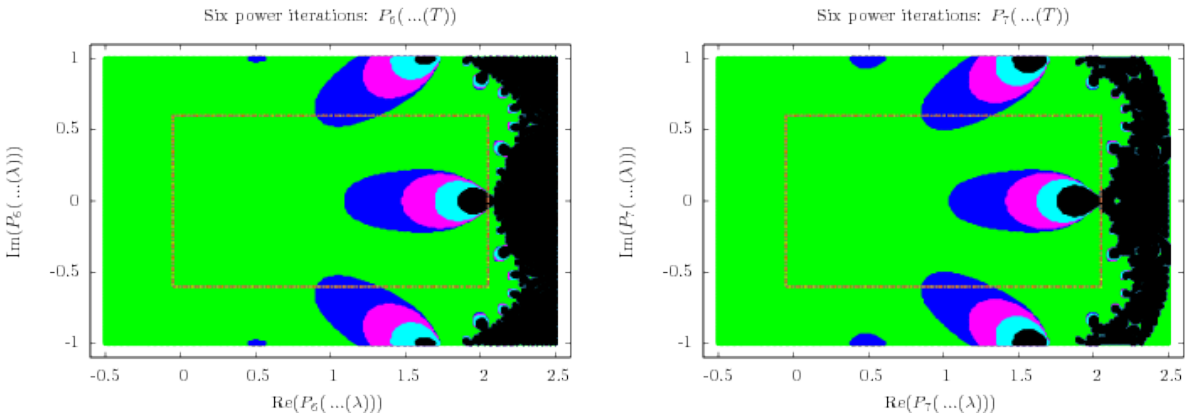

Figure 6.24: Further iteration start to lengthen the tunnel appearing around 2. This guarantees an efficient extraction of the complex eigenvalues with very low imaginary part. The green section on the fractal boundary right comes from a numerical cut-off (the values given after the polynomial transformations are too large). The order of P_7 is 50688.

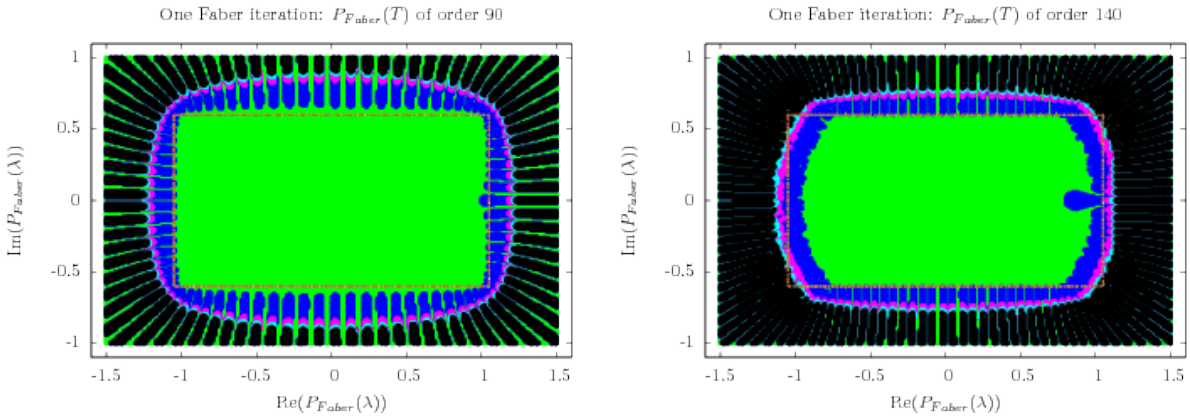

Figure 6.25: Spectral windows for Faber polynomials. The polynomial strategy is presented in Fig.(6.12) and the transformation reasonably achieves what it is expected to do. The oscillating boundaries show that important rotations occur outside of the polygonal hull.

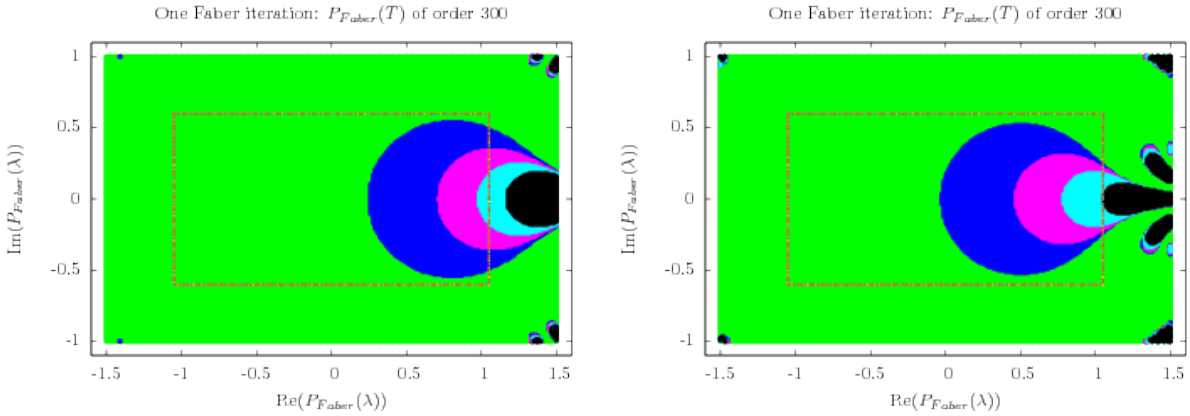

Figure 6.26: Spectral windows for two alternative Faber polynomial showing reasonable extraction properties. The left figure comes from a strategy presented in Fig.(6.13). The right one was built with an alternative strategy.

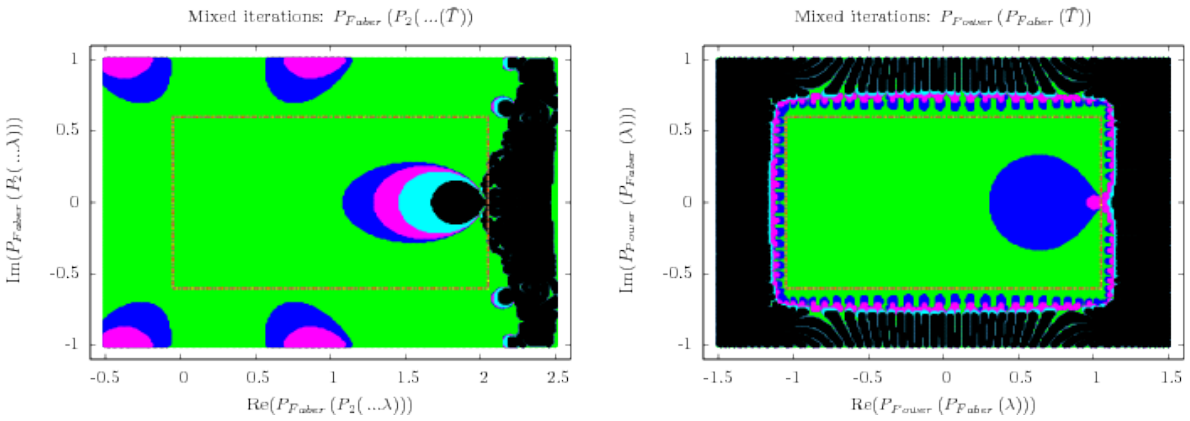

Figure 6.27: Spectral windows for mixed strategies mixing Faber/Power polynomials. The left strategy is represented in Fig.(6.20). The right are from Fig.(6.21).

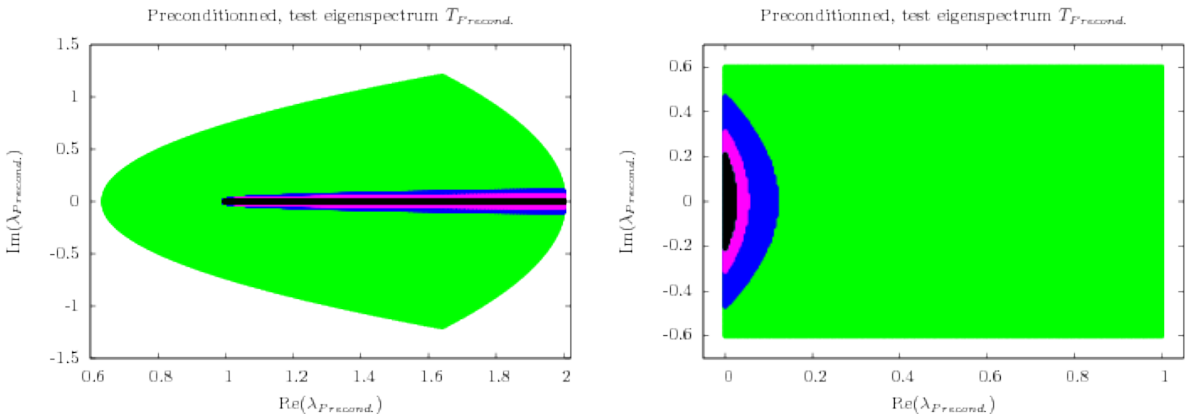

Figure 6.28: Peeling strategy with the even-odd preconditioned Wilson-Dirac operator. A typical eigenspectrum $D_{precond.}$ is represented on the left. The right window shows that the preconditioning acts as an explicit restarting. The supposedly extracted eigenvalues are plotted on the eigenspectrum left.

6.4 Strategies performances, a numerical comparison

As seen previously, the design of transformation polynomials is arbitrary and approximative.

The method efficiency depends on the eigenspectrum shape, the number of eigenvalues computed, the transformation polynomial order and the required precision. In addition to this, as discussed in section 6.1, the Arnoldi algorithm realises only approximately the LR mode (this issue is improved, as the eigenvalue density is decreased). Therefore, a methodical comparison is difficult to establish.

The test proposed here consists in testing fair representants of the approaches described above on a few eigenspectra. The eigenvalues extracted are compared with the corresponding spectral windows. As more eigenvalues are computed, the extraction windows are expected to scale following the patterns presented in the spectral windows of section 6.3. The time performance are presented in Table (6.1). Recall that the computation time increases almost exponentially with the number of computed eigenvalues.

Fig.(6.30) demonstrates that well designed extraction strategy allows for an extraction of the Wilson-Dirac inner eigenvalues operator up to the doublers.

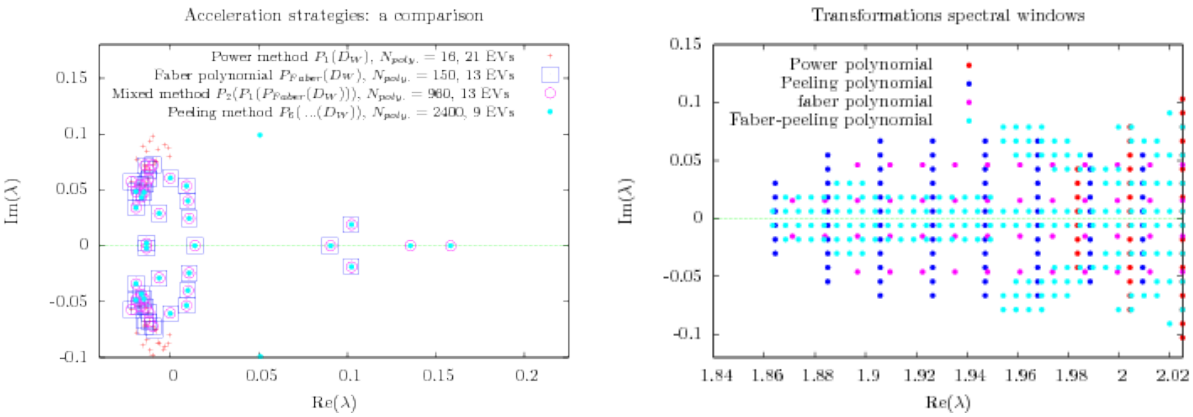

Figure 6.29: In real computations, the computational depth depends on the eigenvalues distribution. Therefore, the transformation performances were tested on a set of three $8^3 \times 16$ configurations ($N_f = 1$ QCD, $\beta = 4.0$, $\kappa = 0.1460$). The eigenvalues of the transformed eigenspectra were computed (with LR mode) and reproduced on D_W from the eigenvectors, as shown on the left window. If the number of eigenvalues are increased, the domains of computed eigenvalues are expected to increase approximately along the spectral windows patterns, as they are approximately represented on the right. Since the computation time depends exponentially of the number of computed eigenvalues, the power method is clearly the less effective, although its convergence is the fastest here.

Power	Faber	Mixed	Peeling
178 s.	1179 s	4188 s	8441 s

Table 6.1: Computation times for the different methods. Averages on three configurations with an error of $\sim 30\%$.

6.5 Further issues

6.5.1 Computation with even/odd-preconditioned Dirac-operator

As seen in the section 3.3.7, the preconditioning has for effect to transform the eigenvalues as $\lambda \to \bar{\lambda} = 2\lambda - \lambda^2$, which is a bijection for the real eigenvalues $|\lambda| \leq 2$.

Therefore, the even/odd-preconditioning can be seen as an "accelerating preconditioning for free". In addition to this, only one half of the matrix elements is involved in a preconditioned Matrix computations. Therefore, the preconditioning procedure halves the eigenproblem size, while the memory required by the Arnoldi algorithm is divided by 4 and the eigenvalue density is efficiently lowered.

Evidently, the polynomial transformations applied has to be adapted making use of the idea introduced in the last sections and the even/odd-preconditioned Dirac-operator eigenspectrum particular shape. The even/odd preconditioned version of the D_W was successfully applied in practice, improving the performances. An example is illustrated in Fig.(6.31).

6.5.2 Deflation

One may think of applying deflation ideas with the converged eigenvectors through Schur projections $D_W \to \tilde{D}_W = W^\dagger D_W W$ observing
$P(\tilde{D}_W) = W^\dagger P(D_W) W$. In this case, W is a the projector onto the space perpendicular to the one spanned by the converged eigenvectors. The non-normality of D_W implies $W \neq \mathbf{1} - VV^\dagger$, with V having D_W's converged and normalised eigenvectors in its columns.

More realistically, one may consider the transformation $P(D_W) \to P(D_W) - VP(\Gamma)V^+$, where Γ contains in its diagonal the eigenvalues of the converged eigenvectors of D_W.
In practice, deflation was not implemented, as the method imply the storage of very large vectors.

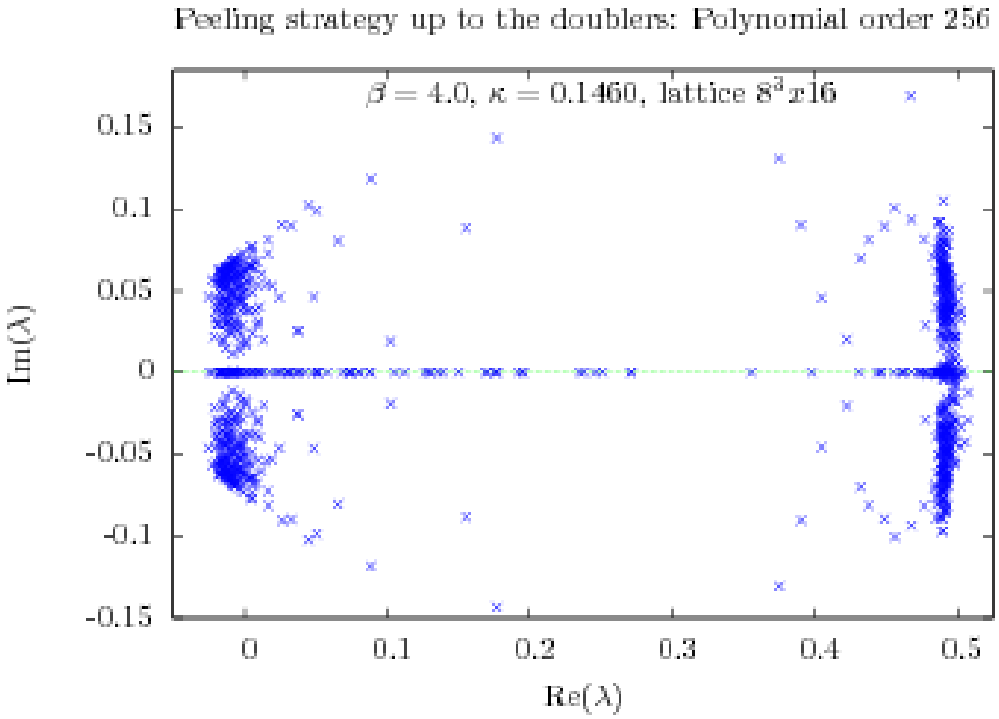

Figure 6.30: For one flavour QCD, the peeling strategy applied on D_W allows for a partial extraction up to the doubler modes. 100 configurations are summarised. This result was systematically achieved with a reasonable polynomial order ($P_{peeling} = 625$) and computing the 24 lowest eigenvalues (after peeling) only.

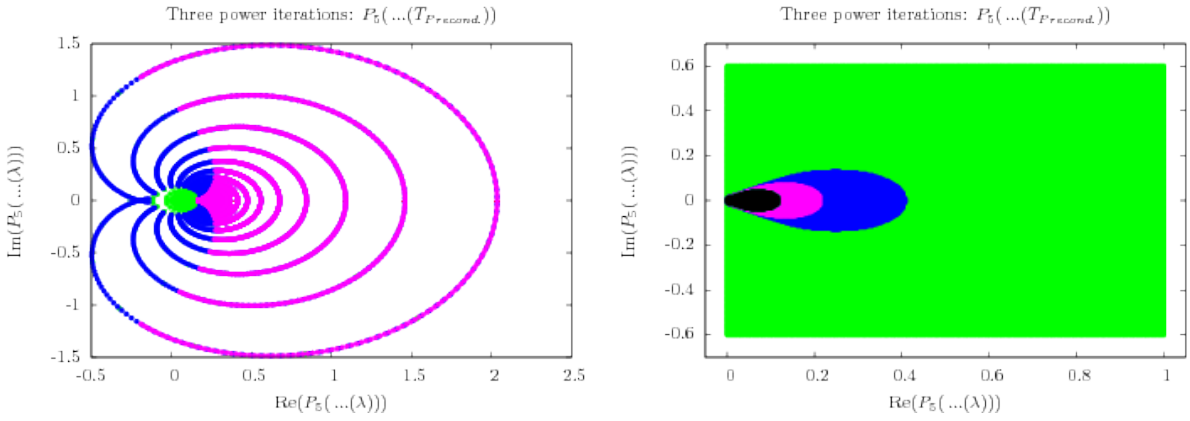

Figure 6.31: Transformation of order 240 are already ivery efficient with the even-odd preconditioned Wilson-Dirac operator. This is illustrated through the transformed eigenspectrum on the left figure and its corresponding spectral window on the right.

Chapter 7

Determinant, Pfaffian sign problem and eigenvalue distributions

In the one flavour projects considered, the determinant or Pfaffian sign problem enters in the analysis only as a perturbation corrected through reweightings and the discussion is organised from the available data.

The determinant or Pfaffian sign dependance of parameter as κ, β, the lattice volume and the correction factors are discussed. Because the determinant sign directly depends on D_W real eigenvalues, their distribution is studied here. As no analytical relation is known between the lowest eigenvalues of D_W and Q (see section 3.3.6), the opportunity is taken to compare their low eigenspectra.

For statistical reasons, the study is performed on stout-smeared configurations. For one flavour QCD, configurations with low, negative quark masses were studied only. In such a setup, the determinant sign appears to have an important impact. Equivalently, in $\mathcal{N} = 1$ Sym, the Pfaffian sign problem becomes acute as the gluino mass is low or negative.

7.1 The sign problem in practice

7.1.1 Determinant sign history

For the one flavour QCD, Fig.(7.1) reviews determinant sign histories. Results for $\langle\sigma\rangle = (N_+ - N_-)/(N_+ + N_-)$ are summarised in Table (7.1) and give a measure of the sign problem. N_+ and N_- are respectively the number of collected positive and negative determinant or Pfaffian signs as they vary along the Monte-Carlo history.

7.1.2 β, κ, lattice volume dependance

One flavour QCD: lattice volume and κ-dependance

Depending on the lattice volume, $\langle\sigma\rangle$ varies differently as κ is tuned. This is illustrated in Table (7.1) and in Fig.(7.2), where $\langle\sigma\rangle(m_{phys.})$ is evaluated. For

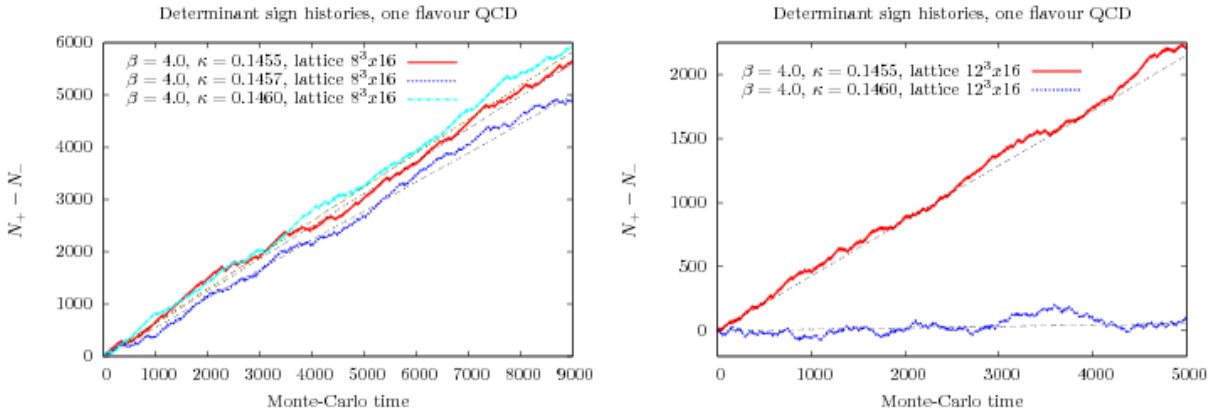

Figure 7.1: Histories of the determinant sign computation for one flavour QCD. the lattices sizes are $8^3 \times 16$ and $12^3 \times 16$, $\beta = 4.0$. $N_\pm$ are the number of collected positive/negative determinant signs and vary along the Monte-Carlo history. For $\mathcal{N} = 1$ Sym, the histories of the Pfaffian sign are comparable.

both the 8^3x16 lattice, the lowest real eigenvalue distributions are represented in Fig.(7.3) and compared with the 12^3x16 ones in Fig.(7.4).

Following Fig.(7.3), as κ is increased, the lowest real eigenvalues appear to fluctuate deeper into the negative domain. Recall that the determinant sign is simply given by the number of negative real eigenvalues of D_W. Therefore, for large eigenspectra (with a large number of real eigenvalues) $\langle\sigma\rangle$ is expected to decrease before it stabilises around $\langle\sigma\rangle \approx 0$ when κ is increased (more real eigenvalues are expected to enter into the negative domain and random fluctuations of their number imply $\langle\sigma\rangle \approx 0$).

According to the above discussion, Fig.(7.2) is unexpected for the 8^3x16 lattice while the $12^3 \times 16$ case is very likely to be representative of the standard behaviour. Under the hypothesis that no physical effects influence the 8^3x16 scenario, the explanation lies probably in the different distributions of the lowest, real eigenvalues.

For the 12^3x16 lattice, the lowest real eigenvalues were collected mostly in the negative domain, as numerous second and third lowest, real eigenvalues were. As argued above, $\langle\sigma\rangle \approx 0$ is expected from their fluctuations.

In contrast, less real eigenvalues are found on 8^3x16 lattice. The fact, that $\langle\sigma\rangle$ increases despite of this is explained by an increasing number of second real eigenvalues entering into the negative domain. Let us mention that $\langle\sigma\rangle$ showed large fluctuations in subsamples of the ~ 10000 considered configurations.

κ	N_+	N_-	$\langle\sigma\rangle$
0.1452	4668	1675	0.47
0.1455	5649	1883	0.5
0.1457	8217	2345	0.56
0.1460	8566	1833	0.64

κ	N_+	N_-	$\langle\sigma\rangle$
0.1452	3721	1484	0.2(2)
0.1455	3725	1880	0.1(5)
0.1460	2823	2757	0.0(1)

Table 7.1: lattice 8^3x16: lattice 12^3x16:

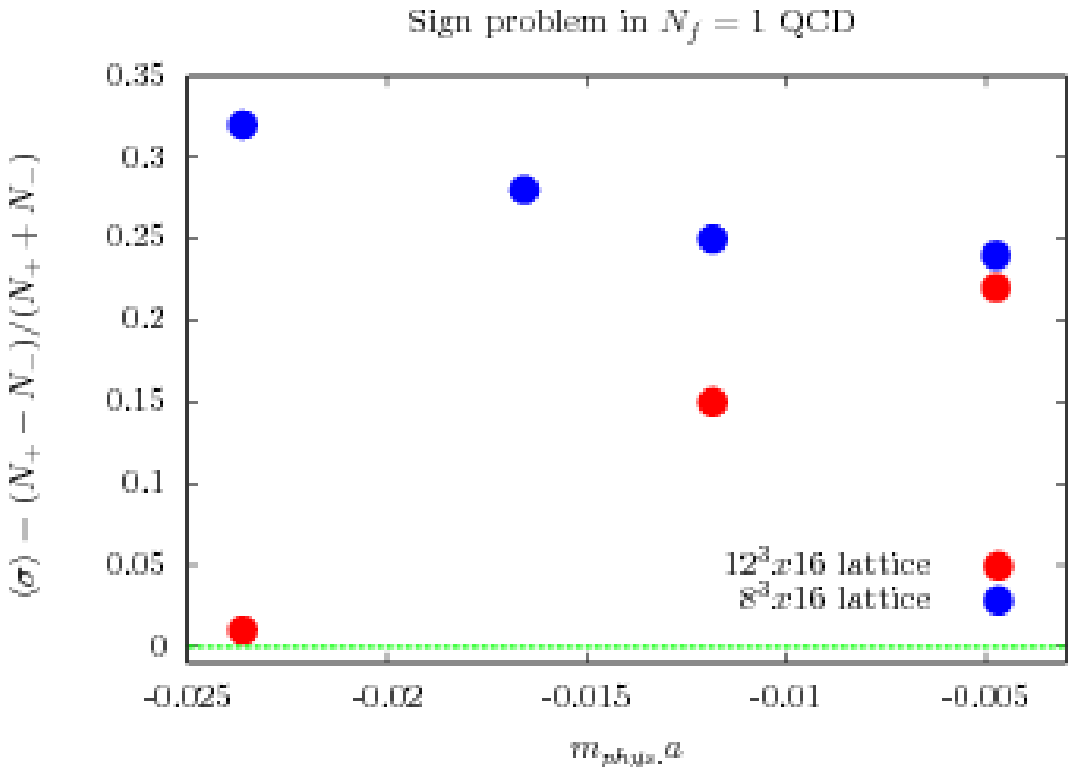

Figure 7.2: $[\sigma](m_{phys.}a)$ for different lattice sizes. The physical quark mass is set as $am_{phys.} = \frac{1}{2\kappa} - \frac{1}{2\kappa_{crit.}}$. The picture is not as expected (see discussion above) as the results completely differs for different lattice sizes. $\kappa_{crit.} = 0.145$ is an approximation found through the study of the particle spectrum with a partially quenched extension of one flavour QCD [62].

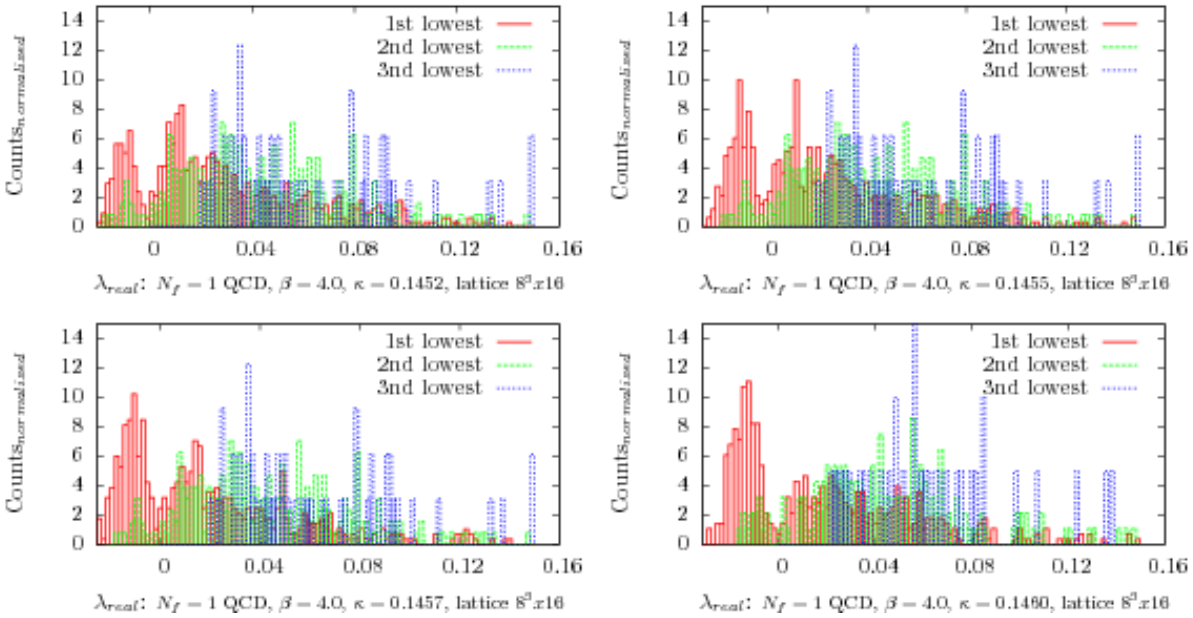

Figure 7.3: Distributions of the lowest real eigenvalues, as they were found for the one flavour QCD with even-odd preconditioned Wilson-Dirac operator. As κ increases, the distribution is shifted and the peak in the negative sector increases. The plots are approximative since a lowest, real eigenvalue could be extracted for $\approx 85\%$ of all configurations in practice. The lowest eigenvalues distributions are reliable up to 0.05.

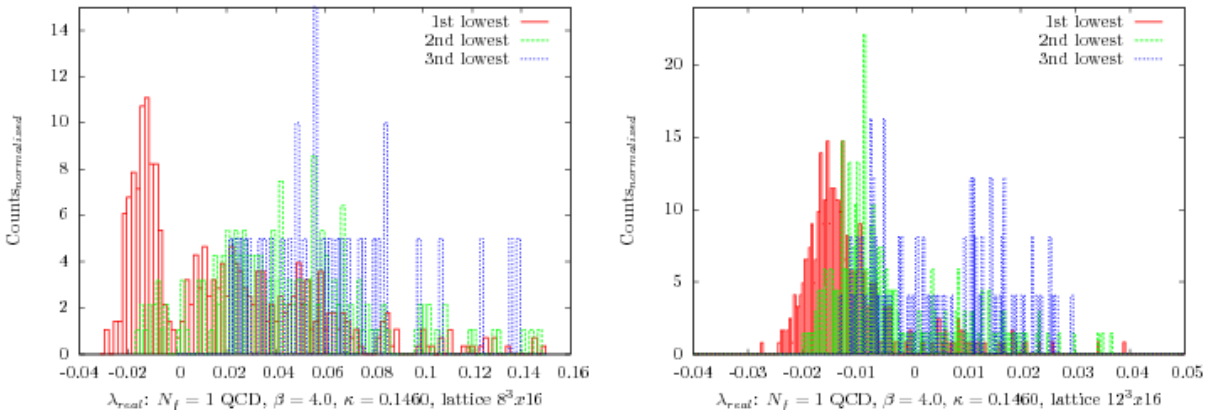

Figure 7.4: For similar κ but different lattice sizes (8^3x16 vs 12^3x16), the eigenvalue distributions of the lowest, real eigenvalues peak approximately at the same point. However, the density of real eigenmodes is higher and more real eigenvalues enter the negative plane for 12^3x16. For the 12^3x16 lattice also, a lowest real eigenvalue could be detected in $\approx 90\%$ of all configurations, while the lowest eigenvalues distributions are reliable up to 0.01.

7.1.3 Determinant sign, autocorrelation times

The determinant sign histories of Fig.(7.1) hint at some autocorrelation in Monte-Carlo time. As the determinant sign problem becomes critical ($\langle\sigma\rangle \approx 0$), autocorrelation times can be roughly evaluated. This is shown in Fig.(7.5), where the autocorrelation time for the determinant sign is found to be long (in comparison with other observables).

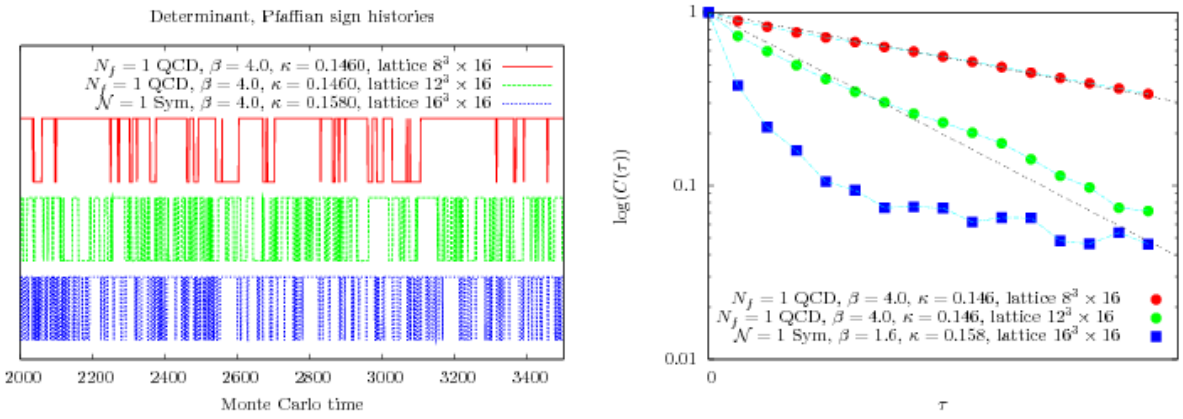

Figure 7.5: On the left, determinant or Pfaffian sign histories are compared for one flavour QCD with different lattice sizes and for $\mathcal{N} = 1$ Sym for 16^4. On the right, as the sign problem becomes critical $\langle\sigma\rangle \approx 0$, autocorrelation time $\tau_{\sigma,\,\mathrm{exp.}}$ can be approximately evaluated studying the determinant sign correlation function decays. For example, on $12^3 \times 16$ lattices, one finds $\tau_{\sigma,\,\mathrm{exp.}} = 20 \pm 5$ for $\kappa = 0.1460$.

7.1.4 Computational precision

In practice, the determinant or Pfaffian sign computations are based on evaluations of the smallest real eigenvalues λ_D of D_W. Fig.(7.6) discusses the smallest real eigenvalue extraction quality. This was done on $\mathcal{N} = 1$ Sym configurations comparing computations performed with different transformation polynomials and Dirac operators (D_W and its even-odd preconditioned version).

As expected from the discussion of chapter 6, after polynomial transformation, the outmost left eigenvalues are extracted with a very good precision, while the inner eigenvalues are less precisely evaluated. This can be observed in Fig.(7.6). For the sample of configurations studied, the signs evaluated with different approaches were similar.

As discussed in Appendix C, doublers appeared in the $\mathcal{N} = 1$ Sym case, which complicates the Pfaffian sign analysis.

7.2 The determinant sign and other quantities

As simulations are performed, additional quantities are required and evaluated, as the lowest eigenvalues of the hermitian Wilson-Dirac operator $Q^\dagger Q$ and the

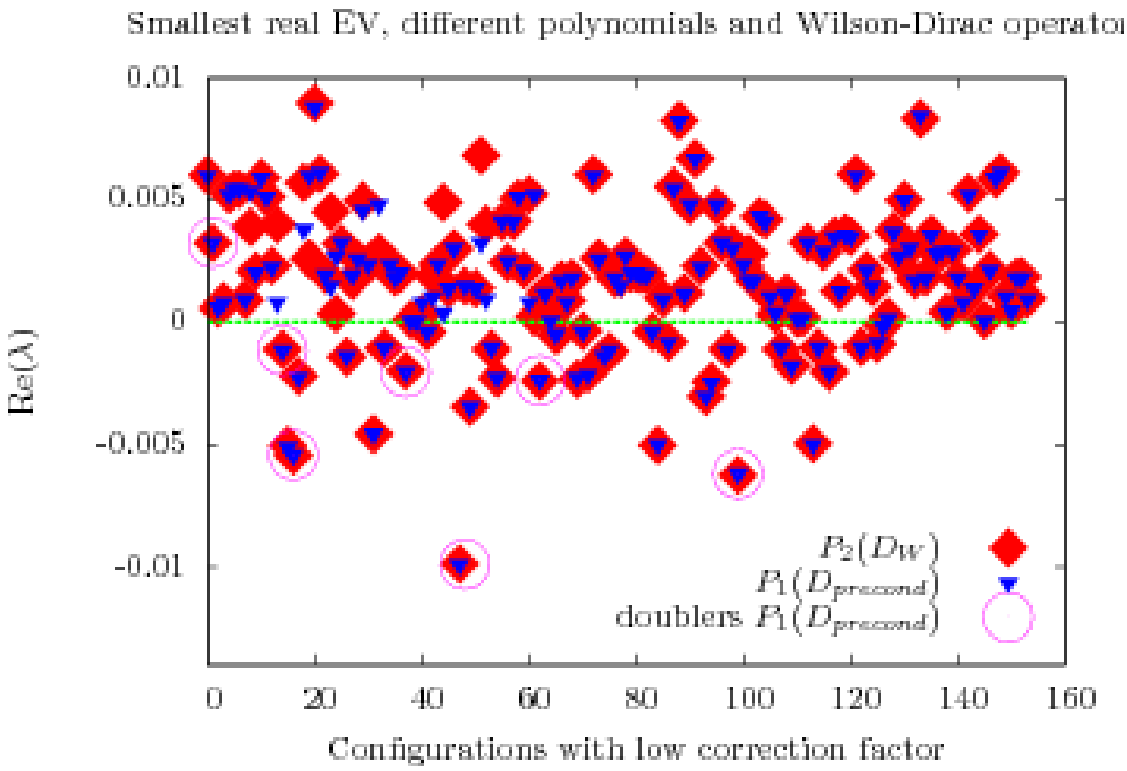

Figure 7.6: For 100 $\mathcal{N}=1$ Sym configurations, the lowest eigenvalues λ_{D_W} and $\lambda_{D_{prec}}$ were found respectively on the eigenspectra $P(D_W)$ and $\tilde{P}(D_{prec})$, after polynomial transformation of the nonhermitian D_W and preconditioned D_{prec} Wilson-Dirac operators. The polynomials P and $\tilde{P}$ are different. The negative real eigenvalues as well as the Pfaffian signs of both approaches coincide.

correction factor[1]. Since the determinant sign computations are relatively expensive, it is interesting to investigate whether an alternative evaluation of the determinant sign is possible from other quantities, as this might be suggested considering Fig.(7.7).

Although the correction factors are only approximately related to the Wilson-Dirac operator, they are considered first. Fig.(7.8) emerges under simple comparisons. Depending on κ value, the lowest real eigenvalues of the non-hermitian Wilson-Dirac operator D_W are partially distributed in the negative domain. Therefore, the correction factor becomes completely inappropriate for the determinant or Pfaffian sign evaluation (as shown in the lowest right window of Fig.(7.8)).

In the next section, the smallest eigenvalues of $Q^\dagger Q$ are related to their smallest counterpart of D_W instead of the determinant or Pfaffian signs.

[1]The correction factors are computed for configurations where very small eigenvalues of $Q^\dagger Q$ are found. They are generated through a stochastic noisy correction step and reweight the configurations generated outside of a computational range where the algorithm behaviour is well under control [45].

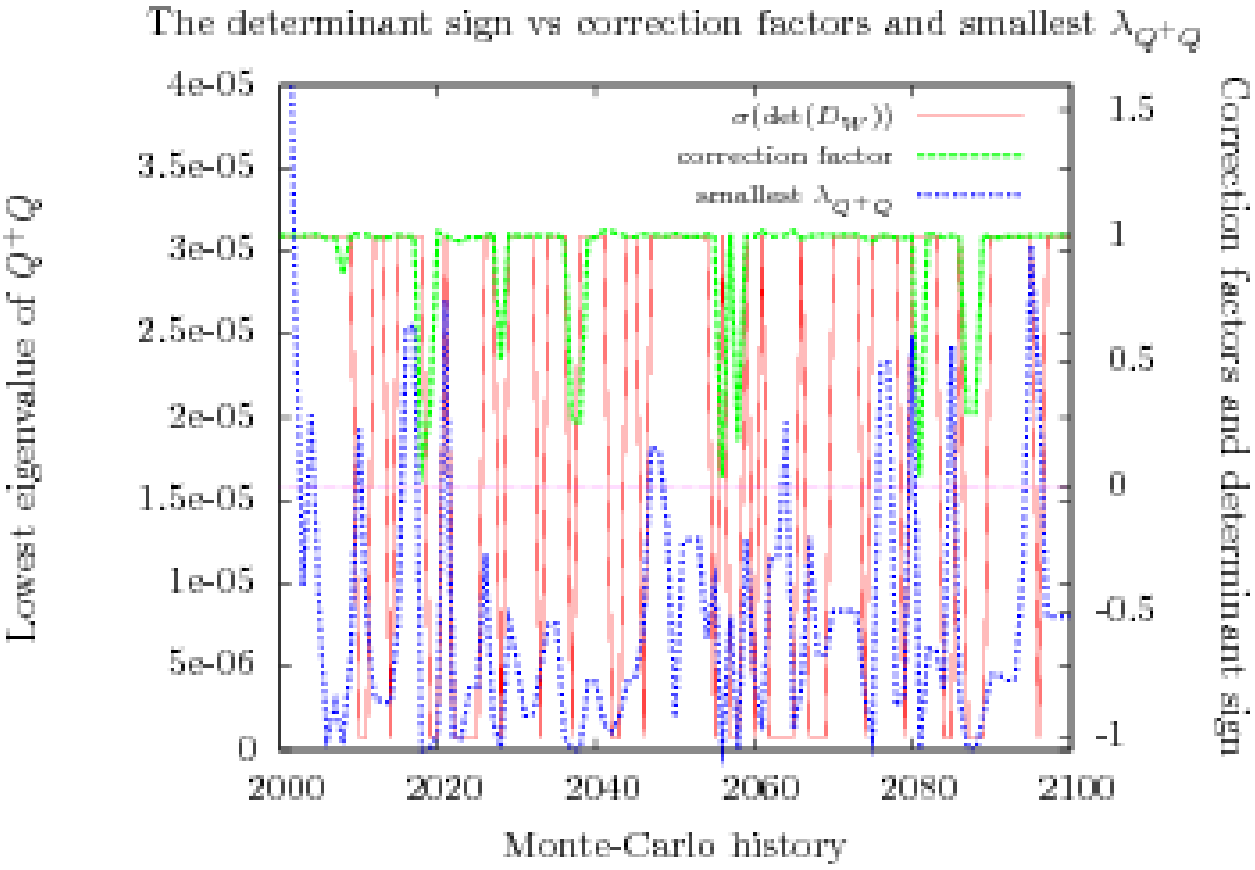

Figure 7.7: For $\mathcal{N} = 1$ Sym, $\beta = 1.6$, $\kappa = 0.1580$ and lattice 16^4, a comparison is presented of the Pfaffian signs, the correction factors as well as the lowest eigenvalues of $Q^\dagger Q$ (Q is the hermitian Wilson-Dirac operator) along the Monte-Carlo history.

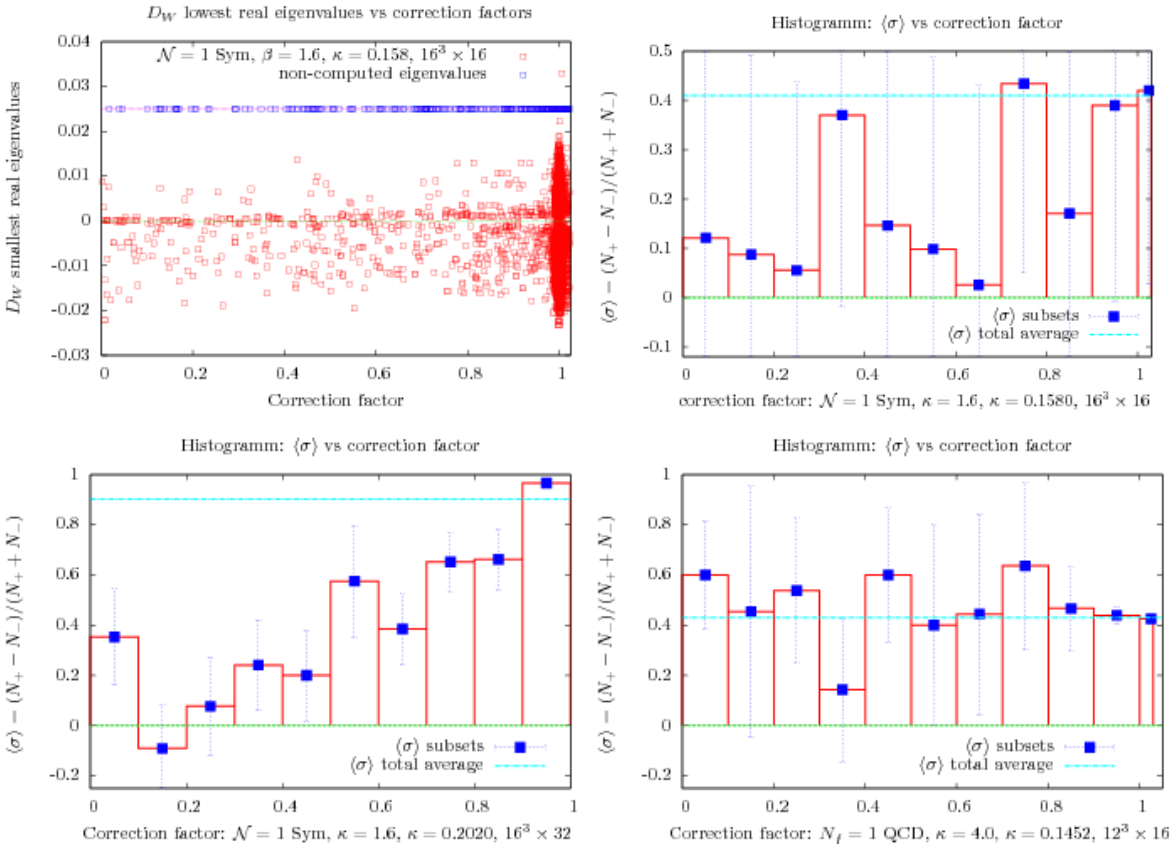

Figure 7.8: On the upper left, the lowest real eigenvalue is distributed against the correction factors. In many cases, no real eigenvalue could be computed. Those configurations are made visible with blue points along a line at ~ 0.025. On the other windows, for both one flavour theories, the corrections factors were decomposed into 11 sectors and the "probability" of finding negative determinant signs is measured with $\langle\sigma\rangle$. The turquoise line represents $\langle\sigma\rangle$ averaged over the whole sample. As expected, for low or negative mass parameters, the correction factors are not correlated with the determinant or Pfaffian sign anymore.

7.3 Comparisons between the low eigenvalues of the hermitian and non-hermitian Wilson-Dirac operators

As mentioned in section 3.3.6, no analytic relation is known between the hermitian and non-hermitian Dirac operators low eigenspectra. Nevertheless, in continuum, the lowest eigenvalues of D and Q were observed in section 3.2.4 to be related through

$$\lambda_Q = \pm\sqrt{\lambda_D^2 + m^2}, \tag{7.1}$$

which is not exactly realised on the lattice. However, eq.(3.12) forces the zero eigenmodes of Q to be zero eigenmodes of D_W. In addition to this, it is interesting to observe that the lowest eigenvalues are distributed inside of boundaries partially and approximately reproducing the continuum relation of eq.(7.1).

Thus, one may have the possibility to partially retrieve the lattice parameters from the eigenspectra. For that reason, a relation of form $(x-a)^2/b$ is guessed and tested for $\lambda_{Q^+Q}(\lambda_{D_W})$ (and $(x-a)/\sqrt{b}$ for $\sqrt{\lambda_{Q^+Q}}(\lambda_{D_W})$). b is a parameter that had to be introduced in order to obtain decent fits. The parameter $a/\sqrt{b}$ is expected to be remnant of the mass setting.

Notice that the lowest eigenvalues found on both eigenspectrum, as they are plotted in the following figures, are not necessarily related one to one.

7.3.1 One flavour QCD project

Fig.(7.9), Fig.(7.10) and Fig.(**??**) illustrate this discussion for one flavour QCD. The eigenvalues are distributed outside parabolical or triangular shapes for $\lambda_{Q^+Q}(\lambda_{D_W})$ and $\sqrt{\lambda_{Q^+Q}}(\lambda_{D_W})$ respectively.

It turns out that the low eigenspectra of D_W and Q provides with some simple but very approximative lattice definition of the quark and gluino masses. Nevertheless, with this analysis, the picture is by far too imprecise and only the quark mass sign could be retrieven.

7.3.2 $\mathcal{N} = 1$ Sym project

In Fig.(7.12), a discussion similar to the previous one is presented for $\mathcal{N} = 1$ Sym. In addition to this, notice that the determinant sign could be computed for large lattices: 24^3x48 and 32^3x64 Fig.(7.12). As mentioned in the appendix C, such computations are made cheaper by the fact that eigenvalue doubling is mostly not detected in practical computations.

7.3.3 The determinant sign and the eigenvalues of Q

Fig.(7.13) discusses the frequency of negative determinant signs in relation with Q lowest eigenvalues. This is done in a regime with negative quark masses.

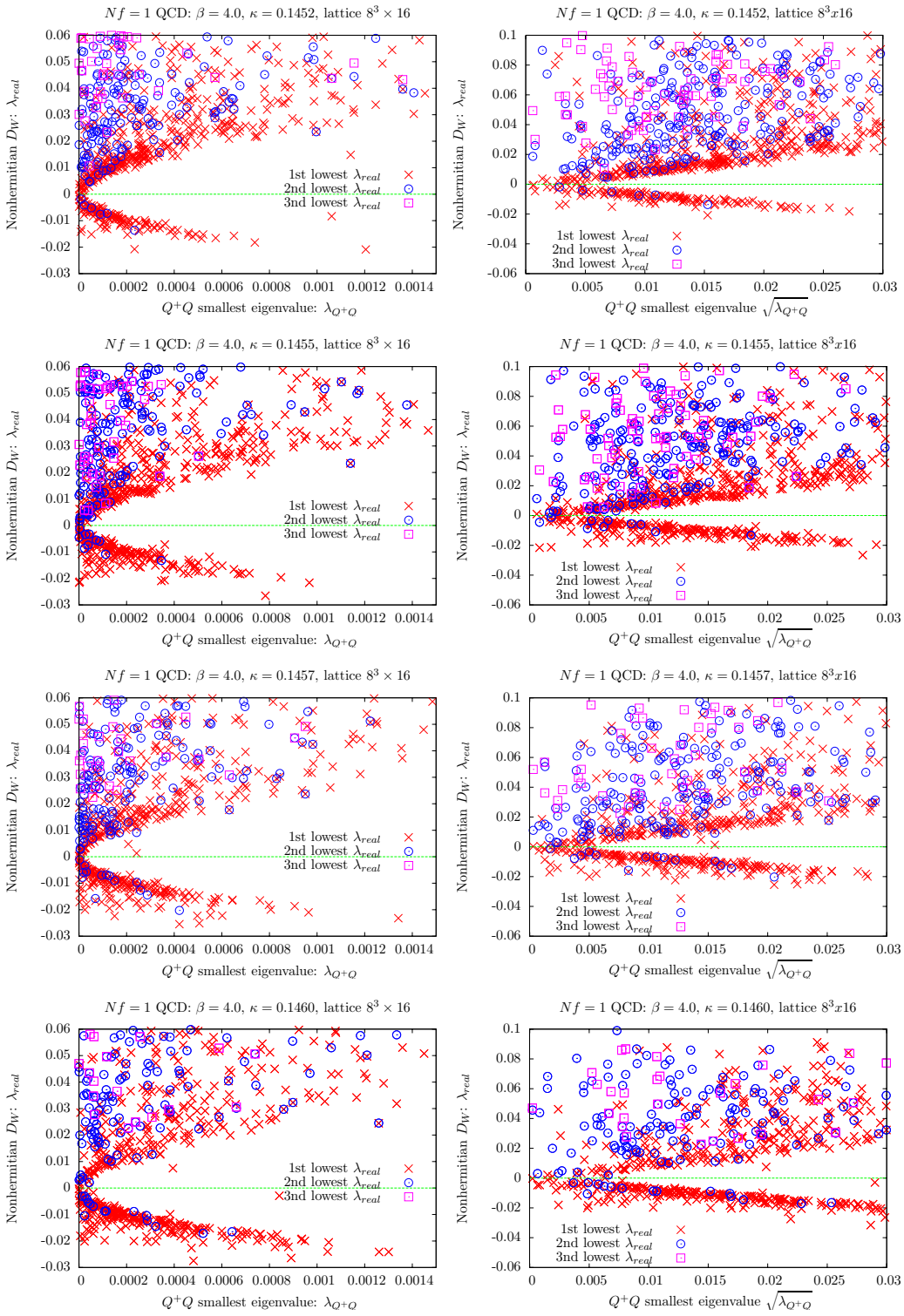

Figure 7.9: The distribution of relations $\lambda_{Q^+Q}(\lambda_{D_W})$ and $\sqrt{\lambda_{Q^+Q}}(\lambda_{D_W})$ for different simulations. Configurations where 1, 2 or 3 eigenvalues were found are represented only, which represents $\approx$ 85% of the whole configurations. The eigenspectra scatter outside of ellipsoidal $(\lambda_{Q^+Q}(\lambda_{D_W}))$ or triangular $(\sqrt{\lambda_{Q^+Q}}(\lambda_{D_W}))$ domains.

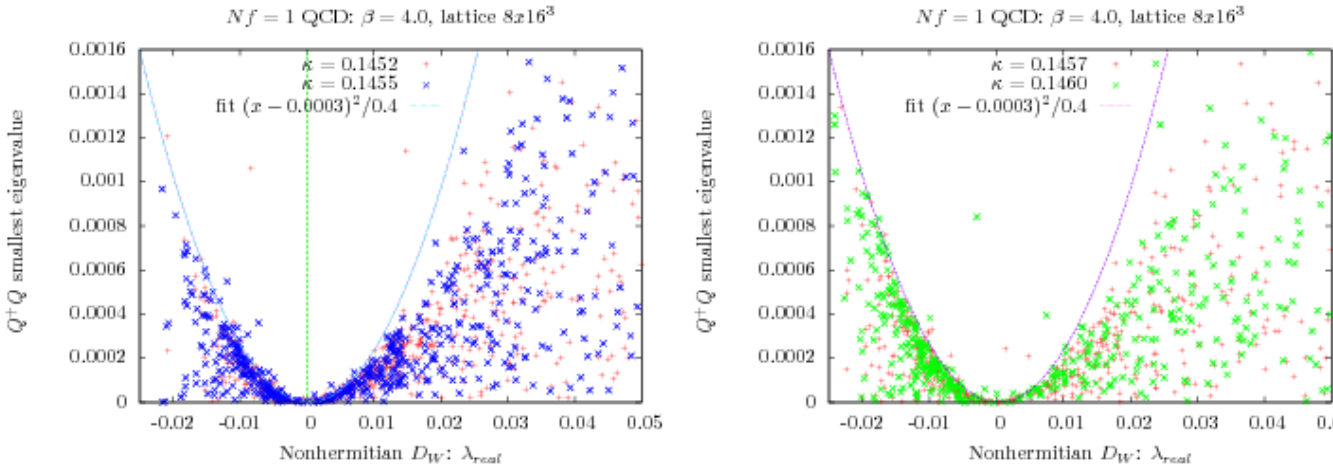

Figure 7.10: With the lowest eigenvalue, the results showed in eq.(7.8) for $\lambda_{Q^+Q}(\lambda_{D_W})$ are presented testing a fit $(x-a)^2/b$. Following the idea, that the continuum relation are approximately realised on the lattice, one would expect a slight shift for the eigenspectra, for different κ's. However, the distributions are too approximative and only one fit is proposed. This fit is only satisfying on the left part, but it clearly suggests a negative value for a. Notice that the lowest eigenvalues of D_W and Q^+Q are not necessarily related one to one.

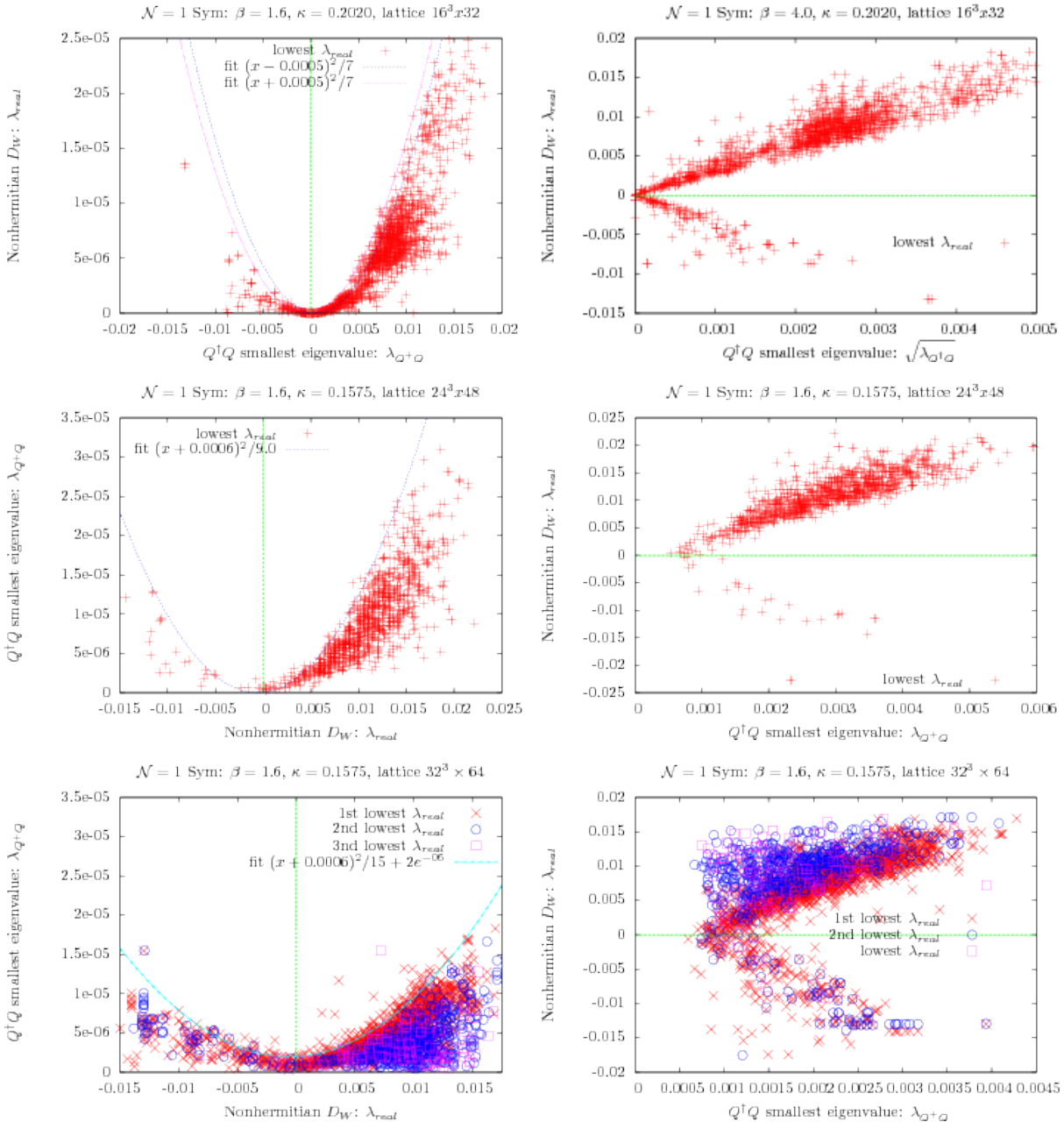

Figure 7.11: Distributions of the lowest eigenvalues for large lattice. For the latice 16^3x32, a visual discussion of the parameter a (fits $(x-a)^2/b$) is proposed. On the right figure, the two lowest distributions show a gap around 0 for the eigenvalues of Q. This reflects a precision issue for λ_{Q^+Q}, which are computed with less precision for large lattices.

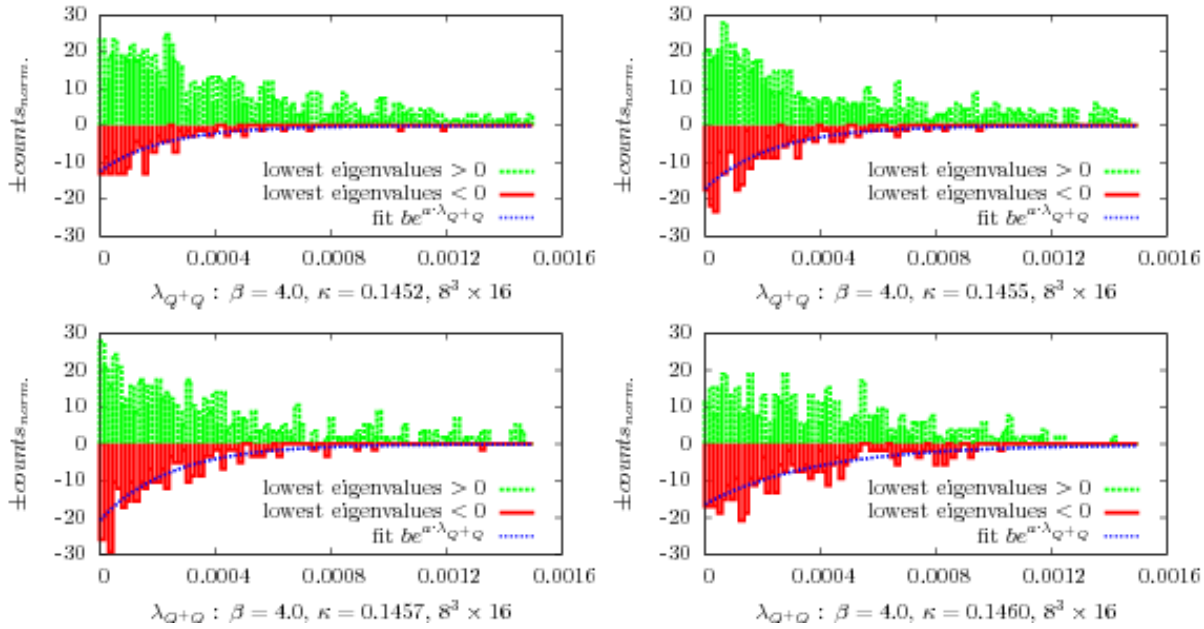

Figure 7.12: Bar diagram illustrating distributions of the lowest eigenvalues of Q^+Q. The green and red sets distinguish between sets of configurations with positive and negative smallest real eigenvalues of D_W. The blue line is a fit of the form $f(x) = be^{-a\lambda_{Q^+Q}}$, and provide with a more reasonable estimation for the probability of finding negative determinant as the one made with the correction factors (Fig.(7.7), Fig.(7.8)).

Chapter 8

One flavour QCD project and results

As stated in the introduction, the particle mass spectrum and the phase structure of the one flavour QCD theory are under study.

8.1 Mass spectrum study

As the mass spectrum was studied, determinant sign fluctuations were found for the largest κ's. The determinant sign fluctuations affected the masses up to $\approx 7\%$. If found to be relevant, those corrections are listed in [64], [63], [62], [62] and recent results for the particle spectrum are summarised in Fig.(8.1).

8.2 Comparisons related to planar equivalence

From the mass spectrum of one flavour QCD, results expected from an approximated planar equivalence relation (at large N_c) could be tested. A theoretical prediction concerning the η_s and σ_s masses was found to be [11]

$$M_{\eta_s}/M_\sigma = \frac{N_c - 1}{N_c} 1 + \delta, \quad \delta \sim \mathcal{O}(1/N_c, (1/N_c)^2), \tag{8.1}$$

where δ is a theoretical uncertainty related to the fact that planar equivalence is only approximative with $N_c = 3$ and δ is of order $1/N_c$, or $(1/N_c)^2$. From the lattice computations, our results obtained with the one flavour theory are [62]

$$M_{\eta_s}/M_{\sigma_s} = 0.410, \;\; \delta = 0.23. \tag{8.2}$$

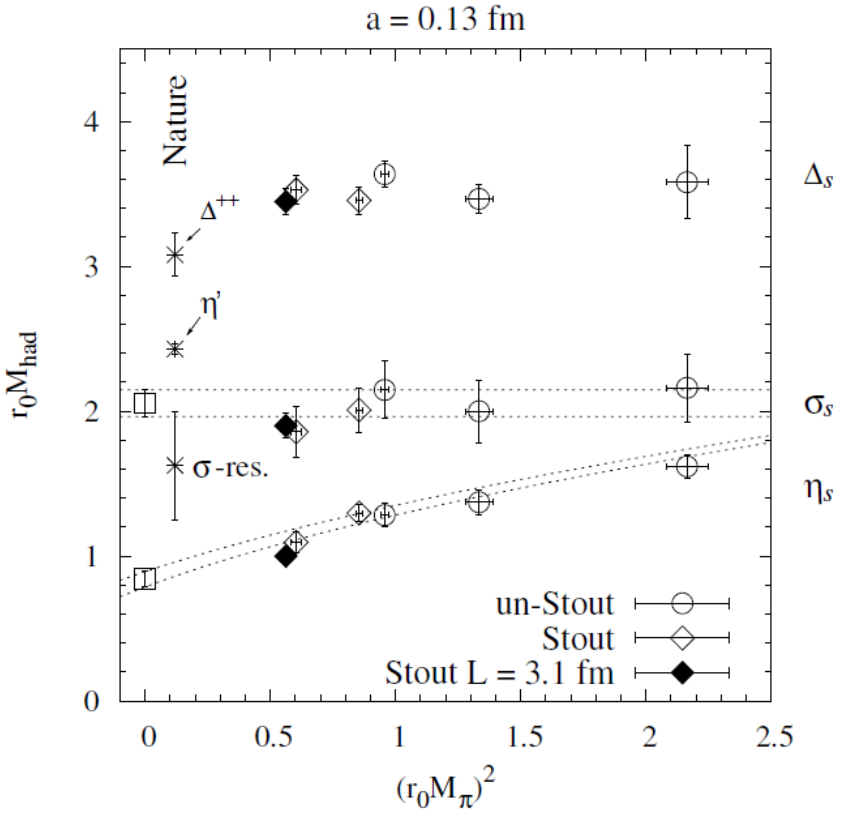

Figure 8.1: Results for the hadron spectrum of one flavour QCD as they were published in [62]. The masses of the η_s and σ_s particles are represented with their corresponding fits evaluated performing partially quenched chiral perturbation theory (PQχPT) [25].

8.3 Phase space structure

From the partially quenched one flavour theory particle spectrum, a critical $\kappa_{crit.}$ could be evaluated. Trying to realise the CP-symmetry breaking scenario proposed by Creutz, the bare quark mass is pushed further into the negative regime through tunings of $\kappa > \kappa_{crit.}$.

8.3.1 Spectral decomposition of the pseudoscalar condensate

In one flavour QCD on the lattice, a realisation of the CP-symmetry breaking phase is detected through the study of the pseudoscalar condensate $\langle\bar{\psi}\gamma_5\psi\rangle$. As seen in eq.(3.23), it can be decomposed as

$$\langle\bar{\psi}\gamma_5\psi\rangle = \mathrm{Tr}\,(Q) = \mathrm{Tr}\left(\gamma_5 D_W^{-1}\right). \tag{8.3}$$

Since the entire eigenspectrum can currently not be computed, the evaluation of $\mathrm{Tr}\,(Q)$ through spectral decomposition was performed using stochastic estimators for fermion loops [57] [55].

Alternatively, one considers the non-normal operator D_W, which spectral decomposition is studied in appendix B. Making use of eq.(B.9) and building the trace over the lattice points $x \in \mathcal{Z}_4$, it comes

$$\begin{aligned}\mathrm{Tr}\left(D_W^{-1}\gamma_5\right) &= \mathrm{Tr}\left(\sum_\lambda \frac{1}{\lambda}\frac{|R_\lambda\rangle\langle R_{\lambda^*}|}{\langle R_{\lambda^*}|\gamma_5|R_\lambda\rangle}\right)\\ = \sum_\lambda \frac{1}{\lambda}\frac{\sum_x |R_{\lambda,x}\rangle\langle R_{\lambda^*,x}|}{\langle R_{\lambda^*}|\gamma_5|R_\lambda\rangle} &= \sum_\lambda \frac{1}{\lambda}\frac{\langle R_{\lambda^*}|R_\lambda\rangle}{\langle R_{\lambda^*}|\gamma_5|R_\lambda\rangle}\end{aligned} \tag{8.4}$$

For normalised real, right eigenvectors $\{v_\lambda\}$, as computed by the Arnoldi algorithm on D_W, one sets $|R_\lambda\rangle \equiv v_\lambda$, $|R_{\lambda^*}\rangle \equiv v_{\lambda^*}$ and with $\chi_{latt.} = v_\lambda^\dagger\gamma_5 v_\lambda$, the spectral decomposition reads explicitly

$$\mathrm{Tr}\left(D_W^{-1}\gamma_5\right) = \sum_{\lambda\in\mathrm{R}}\frac{1}{\chi_{latt.}\lambda} + \sum_{\lambda\in\mathrm{C}}^{N_\mathrm{C}/2}\left[\frac{1}{\lambda}\left(\frac{v_{\lambda^*}^\dagger v_\lambda}{v_{\lambda^*}^\dagger\gamma_5 v_\lambda}\right) + \frac{1}{\lambda^*}\left(\frac{v_\lambda^\dagger v_{\lambda^*}}{v_\lambda^\dagger\gamma_5 v_{\lambda^*}}\right)\right], \tag{8.5}$$

where $N_\mathrm{C}/2$ is the number of complex conjugate eigenpairs in D_W eigenspectrum.

8.3.2 Situation in continuum

As explained in appendix B, the continuum Dirac operator is normal. As a result, its right eigenvectors form an orthonormal system and only the real eigenvectors $\lambda = \lambda^*$ contribute to the spectral decomposition (if $\lambda \in \mathrm{C}$, $\{v_{\lambda^*}, v_\lambda\}$ are orthonormal one another). Therefore, in continuum, eq.(8.4) becomes a sum over the $N_{\mathrm{zero.}}$ zero-modes

$$\mathrm{Tr}\left(D_W^{-1}\gamma_5\right) = \frac{1}{m_q}\sum_{\mathrm{i}}^{N_{\mathrm{zero.}}}\chi_i = \frac{n_+ - n_-}{m_q}, \tag{8.6}$$

with $n_\pm$ the number of zero-modes with positive/negative chirality. Eq.(8.6) actually holds since it reproduces the Atiyah-Singer theorem.

The correspondence with the lattice situation can be seen recalling that the real eigenmodes corresponds to the continuum zero modes and that $\chi \in \{\pm 1\}$ and in the continuum limes, only the real eigenmodes are expected to contribute.

In the continuum, the pseudoscalar condensate gets a value through (discrete) contributions from the topological sectors, as illustrated in Fig.(8.2).

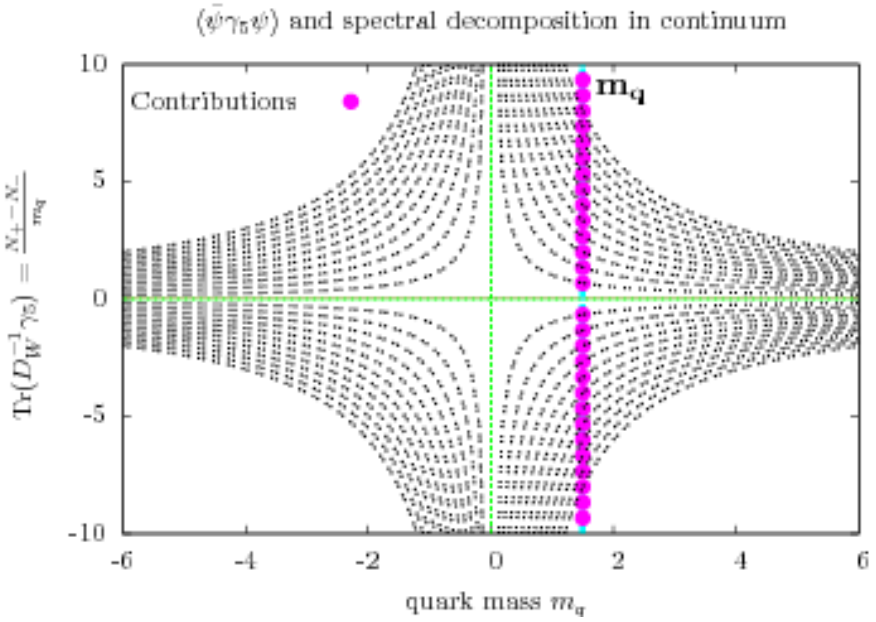

Figure 8.2: In continuum, the spectral decomposition of the pseudoscalar condensate is proportional to the topological charge, reweighted by the bare quark mass. As reconstructed from the eigenvalues of D_W, the pseudoscalar condensate is constructed from discrete contributions reweighted by a factor $1/m_q$.

8.3.3 Situation on the lattice

Departing from the continuum and normality, the spectral decomposition has to include additional, real contributions from the complex eigenpairs, as shown in eq.(8.5). In addition to this, the eigenvectors contributions are reweighted by $1/\lambda$.

Because of this and as suggested by the discussion in continuum, the real eigenmodes, which eigenvalues are the closest to zero are expected to play a major role in the pseudoscalar condensate reconstruction from a spectral decomposition.
This picture is tested and discussed in sections 8.4.

The pseudoscalar condensate and the topological charge

The standard connection with the topology is found via the flavour singlet axial vector current divergence relation (ABJ anomaly) and reads for $N_f = 1$

$$\partial_\mu(\bar{\psi}\gamma_5\gamma_\mu\psi) = 2m_q\bar{\psi}\gamma_5\psi + 2N_f q(x), \tag{8.7}$$

with $q(x)$ the topological density. Under integration over space-time with periodic boundaries, the partial derivative vanishes and one obtains

$$\nu = \kappa m_q\langle\bar{\psi}\gamma_5\psi\rangle = \kappa m_q \mathrm{Tr}(\gamma_5 D_W^{-1}). \tag{8.8}$$

8.4 The pseudoscalar condensate and the Wilson-Dirac operator eigenvalues

8.4.1 First observations on $8^3 \times 16$ and $12^3 \times 16$ lattices

With $\beta = 4.0$, for lattice sizes $8^3 \times 16$ and for κ varying between [0.1452, 0.1460], pseudo-scalar condensates were computed using stochastic estimators. In Fig.(8.3), the configurations were naively separated into subsets with different determinant signs. On the lattice $8^3 \times 16$, one observes two peaks for the pseudoscalar condensate distribution. As the lattice is expanded ($12^3 \times 16$), this feature disapears in Fig.(8.3).

8.4.2 Pseudoscalar condensate and the Wilson-Dirac eigenspectrum: the real eigenvalue contributions

The real eigenvalues numerical chirality distribution

The real eigenvalues enter eq.(8.5) with a weight inversely proportional to their right eigenvectors numerical chirality $\chi_{num.}$.

Typical distributions for $\chi_{num.}$ are studied in Fig.(8.5) and Fig.(8.6). $\chi_{num.}$ decreases slighty as the λ_{real} decreases (Fig.(8.5)). This suggests that the outer real eigenmodes are better lattice approximations of the continuum zero-modes, as in the continuum chirality $\chi = \pm 1$.

The distribution of $\chi_{num.}$ shows some asymmetry in Fig.(8.6), for $\beta = 4.0$, $\kappa = 0.1460$, lattice 8^3x16. This hints at the possibility that the simulation remained stuck in a topological sector.

Basical tests with the real eigenvalues

Eq.(8.5) indicates that the peaks observed in the pseudoscalar condensate distribution in Fig.(8.3) primarily depends on the lowest, real eigenvalues and their numerical chirality, rather than the determinant sign (In particular because of the factor $1/\lambda_{real}$ in eq.(8.5)).

In order to test this, configurations on which low, real eigenvalues were found are separately studied in Fig.(8.7). Two peaks could be reproduced in the pseudoscalar condensate distribution independently of the determinant sign and the following observations could be made:

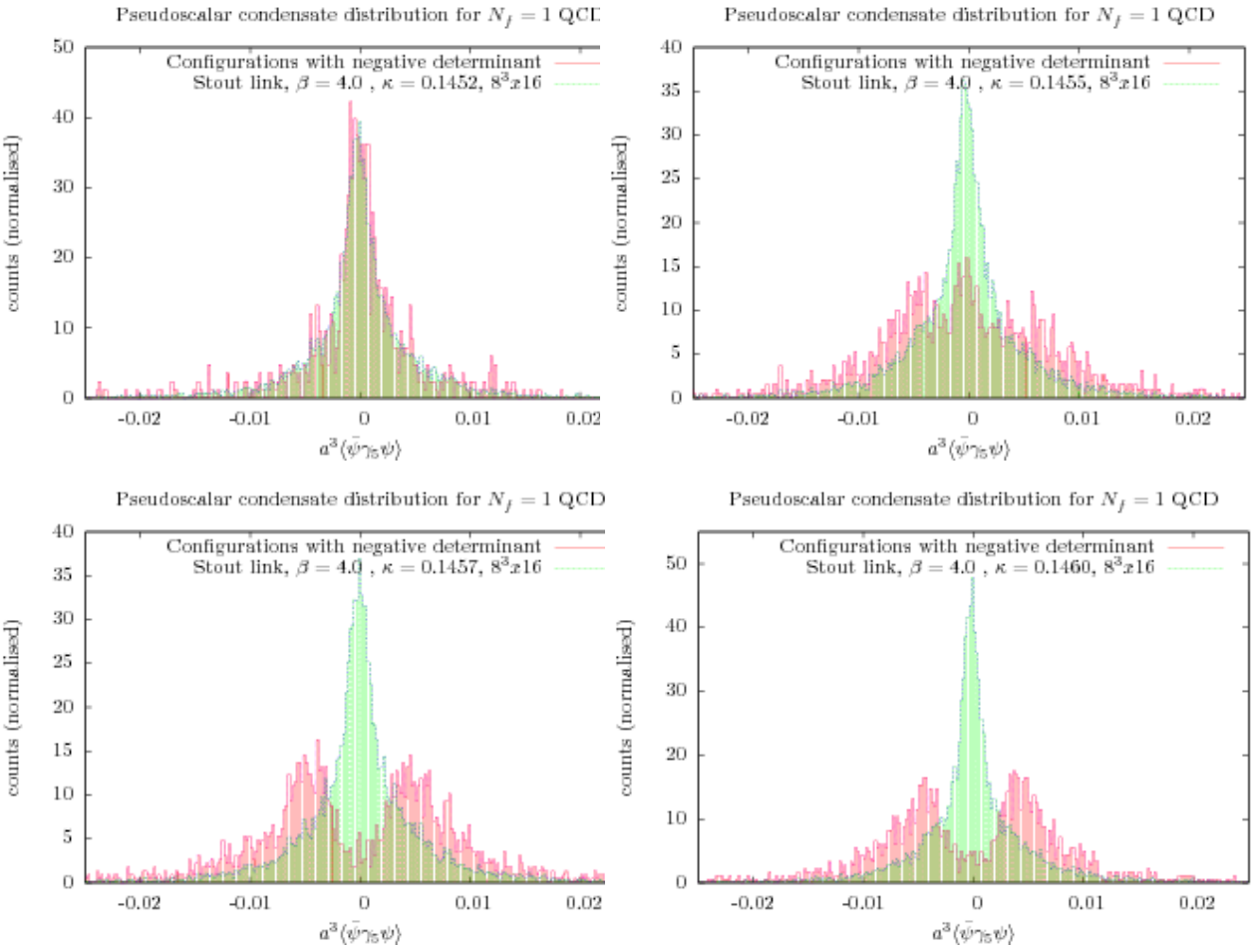

Figure 8.3: CP breaking for one flavour QCD? The configurations were separated into two distinct sets, depending on the determinant sign. The configurations with negative determinant exhibit a CP-symmetry breaking pattern? This interpretation is shown to be naive as the difference in the pseudoscalar distributions reflects the the lowest, real eigenvalue positions (Fig.(8.7)).

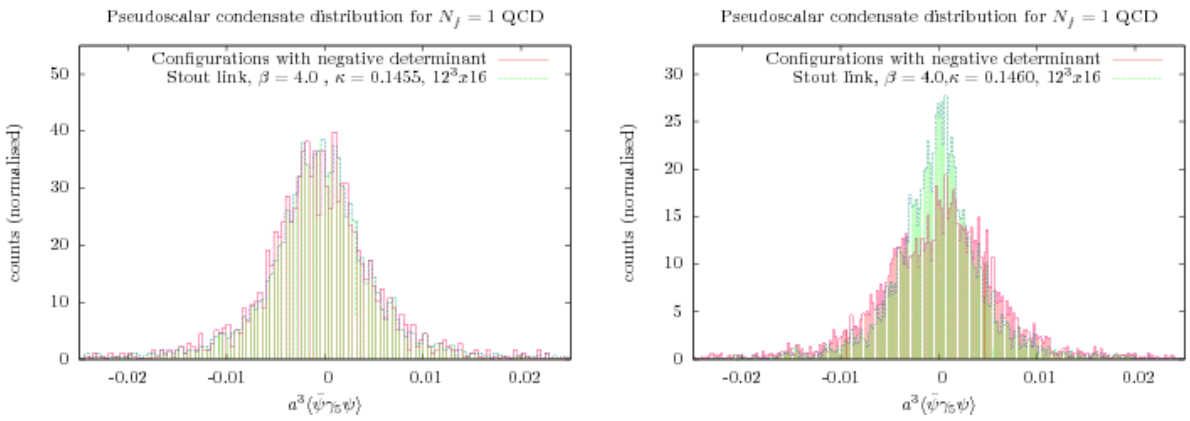

Figure 8.4: The two peaks vanishes as the lattice size increase. The configurations were separated into two distinct sets, depending on the determinant sign. The CP-symmetry breaking pattern previously observed on lattices 8^3x16 vanishes.

- The configurations with real eigenvalues λ_{real} the closest to zero ($|\lambda_{real}| < 0.001$, λ_{real} is negative or positive) add up to form two distant peaks in the pseudoscalar distribution.
- The configurations found with the most negative real eigenvalues $\lambda_{real} < -0.01$ form two close peaks in the pseudoscalar distribution.
- Configurations, where two low, real eigenvalues were found form a more complicated pattern. Four peaks appear for $\kappa = 0.1457$, which can be explained by the fact that the real eigenmodes enter "destructively" or constructively in the spectral decomposition, depending on their chirality sign. For $\kappa = 0.1460$, the asymmetric pseudoscalar distribution can be related to the asymetry in the distribution of $\chi_{num.}$.

This confirms that the lowest eigenvalues play a primary role in the pseudoscalar distribution.

For both 8^3x16 and 12^3x16 lattices, the real eigenvalue distributions were represented in Fig.(7.3) and Fig.(7.4). For the lattice size 12^3x16, more low, real and complex eigenvalues fluctuate close to zero.

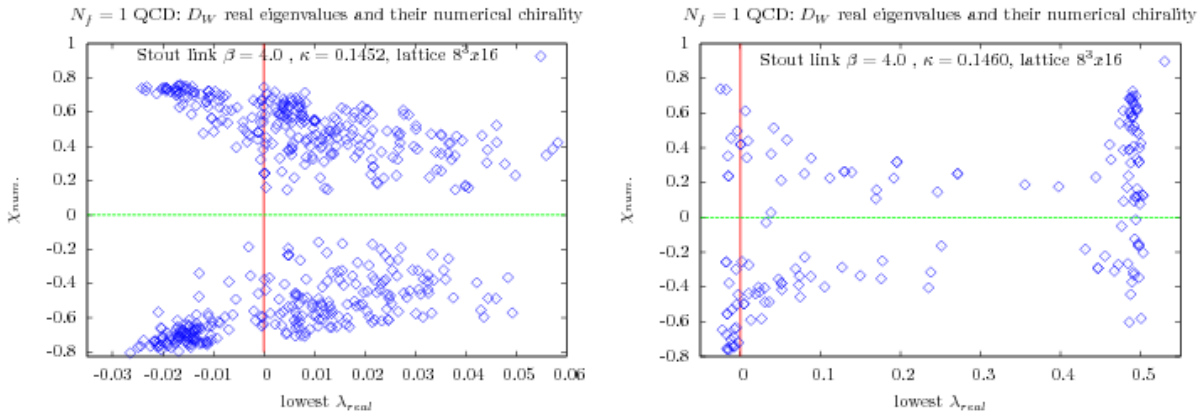

Figure 8.5: $\chi_{num.}$ is illustrated for the real eigenvalues only and put in relation with the eigenvalue position. Notice the intriguing asymmetry between left and right handed eigenvectors. For the right figure, the real eigenvalues were computed deeper and the chiralities appear to increase again around 0.5. This fact and the position where this happens confirm that the rightmost eigenvalues computed are doubler eigenmodes.

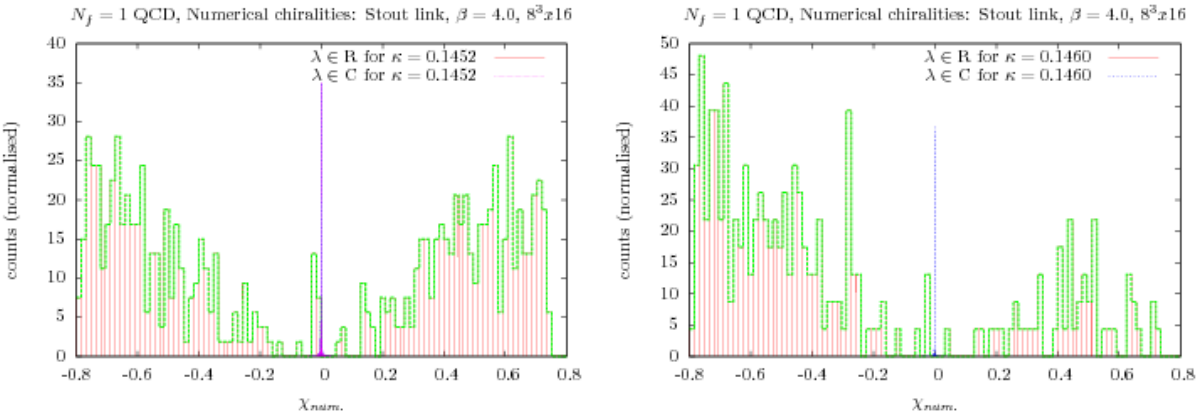

Figure 8.6: Distribution of $\chi_{num.}$ Notice the asymmetry for $\kappa = 0.1460$. This would indicate that the simulation remained stuck in a topological sector? As expected, the complex eigenmode chiralities peak precisely at zero.

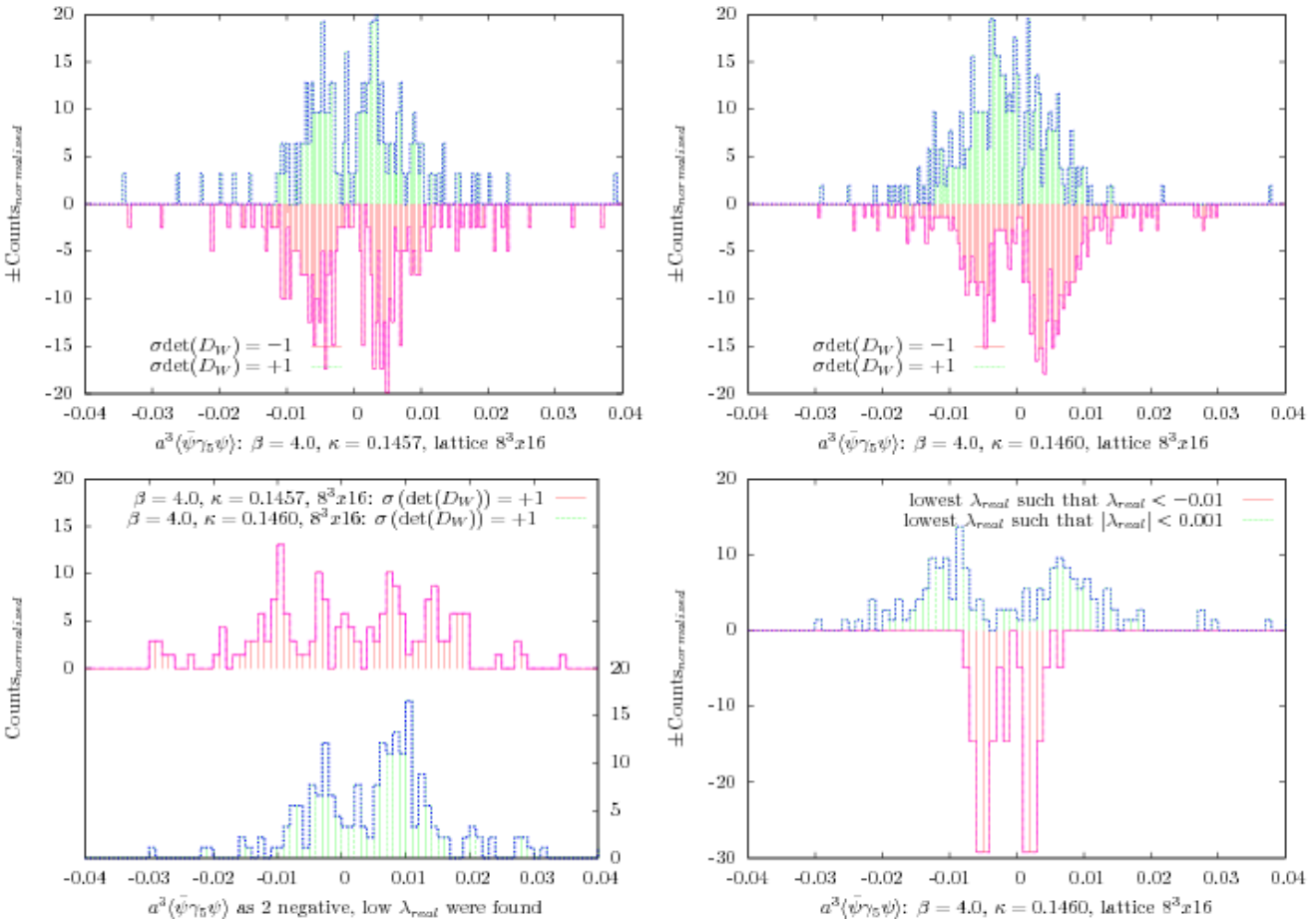

Figure 8.7: Discussion of the pseudoscalar condensate in function of the determinant sign and the lowest real eigenvalues distance to zero. The two peaks behaviour found for the lattice size $8^3 \times 16$ can be reproduced while the determinant sign is confirmed not to be a criterion. For more clarity, the y-axis is flipped according to the determinant signs of the configurations considered.

8.4.3 Spectral decompositions

Fig.(8.8) compares two spectral decompositions. One decomposition was computed with the operator Q and stochastic sources. The other one using eigenvalues computed on D_W with the peeling method. The extraction pattern is the one shown in Fig.(6.30).

In Fig.(8.8), contributions to $\mathrm{Tr}(\gamma_5 D_W^{-1})$ from the real and imaginary contributions are balanced and both spectral decompositions (with Q and D_W) coincide approximately.

Fig.(8.9) and Fig.(8.10) discuss the contribution of the real and complex eigenmodes separately and independantly of their position on the real axis.

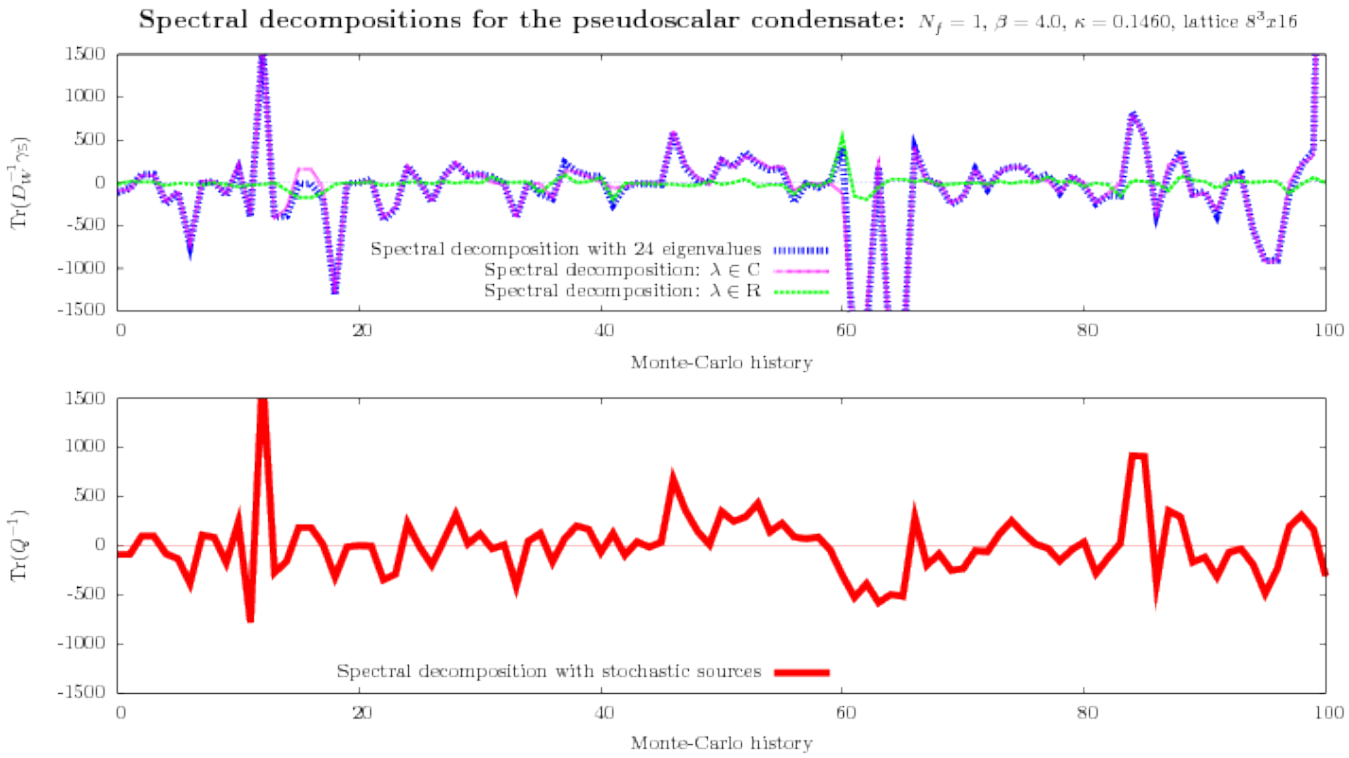

Figure 8.8: For 100 random configurations, spectral decompositions with the hermitian or non-hermitian Wilson-Dirac operators Q and D_W are compared. For the spectral decomposition with D_W, the contributions from the real and complex eigenmodes is explicitly shown. The spectral decomposition achieved with this kind of eigenvalue extraction reconstitute the pseudoscalar, in a first order. Obviously, the extraction pattern (Fig.(6.30)) peeled most of the complex eigenmodes with low complex part away and their effect is hidden but supposedly responsible for most of the deviations. The fact that they contribute less than the eigenvalues the closest from zero is compensated by their important number.

8.4.4 Consequences for the lattice study of CP-breaking?

Fig.(8.5) and Fig.(8.9) show that deeper eigenmodes start to deviate stronger from the physics in continuum, which is particularly true for eigenvalues between the physical and doubler eigenmodes.

Under the assumption that lowering the quark mass would have for main effect to simply pull the eigenspectrum further onto the left, the spectral decomposition point of view suggests that the artefacts observed in the Wilson-Dirac formalism could put in danger the study of CP breaking. For more inner eigenvectors, the departure from the continuum physics (D_W is less normal, its eigenvalues are less orthogonal and $\chi_{num.}$ further from ± 1) is consistent with the idea of Wilson. This issue should be taken care of in further computations in the Wilson formalism.

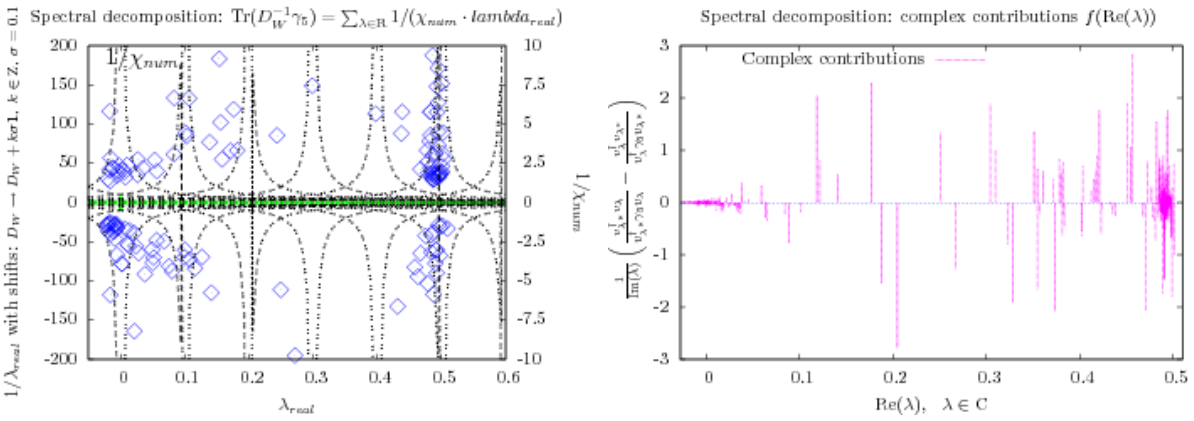

Figure 8.9: On the left, the real eigenvalue contributions to the spectral are evaluated. The black 3 lines suggest the reweighting $1/\lambda_{real}$ for 3 alternative shifts. On the right, the absolute contributions from the complex eigenmodes are evaluated, as if they were lying at $\mathrm{Re}(\lambda) = 0$, with $\lambda \in \mathrm{C}$. The non-normality of the Wilson-Dirac operator has for effect to increase the contributions from the deep eigenspectrum ($\mathrm{Re}(\lambda) > 0.08$). If pulling the eigenspectrum further into the negative part of the complex plane, one expect larger contributions from the complex eigenmodes. The computation is only precise up to $\mathrm{Re}(\lambda) \approx 0.4$ and the doublers area should behave as the physical one.

According to the simple model discussed in Fig.(8.7), the differences observed between the 8^3x16 and the 12^3x16 lattices (Fig.(8.3) and Fig.(8.4)) lie in the different low eigenvalues density. For larger lattices, the increasing density of real and complex eigenvalues settling close to zero cancels the simple effects demonstrated in Fig.(8.7).

8.4.5 Insights from eigenvalues and their numerical chirality distribution?

This study illustrates which insights may become available from computations of the inner eigenmodes and their numerical chirality.

For several configurations, Fig.(8.11) discusses how two low, real eigenvalues computed close to zero behave in respect to $\chi_{num.}$.

configurations where two lowest eigenvalues were computed are selected. Such distributions show a qualitative change between $\kappa = 0.1452$ and $\kappa = 0.1460$. Observe also that, as the eigenspectrum is shifted toward the negative sector, combinations preserving the pseudoscalar condensate seem to be privilegied. With the quantities $\{\lambda_{real},\ \chi_{num.}\}$, these combinations are ($\sigma() = \pm$ is the sign function):

- $\{\sigma(\lambda_{real\,1}) = \sigma(\lambda_{real\,2}),\ \sigma(\chi_{num.\,1}) = -\sigma(\xi_{num.\,2})\}$
- $\{\sigma(\lambda_{real\,1}) = -\sigma(\lambda_{real\,2}),\ \sigma(\chi_{num.\,1}) = \sigma(\xi_{num.\,2})\}$

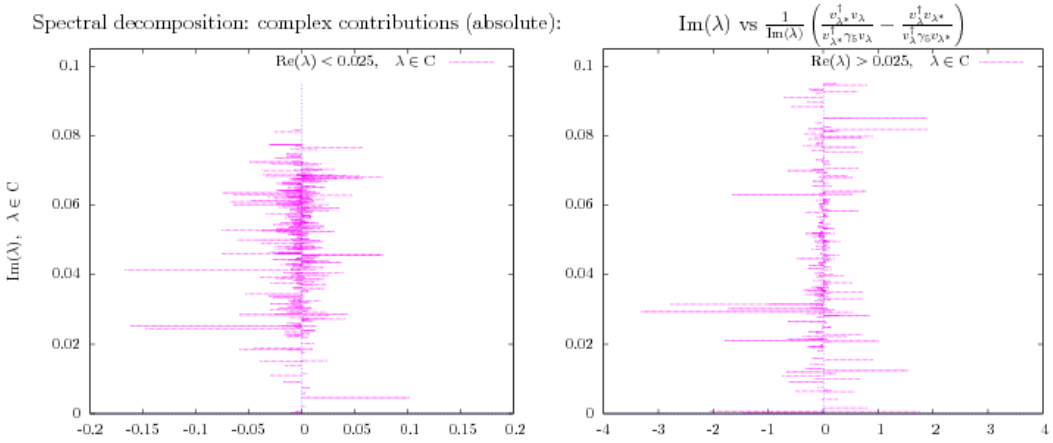

Figure 8.10: This figure discusses the contribution from the complex eigenmodes of D_W as function of the imaginary position (the x-axis legend is indicated above the right window). On the left, this is studied for the lowest eigenvalues, which are distributed around zero. On the right, the deeper regions are examined. The distribution fluctuations are relatively uniform and the reweighting $1/\lambda$ is mostly responsible for the partial vanishing of the complex contributions.

In addition to this, as both eigenvalues are separated by zero, a negative numerical chirality is privileged(?!).

For deeper eigenvalues extraction, up to the doublers eigenmodes and on 8^3x16 lattices, a similar discussion is presented on the right of Fig.(8.12). On the left, for 12^3x16 lattice, the lowest eigenmodes are discussed for a small set of configurations.

In Fig.(8.13), four configurations eigenspectra are tracked along the Monte-Carlo history.

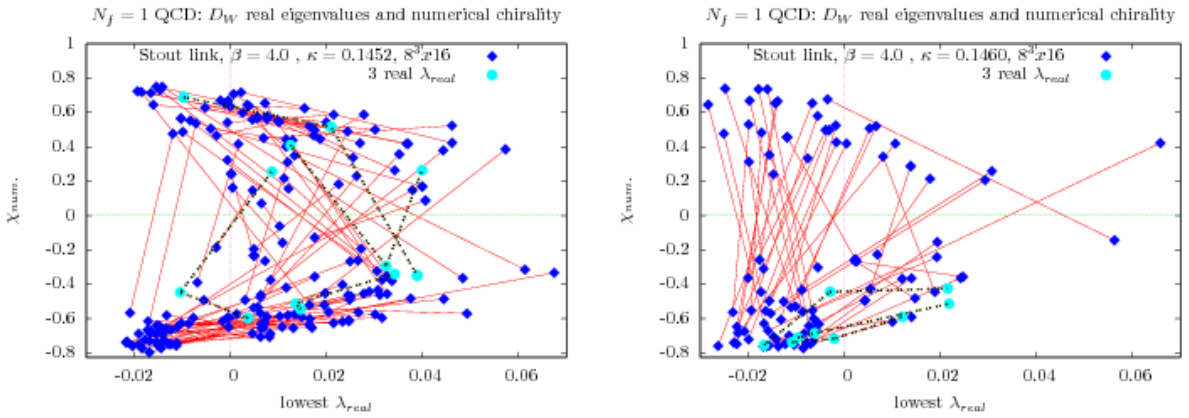

Figure 8.11: Distribution of $\chi_{num.}$ for $\kappa = 0.1452$ and $\kappa = 0.1460$. The configurations presented had two or three real eigenvalues computed. Eigenvalues found in the similar configuration are connected with a line. The plots illustrate the real eigenvalues distribution and behaviour as the bare quark mass is lowered (lattice $8^3 \times 16$).

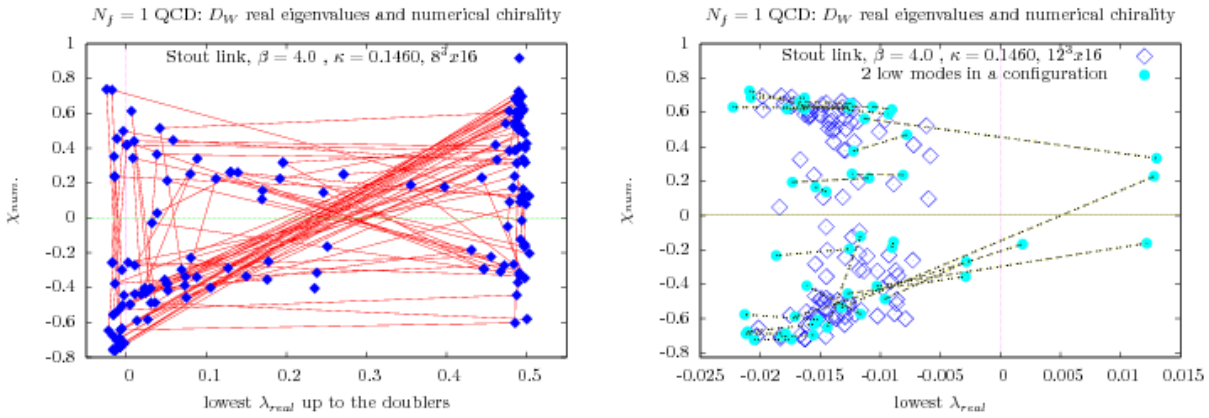

Figure 8.12: Spectral decomposition and distribution of $\chi_{num.}$ for a deeper eigenvalue computation. The lines connect the real eigenmodes found in a given configuration. The first doubler sector is expected to show inversed chiralities, in comparison with the lowest, real eigenmodes. The diagonal symmetry illustrates this fact. A similar examination was made on a larger 12^3 lattice.

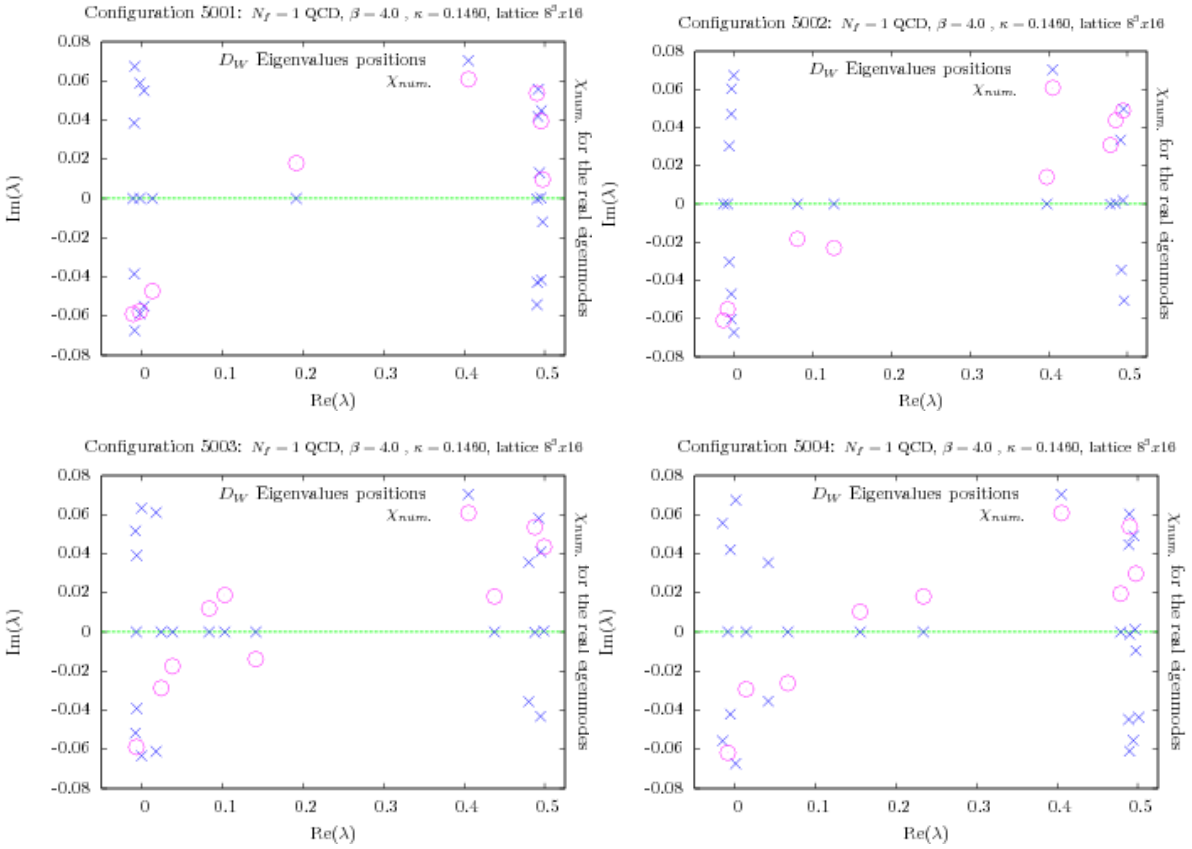

Figure 8.13: Deep extractions of the Wilson-Dirac eigenmodes allow for a reconstitution of the eigenspectra, with the real eigenvalue numerical chiralities. The low complex and real eigenvalues are the most relevant for the spectral decomposition, while the inner real eigenvalues contains complementary informations about the configuration topology. In a certain sense, such a figure tracks the backbones of 4 figurations as they evolve along the Monte-Carlo history.

Chapter 9

Sym project

9.1 Corrections on the spectrum of $\mathcal{N} = 1$ $SU(2)$ Sym

As for one flavour QCD, the supermultiplets mass spectrum of $\mathcal{N} = 1$ $SU(2)$ Sym is affected up to 7 percent. The cases where deviations from the determinant sign have some relevance are indicated in publications of the DESY-Münster collaboration. For example, see [58].

In practice and as discussed in Appendix C, a few (4) doublers showed up in eigenvalues computations.

9.2 Scalar condensate and vacuum structure.

The determinant sign have an important impact on the scalar condensate distribution, as can be seen on Fig.(9.2).

For the parameter setup $\beta = 1.6$, $\kappa = 0.1580$, lattice 16^4, the determinant sign repartition is summarised in the table below. It indicates that the lowest real eigenvalues are fluctuating close to zero.

$\sigma(\det(D_W)) = +1$	$\sigma(\det(D_W)) = -1$
2823 configurations	2757 configurations
661 with two $\lambda_{real} < 0$	54 with three $\lambda_{real} < 0$
3 with four $\lambda_{real} < 0$	0 with five $\lambda_{real} < 0$

Table 9.1: sign distribution summary for $\mathcal{N} = 1$ $SU(2)$ Sym.

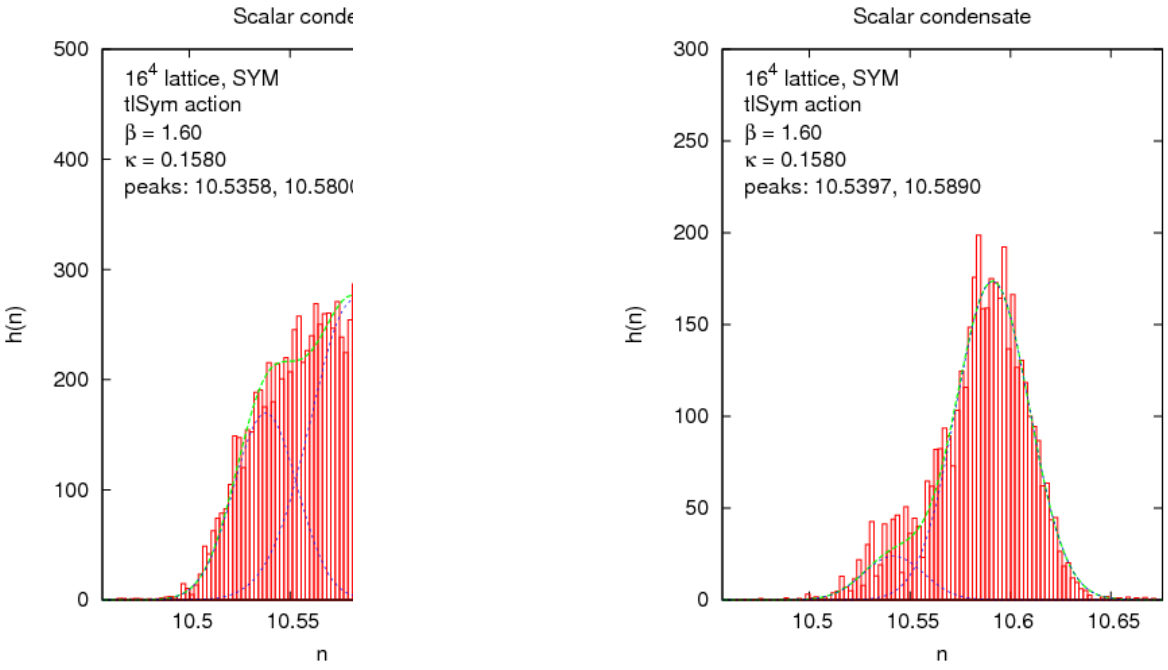

Figure 9.1: As they are published in [58], the scalar condensate with a reweighting from the determinant sign or without it are plotted resp. on the right and on the left. Two-gaussian fit seem reasonable. The right picture suggests a spontaneous symmetry breaking scenario, a signal remnant of a supersymmetric phase may have been detected on the lattice.

Chapter 10

Summary and discussion

After an overview of the theoretical questions under investigation with the one flavour projects, the non-hermitian Wilson-Dirac operator D_W low eigenmodes are discussed in different contexts on the lattice (determinant or Pfaffian sign, topological charge, doublers, zero modes, spectral decompositions). In practice, the eigenvalues of the non-hermitian Wilson-Dirac operator D_W are computed with the Arnoldi algorithm. However, the operator non-normality, its eigenspectrum shape as well as its size appear to be important limitations.

In a first step, a basic understanding of the algorithm behaviour and limitations is gained from its mathematical description. The discussion is completed with practical tests. From this knowledge, this work presents an improvement program, where the algorithm extraction performances are improved with *preconditioning* through polynomial transformations $D_W \to P(D_W)$ of the eigenspectrum of D_W. Three main accelerating techniques were discussed:

- The power polynomial transformation
- The Faber polynomial transformation
- Iterations of the above methods (peeling method, mixed polynomials, ...)

The design of such polynomials is at least partially arbitrary. In addition to the many parameters involved in the design of polynomial transformations, the efficiency also depends on the distribution of the Wilson-Dirac operator eigenvalues, the matrix size, the memory available, ... Therefore, visual and numerical test methods were proposed. They allow for the construction of efficient polynomial strategies, which were tested and compared on real configurations.

With these methods, the Arnoldi algorithm computational performances are extensively improved while the range where real eigenvalues can be extracted is broadened. As a result:

For models in the Wilson formalism, the determinant sign could be effectively computed within a broader range of parameters and lattice sizes. The method efficiency is optimal for the smallest real eigenvalues and is expected to improve along with the computational performances, in particular making use of larger extraction polynomials. Nevertheless, the determinant sign remains an

important bottleneck and its computation is still difficult. Tests showed that an extraction of the more inner eigenspectrum (the real eigenvalues lying inside the eigenspectrum) requires a increasingly steep effort.

While the determinant signs were computed, comparisons between the low eigenspectra of the non-hermitian and hermitian Wilson-Dirac operators became available for the one flavour theories. Distributions of the eigenvalues of both eigenspectra were found to fluctuate partially around their exact distribution in the continuum, despite the fact that the two lowest eigenvalues of the non-hermitian and hermitian Wilson-Dirac operators plotted in those studies are probably not always related one to one.

For one flavour QCD, the spectral decomposition offers an alternative point of view where the eigenspectrum of the non-hermitian Wilson-Dirac operator D_W can be connected to the pseudoscalar condensate value. As a result, a quantitative picture arises, where the pseudoscalar condensate gets its value predominantly from the low, real eigenvalues. This model could be positively tested with the current results for the pseudoscalar condensates and its distributions. Contributions from the different eigensectors (the complex and the real eigenvalues) were evaluated and the picture that emerged could be compared to its counterpart in the continuum.

As the quark mass is lowered, the low eigenspectrum is expected to move further into the left half of the complex plane. In this situation and contrasting with the situation in the continuum, preliminary tests show that important artefacts from the Wilson formulation and its non-normality may show up.

An approximative evaluation of the quark mass is accessible in the lattice realisation of QCD, in the Wilson formalism. This is the case either through the real eigenvectors chirality or through comparisons of the lowest eigenvalues of the hermitian and non-hermitian Wilson-Dirac operators. On the lattice and for one flavour QCD, this naively removes the ambiguity around the definition of the quark mass.

Appendix A

Arnoldi-Faber method for large non hermitian eigenvalue problems

This appendix introduces a method based on the Schwarz-Christoffel conformal transformation for computing the rightmost eigenvalues of large non-hermitian matrices, as descibed in [33].

A.1 Minmax problem for the Arnoldi algorithm

The Arnoldi factorisation reads

$$AV_m = V_m H_m + f_{m+1,\,m} v_{m+1} e_m^*,$$

with initial vector v_0, $\|v_0\|_2 = 1$. Its iterations generate iteratively an orthonormal basis $V_m = [v_0, \ldots v_{m-1}]$ of the Krylov space $\mathcal{K}_m(A, v_0)$ and constructs the Hessenberg matrix $H_m = V_m^* A V_m$, as explained in section 5.3.

Let us assume that the rightmost eigenvalue λ is unique and semi-simple (algebraic and geometric multiplicities are equal) and let P denote the corresponding spectral projector ($P \equiv v_\lambda v_\lambda^T$). If $Pv_0 \neq 0$, then $u = Pv_0/\|Pv_0\|_2$ is an eigenvector of A with eigenvalue λ. Let define $y = (\mathbf{1}-P)v_1/\|(\mathbf{1}-P)v_0\|_2$, if $(\mathbf{1}-P)v_0 \neq 0$ and $y = 0$ otherwise. Call $\mathcal{P}_{m-1}$ the set of polynomials of degree $\leq m-1$. The following proposition holds

proposition:

The angle $\theta(u, \mathcal{K}_m)$ between u and $\mathcal{K}_m$ satisfyies

$$\sin\,\theta(u, \mathcal{K}_m) \leq \min_{\{p \in \mathcal{P}_{m-1},\, p(\lambda)=1\}} \|p(A)y\|_2 \tan\theta(u,\, v_0)$$

where $\theta(u, v_0)$ is the angle between u and the starting vector v_0. $p(\lambda) = 1$ is a standard normalisation (The angle θ is a geometric analogy for evaluating the distance between subspaces [22]).

proof: see [33].

The angle θ is a geometric analogy for evaluating the distance between subspaces

(see for example [22]). As the Eigenvector u can be fully constructed from the Krylov space $\mathcal{K}_m$ if $\sin\theta(u_1, \mathcal{K}_m) \to 0$, the proposition states that an ideal choice of polynomial $p \in \mathcal{P}_{m-1},\ p(\lambda) = 1$ minimises $\|p(A)y\|_2$. For A diagonalisable, this is realised if p satisfies the following minmax problem

$$\gamma_{m-1}(\Omega) = \min_{\{p \in \mathcal{P}_{m-1},\, p(\lambda)=1\}} \max_{z \in \Omega} |p(z)|, \tag{A.1}$$

where $\Omega \subset \mathbb{C}$ is a compact set containing the whole eigenspectrum of A, with the exception of λ.

Define now $\Omega^c \backslash \Omega$ the complement of Ω with respect to $\bar{\mathbb{C}} = \mathbb{C} \cup \{\infty\}$ and make the hypothesis that Ω^c is simply connected. The Riemann mapping theorem (see for example [34]) ensures the existence of a function $\omega = \Phi(z)$ mapping Ω^c conformally (the geometric angles are locally conserved by the transformation) onto $D^c \backslash D$, the exterior of the unit disc $D = \{\omega \in \mathrm{C}, \|\omega\| < 1\}$, satisfying the conditions

$$\Phi(\infty) = \infty, \quad 0 < \lim_{z \to \infty} \frac{\Phi(z)}{z} < \infty.$$

As a consequence, the Laurent expansion of $\Phi(z)$ is of the form

$$\Phi(z) = \alpha z + \alpha_0 + \frac{\alpha_1}{z} + \frac{\alpha_2}{z^2} + ... \, \alpha > 0.$$

Let $F_k(z) = \alpha_k^k z^k + \alpha_{k-1}^k z^{k-1} + ... + \alpha_0^k$ be the polynomial part of the Laurent expansion of $(\Phi(z))^k = \alpha_k^k z^k + \alpha_{k-1}^k z^{k-1} + ... + \alpha_0^k + \frac{\alpha_1^{(k)}}{z} + ...$ The *Faber polynomial* is $F_{k,\,\Omega}(z)$, of degree k and generated on Ω.

Now let $\Psi(\omega)$ be the inverse of $\Phi(z)$ given above and suppose Ω contained in the disc $\|z\| < R$. Then there is a known result stating

$$\frac{\Psi(\omega)}{\Psi(\omega) - z} = \sum_{k=0}^{\infty} \frac{F_k(z)}{\omega^{k+1}},$$

where the convergence is uniform for all $\|\omega\| \geq R$. $\Psi(\omega)$ has at infinity a Laurent expansion of the form $\Psi(\omega) = \beta\omega + \beta_0 + \frac{\beta_1}{z} + \frac{\beta_2}{z^2} + ...$, $\beta = \frac{1}{\alpha}$. With this last expansion and with the relation above, the Faber polynomials can be recursively computed from

$$\begin{aligned} F_0(z) &= 1 \\ F_1(z) &= (z - \beta_0)/\beta \\ F_k(z) &= (zF_{k-1}(z) - (\beta_0 F_{k-1}(z) + \ ... \\ +\beta_{k-1}F_0(z)) &- (k-1)\beta_{k-1})/\beta, \quad k \leq 2. \end{aligned}$$

Faber polynomial can also be applied to the cases where Ω is a circle or an ellipse. A transformation mapping the outside of Ω onto the outside of the unit circle was found ($\Omega^c \backslash \Omega \to D^c \backslash D$).

A.2 Computation of Faber polynomials for polygons: the Schwarz-Christoffel transformation

A.2.1 The Schwarz-Christoffel transformation

Assume that Ω is a polygon with p vertices z_1, z_2, z_3, ..., z_p given in counter clockwise order with respective interior angles $\alpha_1\pi$, $\alpha_2\pi$, ... , with $0 < \alpha_i < 2$ and $\sum_{j=1}^{p} \alpha_j = p - 2$.
Theorem:
Let $a_1 = e^{i\theta_1}$, ..., $a_p = e^{i\theta_p}$ with $0 \leq \theta_1 \leq ... \leq \theta_p \leq 2\pi$ be pre-images of vertices of Ω under the conformal map Ψ, mapping D^c onto Ω^c. Then

$$\Psi(w) = C_\psi \int_{w_0}^{w_1} \Pi_{j=1}^{p} (1 - \frac{a_j}{t})^{\alpha_j - 1} dt + \Psi(w_0) \tag{A.2}$$

with $w \in D^c$, $w_0 \in D^c$ and $C_\Psi \in \mathbb{C}$

proof:
The above identity can be constructed applying some simple transformations on the standard conformal map [33] [34] $\Psi_1 : D \to \Omega^c$ given by

$$\Psi_1(w) = C_{\psi_1} \int_{\tilde{w}}^{w} \Pi_{j=1}^{p} (t - a_j)^{\alpha_j - 1} \frac{dt}{t^2} dt + \Psi(\tilde{w}),\ w,\ \tilde{w} \in D^c. \tag{A.3}$$

A.2.2 Schwarz-Christoffel transformation parameter determination

The values C_ψ, a_1, ..., a_p are known as the *accessory parameters* and have to be precisely computed. The problem is to find $a_1 = e^{i\theta_1}$, ..., $a_p = e^{i\theta_p}$ such that $\Psi(\bar{a}_k) = \Psi_1(a_k) = z_k$, $k = 1$, ..., p since $\Psi_1(0) \to \infty$, the choice of $a_p = 1$ determines Ψ_1 uniquely.

The *crowding phenomenon* refers to the numerical problems arising as some pre-vertices are too close one another.

Construction of the Faber polynomials The Faber polynomial can be numerically evaluated using the *Driscoll toolbox* [31].

Appendix B

Non-normality of the non-hermitian Wilson-Dirac operator and consequences

B.1 Non-normal matrices and right, left eigenvectors

For a given operator A in $\mathrm{C}^{n\times n}$, *right and left eigenvectors* $|R_\lambda\rangle$ and $\langle L_\lambda|$ are defined respectively as $A\,|R_\lambda\rangle = \lambda\,|R_\lambda\rangle$ and $\langle L_\lambda|\,A = \lambda\,\langle L_\lambda|$. A right vector of A is the left vector of the A^T and vice versa.
The two following general cases can be distinguished:

- *normal* matrices $AA^\dagger = A^\dagger A$:
  They are diagonalisable by unitary matrices. In that case, orthonormal sets of right and left eigenvectors $\{|R_\lambda\rangle\}$ and $\{\langle L_\lambda|\}$ can be found (and $\{\{|R_\lambda\rangle\}$ span the entire space C^n). It holds also $\langle L_\lambda|R_{\tilde\lambda}\rangle = \delta_{\lambda,\,\tilde\lambda}$.

- *non-normal* matrices $AA^\dagger \neq A^\dagger A$:
  Non-normal matrices can only be decomposed into upper-triangular matrices under unitary transformations. The elements in the sets $\{|R_\lambda\rangle\}$, $\{\langle L_\lambda|\}$ cannot be set orthogonal one another. Besides this, A may be *defective* [1].

B.2 Non-hermitian Wilson-Dirac operator and non-normality

In its continuum version, because the partial derivative $i\partial/\partial_x$ as well as the fields elements $i\tau^a$, $\tau^a \in su(N_c)$ are antihermitian, the Wilson-Dirac operator is normal ($D^\dagger D = -DD = DD^\dagger$) and the distinction between right and left eigenmodes is lifted.

[1] A matrix is defective is some of its eigenvalues have different algebraic and geometric multiplicities. An example is $\begin{pmatrix} a & 1 \\ 0 & a \end{pmatrix}$, with eigenvalues $\{a,\,a\}$ but only one eigenvector.

In the Wilson formulation on the lattice, however, the non-hermitian Wilson-Dirac operator non-normality has important consequences.

B.2.1 D_W and biorthogonality

For D_W non-normal and non-defective, a diagonalisation can be accomplished by non-hermitian similarity transformation S

$$S^{-1} D_W S = \Lambda, \qquad S S^{-1} = \mathbf{1}, \tag{B.1}$$

with Λ diagonal. The right eigenvectors are in the columns of S and the left eigenvectors the rows of S^{-1}. From $SS^{-1} = \mathbf{1}$, it follows successively that left and right eigenvectors are *biorthogonal*

$$\left\langle L_\lambda \middle| R_{\tilde{\lambda}} \right\rangle = \delta_{\lambda,\,\tilde{\lambda}} \left\langle L_\lambda | R_\lambda \right\rangle \tag{B.2}$$

and that

$$\sum_\lambda \lambda \frac{|R_\lambda\rangle \langle L_\lambda|}{\langle L_\lambda | R_\lambda \rangle} = \mathbf{1}. \tag{B.3}$$

In addition to this, the γ_5-hermiticity forces the following pairings (see eq.(3.8))

$$\begin{aligned} \langle R_\lambda | \gamma_5 = \langle L_{\lambda^*} | , \quad \gamma_5 |R_\lambda\rangle = |L_{\lambda^*}\rangle , \\ \langle L_\lambda | \gamma_5 = \langle R_{\lambda^*} | , \quad \gamma_5 |L_\lambda\rangle = |R_{\lambda^*}\rangle . \end{aligned} \tag{B.4}$$

As a consequence, given the right eigenvectors, one can construct the left eigenvectors and inversely. The normalisation is fixed since

$$\langle L_\lambda | L_\lambda \rangle = \langle R_{\lambda^*} | \gamma_5 \gamma_5 |R_{\lambda^*}\rangle = \langle R_{\lambda^*} | R_{\lambda^*} \rangle . \tag{B.5}$$

B.2.2 Spectral decompositions of D_W

The following relations hold if D_W is non-singular:

$$D_W = D_W \mathbf{1} = \mathbf{1} D_W = \sum_\lambda \lambda \frac{|R_\lambda\rangle \langle L_\lambda|}{\langle L_\lambda | R_\lambda \rangle} \tag{B.6}$$

$$D_W^{-1} = D_W^{-1} \mathbf{1} = \mathbf{1} D_W^{-1} = \sum_\lambda \frac{1}{\lambda} \frac{|R_\lambda\rangle \langle L_\lambda|}{\langle L_\lambda | R_\lambda \rangle} \tag{B.7}$$

$$\tag{B.8}$$

Considering now $D_W^{-1}\gamma_5$, with eq.(B.4), it comes in term of the right eigenvectors

$$D_W^{-1}\gamma_5 = \sum_\lambda \frac{1}{\lambda} \frac{|R_\lambda\rangle \langle L_\lambda| \gamma_5}{\langle L_\lambda | R_\lambda \rangle} = \sum_\lambda \frac{1}{\lambda} \frac{|R_\lambda\rangle \langle R_{\lambda^*}|}{\langle R_{\lambda^*} | \gamma_5 |R_\lambda\rangle}. \tag{B.9}$$

B.3 Impact of non-normality on eigenvalues computing

As result of the right eigenvectors non-orthogonality, eigenvectors within or close to the Krylov subspace constructed by the Arnoldi iteration are not easily detected.

Chapters 5 and 6 show that the inner eigenvectors are not easily accessible. In addition to this and as discussed Appendix C, degenerated eigenvalues are not easily detected by the algorithm.

Appendix C

Eigenvalue doubling for $\mathcal{N} = 1$ Sym

From eq.(3.28) and eq.(3.29) a degeneracy of order 2 is expected for the (real and complex) eigenvalues.

C.1 Practical observations

For computation at finite precision with the non-hermitian D_W, the degeneracy is detected for eigenvectors having converged very precisely only. This occurs randomly on the configurations. This is an issue, since it may leave determinant sign computations ambiguous.

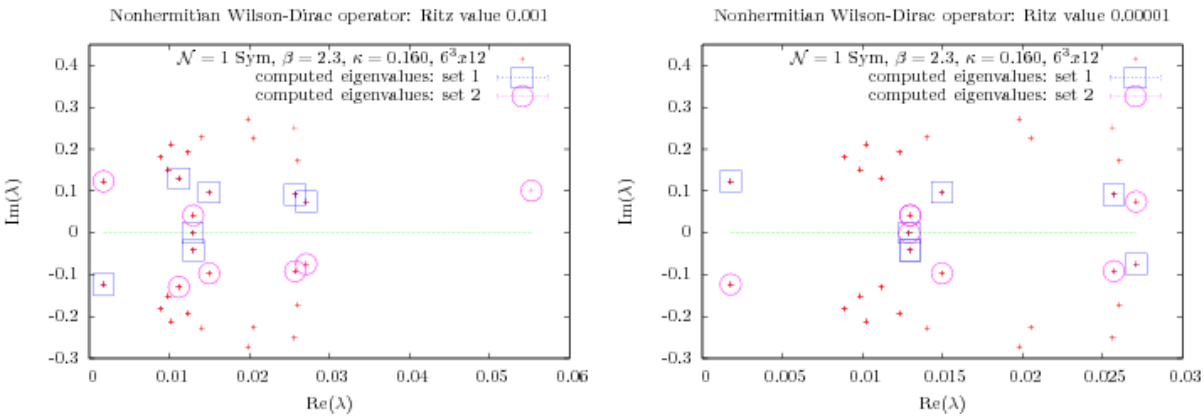

Figure C.1: The small dots in the background represents the eigenvectors of a converged computation. The squares and circles represents two sets of computed eigenvalues. Degenerated eigenvalues appear when a square and a circle are superposed. This situation occurs when the Ritz value, which controls the precision, is reduced.

Nevertheless, the degeneracy appears following a simple pattern. This is Shown in Fig.(C.1) and Fig.(C.2), where eigenvalues computations are decom-

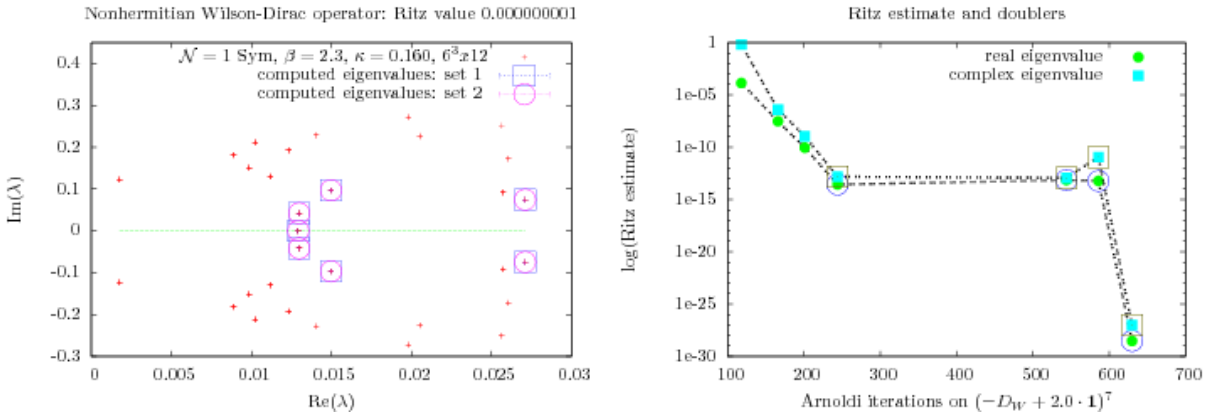

Figure C.2: On the left, as the Ritz value further decreases, degeneracy is completely retrieven. On the right, the doublers appear as the numerical precision given by the Ritz value (basically the distance $\|Av_{num.} - \lambda_{num.} v_{num.}\|_2$) is very good.

posed into two sets, in order to make the degeneracy manifest. The eigenvalues computed with an acceleration polynomial $D_W \rightarrow P_n(D_W)$ are plotted on a background where D_W's eigenspectrum is partially represented.

Along the Arnoldi algorithm convergence history illustrated in Fig.(C.2), the degeneracy simply appears as soon as a very high precision is reached. This naturally occurs first for the outer eigenvalues before degeneracy is detected for more inner ones. The degeneracy is apparently detected in some corrective steps.

C.1.1 Numerical chirality and the doublers, a sufficient criterion?

In practice, the observed doublers show very precisely measurable and identical $\chi_{num.}$. This observation suggests the idea to use $\chi_{num.}$ for distinguishing the doublers from the close eigenvalues. Therefore, although the behaviour of $\chi_{num.}$ partially depends on the position of λ_{real}, fluctuations in the values of $\chi_{num.}$ can be used as additional criterion for selecting out doublers from non-doublers eigenmodes. This should be controlled for the case of $D_{prec.}$.

C.1.2 Positive consequences from the doublers lifting

Since in practice one eigenspectrum half has to be computed, one wins a factor 4 for the determinant sign computations. From this point of view, a lifting of the doubling is rather advantageous.

Appendix D

Planar equivalence, $\mathcal{N} = 1$ Sym and one flavour QCD

This appendix introduces the notion of planar equivalence. A more advanced introduction may be found in [8].

D.1 large $1/N$ expansion, t'Hooft coupling and double line formalism

For multiflavour QCD with gauge group $SU(N_c)$. The quark and gluon propagators read:

$$\langle 0|T(\Psi^i \bar{\Psi}_j)|0\rangle = \delta^i_j S(x-y), \tag{D.1}$$

$$\langle 0|T((A_\mu)^i_j (A_\nu)^k_l)|0\rangle = \left(\delta^i_l \delta^k_j - \tfrac{1}{N}\delta^i_j \delta^k_l\right) D_{\mu\nu}(x-y), \tag{D.2}$$

The first equality follows because $\Psi\bar{\Psi}$ is a scalar. The second from the fact that the fields $A_\mu = A^a_\mu T^a \in SU(N_c)$ transform under the adjoint representation, which is meant by the two indices. One also used the well known $SU(N_c)$ property $\mathrm{Tr}\left((T^a)^i_j (T^b)^k_l\right) = \delta^{ab}\frac{1}{2}\delta^i_l \delta^k_j$. Notice also that the indices specify that Ψ and A_μ transform respectively under the fundamental and adjoint representations of $SU(N_c)$. The functions $S(x-y)$, $D_{\mu\nu}(x-y)$ represent propagators and recognizing that at large $\left(\delta^i_l \delta^k_j - \frac{1}{N_c}\delta^i_j \delta^k_l\right) \to \delta_l \delta^k_j$ $(N_c \to \infty)$ [1] 't Hooft introduced the *double-line formalism*, with the arrows following the indices (see Fig.(2.1)).

At large N_c, one may also introduce the *'t Hooft coupling* $g \to \frac{g}{N^{1/2}}$. Assuming such a modified theory, consider the vacuum Feynman graphs. The number of occurrences of those graphs is given by

$$N_c^{F-E+V} \equiv N^\chi, \tag{D.3}$$

whereas F is the number of faces, E the number of edges and V the number of vertices. It can be shown that:

[1] The vanishing trace property disappears, which implies $SU(N_c) \to U(N_c)$. Physically, one neglects the scalar singlet [13]

Figure D.1: On the left, the gluon propagator in the standard formalism, on the right, its correspondence in the double-line formalism.

(a) the leading connected graphs are of order N^2 and are just made up of gluons. (b) the leading connected graphs with quark lines are of order N. There is only one quark loop which also forms the boundary of the graph.

Topologically, the number in eq.(D.3) appears to correspond to the *Euler index*, defined as

$$\chi \equiv 2 - 2H + B,$$

where H is the number of handles, B the number of holes.

As a result, in the 't Hooft coupling and since their Euler index is the highest, the *planar graphs* become statistically dominant in the large-N_c limit. In turn, they describe the relevant perturbation theory [2].

D.1.1 Orientifoldisation and planar equivalence

Starting from the $\mathcal{N} = 1$ Sym *parent* theory with 't Hooft couplings, a *daughter* theory having similar planar graphs is constructed.

- *parent theory:* Consider the $\mathcal{N} = 1$ Sym theory with the Majorana fields λ^i_j and pair the gluino and anti-gluino fields as $\{\lambda_{ij},\, \lambda^{ij}\}$. λ^i_j is antisymmetric since in the adjoint representation. In those notations, the generator of the adjoint representation transforms at large N_c on the following manner [3]

$$T^a_{adj} \sim T^a \otimes 1 + 1 \otimes \bar{T}^a,$$
$$(T_{adj})_a = (\bar{T}_{adj})_a = T^a_{adj},\ \ \bar{T}^a = -(T_a)^*.$$

  Because the Majorana fields are in the adjoint representation, the gluino-antigluino propagators can be described in the double line formalism.

[2] For the case of gluonic vacuum bubbles, planar graphs have the topology of the sphere $\chi = 2$, while non-planar graphs have for example the topology of the torus $\chi < 2$.

[3] in tensor notations, the decomposition $N_c \otimes \bar{N}_c = (N_c^2 - 1) \oplus 1$ is realised as $q^j \bar{q}_i = \left(q^j \bar{q}_i - \frac{1}{N_c} q^k \bar{q}_k \delta^j_i\right) \oplus \frac{1}{N_c} q^k \bar{q}_k \delta^j_i$. Notice $(...) \sim q^j \bar{q}_i$ $(N_c \to \infty)$. This, motivates the decomposition $(N_c^2 - 1) \oplus 1 \sim \frac{N_c^2}{2} \oplus \frac{N_c^2}{2}$ with generators presented above. ($\frac{1}{2}$ comes from antisymmetry under adjoint representation).

- *daughter theory:* One the other hand, consider some fermionic fields $\{\Psi_{ij},\ \Psi^{ij}\}$ transforming under the fundamental representation, as suggested by the indices. The system of generators reads

$$T^a = T^a \otimes 1 + 1 \otimes T^a,$$
$$(T)_a = (\bar{T})_a = T^a.$$

  As in the parent theory, propagators can be built combining the daughter fermionic fields. After contraction of the indices, they can be described in the double line formalism. However, as the fields transform under the fundamental representation uniquely, the lines are running in the same direction, as in Fig.(D.2).

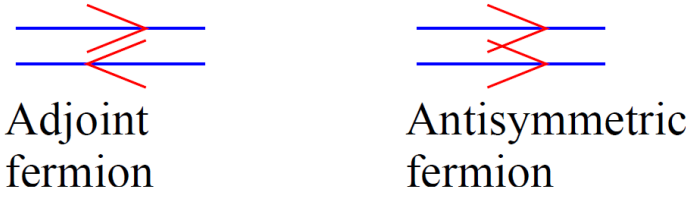

Figure D.2: On the left, the large $1/N_c$ expansion double lines formalism for the gluino-antigluino propagator. On the right, the double-line formalism for the orientifold A theory.

Orientifold A

Orientifold A(ntisymmetric) is a daughter theory constructed with Dirac spinors $\Psi_{[ij]}$ and $(N_c^2 - N_c)$ degrees of freedom ($\Psi_{[ij]} = -\Psi_{[ji]}$). As the parent theory with Majorana fields λ^{ij} has $(N_c^2 - N_c)/2$ fermionic degrees of freedom, the number of Majorana fields is artificially doubled, keeping then track of a factor $1/2$.

As argued above, both theories will have the same planar graphs, but one line has inversed arrows. Orientifold A field theory also have a common bosonic sector and a vacuum structure identical to $\mathcal{N} = 1$ SYM.

Moreover, it can be proved that both theories have equals partition functions at large N_c. This is achieved comparing the determinants (see [9]).

D.2 Planar equivalence and $N_f = 1$ QCD

For $N_c = 3$, the orientifold A daughter theory turns out to be QCD with one flavour. This comes from the standard antisymmetrisation procedure $q^i = \epsilon^{ijk}\Psi_{[jk]}$ ($N = 3$) through which the antisymmetric Dirac spinors become usual quark fields.

Obviously, in that case, the dominance of planar graphs is just very approximately realised ($N_c = 3$). In turn, one flavour QCD is just very approximately planar equivalent to $\mathcal{N} = 1$ Sym.

D.2.1 Additional comments

In general, larger $N_f = N$ (N_c) corresponds to non-supersymmetric $\mathcal{N} = N$ Sym parent theories, while QCD-like theories with $N_c \neq 3$ are not planar equivalent to SYM $\mathcal{N} = 1$ (because, in general, $q^i = \epsilon^{ii_2 \ldots i_{N_c}} \Psi[i_2 \ldots i_{N_c}]$, whereas $\epsilon^{i\, i_2 \ldots i_{N_c}}$ is the antisymmetrisation, invariant under $SU(N_c)$ tensor).

Bibliography

[1] R.F. Dashen, Phys. Rev. D **3** , 1879 (1971).

[2] C. Vafa and E. Witten, Nucl. Phys. B **234** (1984) 173.

[3] M. Creutz, Annals Phys. **322** (2007) 1518, [arXiv:hep-th/0609187].

[4] M. Creutz, AIP Conf. Proc. **756** (2005) 143, [arXiv:hep-lat/0410043].

[5] M. Creutz, Phys. Rev. Lett. **92** (2004) 201601, [arXiv:hep-lat/0312018].

[6] T. Banks, Y. Nir and N. Seiberg, [arXiv:hep-ph/9403203].

[7] M. Creutz, Phys. Rev. Lett. **92** (2004) 162003, [arXiv:hep-ph/0312225].

[8] A. Armoni, M. Shifman and G. Veneziano, *From Super-Yang-Mills theory to QCD: planar equivalence and its implications*, [arXiv:hep-th/0403071].

[9] A. Armoni, M. Shifman and G. Veneziano, *Refining the proof of planar equivalence*, Phys. Rev. D **71** (2005) 045015, [arXiv:hep-th/0412203].

[10] G. Veneziano and J. Wosiek, [arXiv:hep-th/0603045].

[11] A. Armoni and E. Imeroni, Phys. Lett. B **631** (2005) 192, [arXiv:hep-th/0508107].

[12] I. Montvay, G. Münster: *Quantum Fields on a Lattice*, Cambridge, Cambridge University Press, 1994

[13] S. Coleman:*Aspects of symmetry*, Cambridge, Cambridge University Press, 1985

[14] S. Scherer, Adv. Nucl. Phys. **27** (2003) 277, [arXiv:hep-ph/0210398].

[15] I. Montvay, Int. J. Mod. Phys. A **17** (2002) 2377, [arXiv:hep-lat/0112007].

[16] G. Veneziano and S. Yankielowicz, Phys. Lett. B **113** (1982) 231.

[17] A. Morel, J. Phys. (France) **48** (1987) 1111.

[18] C. W. Bernard and M. F. L. Golterman, Phys. Rev. D **49** (1994) 486, [arXiv:hep-lat/9306005].

[19] S. R. Sharpe and N. Shoresh, Phys. Rev. D **64** (2001) 114510, [arXiv:hep-lat/0108003].

[20] Y. Saad, *Numerical methods for large eigenvalue problems*, Manchester, Manchester University Press, 1992

[21] L. N. Trefethen, M. Embree, *Spectra and Pseudospectra: The behaviour of Nonormal Matrices and Operators*, Association of American Publishers, 2005

[22] G. H. Golub, C. F. Van Loan *Matrix computations*, London, The John Hopkins University press, 1991

[23] L. N.N. Trefethen, D. Bau, *Numerical Linear Algebra*, SIAM, 2000

[24] R. B. Lehoucq, *Analysis and Implementation of an implicitly restarted Arnoldi Iteration*, PHD Thesis, Rice University, Houston Texas, 1995

[25] T. Sudmann, *Gitter-QCD mit leichten Wilson-Quarks*, PHD Thesis, itp, Münster University, 2009

[26] R.B. Lehoucq, D.C. Sorensen, *Deflation Techniques for an Implicitly Restarted Arnoldi Iteration*, SIAM J. Matrix Anal. Appl, 1996

[27] D.C. Sorensen, *Implicitly Restarted Arnoldi/Lanczos Methods For Large Scale Eigenvalue Calculations*, Institute for Computer Applications in Science and Engineering (ICASE), 1995

[28] H. Neff, *Low Fermionic eigenmode dominance in QCD on the lattice*, [arXiv:hep-lat/0110076v1]

[29] I. Hip, T. Lippert, H. Neff, K. Schilling and W. Schroers, Nucl. Phys. Proc. Suppl. **106** (2002) 1004, [arXiv:hep-lat/0110155].

[30] I. Hip, T. Lippert, H. Neff, K. Schilling and W. Schroers, Phys. Rev. D **65** (2002) 014506, [arXiv:hep-lat/0105001].

[31] T. A. Driscoll. *A MATLAB Toolbox for Schwarz-Christoffel mapping.*, ACM Trans. Math. Soft. 22 (1996), pp. 168-186.

[32] ARPACK SOFTWARE, [http://www.caam.rice.edu/software/ARPACK/]

[33] V. Heuveline and M. Sadkane, *Arnoldi-Faber Method for Large Non Hermitian Eigenvalue Problems*[citeseer.ist.psu.edu/heuveline97arnoldifaber.html]

[34] A.I. Markushevich, *Theory of functions of a complex variable I, Theory of functions of a complex variable III*, Prentice-Hall, 1965

[35] D. H. Weingarten and J. L. Challifour, Annals Phys. **123** (1979) 61.

[36] H. Kleinert:*Pfadintegrale*, Mannheim, BI-Wissenschaftsverlag, 1993

[37] C. Gattringer, I. Hip: *Analyzing the spectrum of general, non-hermitian Dirac operators*, (1998), texttt"hep-lat/98090902v1"

[38] H. Neff: *Efficient computation of low-lying eigenmodes of non-Hermitian Wilson-Dirac matrices*, (2001), [arXiv:hep-lat/0110076v1]

[39] H. Neff, N. Eicker, T. Lippert, J. W. Negele and K. Schilling, Phys. Rev. D **64** (2001) 114509, [arXiv:hep-lat/0106016].

[40] I. Hip: *Eigenvalue Spectra of Lattice Dirac Operators*, Doctoral thesis, (1999)

[41] C. Gattringer, I. Hip: *On the spectrum of the Wilson-Dirac lattice operator in topologically non-trivial background configurations*, (1998), [arXiv:hep-lat/9712015v3]

[42] M. Daniel, M. Viallet: *The geometrical settings of the Yang-Mills type*, (january 1980), Reviews of Modern Physics, Vol.52, No.1

[43] M. Lüscher, Nucl. Phys. B **418** (1994) 637, [arXiv:hep-lat/9311007].

[44] V. A. Novikov, M. A. Shifman, A. I. Vainshtein, and V. I. Zakharov, Nucl. Phys. B 229 (1983) 381

[45] I. Montvay, Int. J. Mod. Phys. A **17** (2002) 2377, [arXiv:hep-lat/0112007].

[46] G. Curci and G. Veneziano, Nucl. Phys. B **292** (1987) 555.

[47] I. Montvay, [arXiv:hep-lat/0705.4356].

[48] E. E. Scholz and I. Montvay, PoS **LAT2006** (2006) 037, [arXiv:hep-lat/0609042].

[49] D. H. Weingarten and J. C. Sexton, Nucl. Phys. Proc. Suppl. **26** (1992) 613.

[50] K. Fujikawa, Phys. Rev. Lett. **42** (1979) 1195.

[51] M. Creutz, Rev. Mod. Phys. **73** (2001) 119, [arXiv:hep-lat/0007032].

[52] P. Hasenfratz , V. Laliena and F. Niedermeyer, Phys. Lett. **B427**, (1998) 125, [arXiv:hep-lat/9801021].

[53] P. Hasenfratz, [arXiv:hep-lat/0406033].

[54] H. Neff, N. Eicker, T. Lippert, J. W. Negele and K. Schilling, Phys. Rev. D **64** (2001) 114509, [arXiv:hep-lat/0106016].

[55] K. Schilling, H. Neff and T. Lippert, Lect. Notes Phys. **663** (2005) 147, [arXiv:hep-lat/0401005].

[56] F. Farchioni, C. Gebert, I. Montvay and L. Scorzato, Eur. Phys. J. C **26** (2002) 237, [arXiv:hep-lat/0206008].

[57] F. Farchioni, G. Münster and R. Peetz, Eur. Phys. J. C **38** (2004) 329, [arXiv:hep-lat/0404004].

[58] K. Demmouche, F. Farchioni, A. Ferling, I. Montvay, G. Münster, E. E. Scholz and J. Wuilloud, PoS **LAT2009** (2009) 268, [arXiv:0911.0595 [hep-lat]].

[59] K. Demmouche, F. Farchioni, A. Ferling, G. Münster, J. Wuilloud, I. Montvay and E. E. Scholz, PoS C **ONFINEMENT8** (2008) 136, [arXiv: hep-lat /0811.1964].

[60] F. Farchioni, G. Münster, T. Sudmann, J. Wuilloud, I. Montvay and E. E. Scholz, [arXiv: hep-lat /0810.0161].

[61] K. Demmouche, F. Farchioni, A. Ferling, G. Münster, J. Wuilloud, I. Montvay and E. E. Scholz, [arXiv: hep-lat/0810.0144].

[62] F. Farchioni, G. Münster, T. Sudmann, J. Wuilloud, I. Montvay and E. E. Scholz, [arXiv:hep-lat/0810.0161].

[63] F. Farchioni, G. Münster, T. Sudmann, J. Wuilloud, I. Montvay and E. E. Scholz, PoS **LAT2007** (2007) 135 [arXiv: hep-lat /0710.4454].

[64] F. Farchioni, I. Montvay, G. Münster, E. E. Scholz, T. Sudmann and J. Wuilloud, Eur. Phys. J. C **52** (2007) 305, [arXiv: hep-lat 0706.1131].

Aknowledgments

I wish to thank Federico Farchioni, for his continuous help, disponibility and his suggestions throughout this work. This was also a pleasure to collaborate with Istvan Montvay, in spite of the distance (between Hambourg and Münster). I would like to address also a special thank to Gernot Münster, for the opportunity to write a Thesis with him as well as his patient corrections of this work.

I am also grateful to my colleagues Tobias Sudmann, Kamel Demmouche, Alexander Ferling, Eva Baresel, Dirk Homeier and Tobias Bode for their help, their tips and their company.

Finally, I would like to thank warmly Judith for her support.

Selbstständigkeitserklärung:

Hiermit erkläre ich, die vorliegende Arbeit selbstständig und ohne fremde Hilfe verfasst und nur die angegebene Litteratur und Hilfsmittel verwendet zu haben.

Jaïr Wuilloud, 15.01.2010